

https://dspace.org/

Study of diamond/mullite composites by sol/gel and hot press sintering methods

Govo, Simbarashe Piniel

2011-04-15
http://hdl.handle.net/10539/9466

Downloaded from a DSpace repository. https://dspace.org/

Study of Diamond/ Mullite Composites by Sol/ Gel and Hot Press Sintering Methods

Simbarashe Piniel Govo

A dissertation submitted to the Faculty of Engineering and the Built Environment, University of the Witwatersrand, Johannesburg, in fulfilment of the requirements for the degree of Master of Science in Engineering.

– Johannesburg, 2010 –

DECLARATION

I, Simbarashe Piniel Govo declare that this dissertation is my own, unaided work. It is being submitted for the Degree of Master of Science in Engineering at the University of the Witwatersrand, Johannesburg. It has not been submitted before for any degree or examination in any other University.

Simbarashe Piniel Govo

This_____day of_____, 2010

Abstract

A study has been conducted into the synthesis of 10wt% diamond/ mullite composites through two methods: First through the hot press sintering of alumina and silica in stoichiometric composition for 3:2 mullites (mullite formed in situ) at 1400, 1450 and 1500^{o}C. Second through the sol/ gel process. The sol/ gel method only provided the basis for future development with no further discussion of the results while the hot press sintering method yielded composites with residual cristobalite and corundum phases. Achieved densities of the composites were 93.7, 94.6 and 95.8% of the theoretical density with respect to sintering temperatures of 1400, 1450 and 1500^{o}C for compact samples by the first method. Hardness – measured by Vickers indentation – of the composites decreased with increase in temperature with 15.5 ± 0.33GPa achieved at the lowest sintering temperature investigated. The decrease in hardness was attributed to the structural degradation of diamond to non-diamond carbon forms with increase in temperature as observed from Raman spectra of each of the composites. X-ray traces showed an increase in the mullite content with increase in temperature. The fracture toughness of compacts initially hot press sintered from alumina and silica in stoichiometric composition for 3:2 mullite with no diamond added decreased with increase in sintering temperature with 4.75 ± 0.10MPa·m$^{1/2}$ achieved at the lowest sintering temperature investigated. Further discussion to the structure and physical properties is presented.

Dedication

To my daughter *Kyla Tinevimbo Govo*

Acknowledgements

I would like to extend my gratitude to the ***DST/ NRF – Centre of Excellence in Strong Materials*** and ***PGMA (WITS University)*** for the financial support throughout my studies.

I also want to thank my supervisors *Prof. Iakovos Sigalas and Dr. Mathias Herrmann (Fraunhofer IKTS Dresden, Germany)* for the academic contribution, innovative ideas and unwavering patience towards the successes of the studies. I want to thank *Mr. Rudolf Erasmus (WITS, School of Physics)* for assistance in carrying out Raman spectroscopy.

To my wife *Farirai*, I say thank you for the emotional support along the course of my studies. When the road got steep you stood by my side to give fervent encouragement.

I also want to thank my family *Kyla, Sukai, Shelton and Sandra* for their patience throughout my studies and to my *Uncle Charles* for words of hope and encouragement to complete this work, I say God bless you.

Lastly I want to thank all my friends and colleagues in the School of Chemical and Metallurgical Engineering for the teamwork in carrying out all my experiments.

Above all, I thank God almighty for blessing me with the gift of life and the opportunity to further my studies, glory to His name.

Table of Contents

DECLARATION ..... **ii**

Abstract ..... **iii**

Dedication ..... **iv**

Acknowledgements ..... **v**

Chapter 1: Introduction **1**

1.0 Background and Motivation **1**

1.1 Project Overview **2**

Chapter 2: Literature Review **5**

2.1 Composite Materials - General **5**

2.2.1 Physical Properties of Composites *6*
2.1.1.1 Modulus of Elasticity 6
2.1.1.2 Density 7
2.1.1.3 Brittleness Factor 7

2.1.2 Toughening Mechanisms in Composites *8*

2.1.3 Fibre Reinforcement Toughening Mechanisms **10**

2.2 Mullite **13**

2.2.1 Mullite Formation *15*

2.2.2 Other Methods of Forming Mullite *16*

2.2.3 Mullite Preparation: Sol-gel process *18*

2.2.4 Advantages of the Sol/ Gel Method *20*

2.2.5 Types of Mullite *20*

2.2.6 Structural Data of 3:2 and 2:1 Mullites *21*

2.2.7 Lattice Constants for Mullite vs. Alumina content *22*

2.2.8 Mullite over Alumina *23*

2.3 Mullite Composites **25**

2.3.1 Zirconia-Mullite Composites *25*

2.3.2 Aluminium/ Alumina-Mullite Composites *27*

2.3.3 SiC-Mullite Composites *31*

2.3.4 Diamond-Mullite Composites *32*
2.3.4.1 Synthetic Diamonds 33
2.3.4.2 Polycrystalline Diamond, Manufacture and Industrial Purposes 33
2.3.4.3 Properties and degradation of Diamond 34
2.3.4.4 Structure of Diamond 35
2.3.4.5 Carbon Phase Diagram 36

Chapter 3: Experimental Techniques **40**

3.1 Chemicals **40**

3.2 Attrition Milling **40**

3.3 Sample Preparation, Heat Treatment and Composite Nomenclature **41**

3.3.1 The Sinter Mullites Method *42*

3.3.2 The Sol/ Gel Preparation Method *44*

3.4 Hot Press Sample Preparation **47**

3.5 Particle Size Analysis **48**

3.6 Density and Porosity **48**

3.7 X-Ray Diffraction **48**

3.8 Scanning Electron Microscopy / Energy Dispersive Spectroscopy **49**

3.9 Sample Cutting and Mounting **49**

3.10 Sample Surface Grinding and Polishing **49**

3.11 Etching **50**

3.12 Raman Spectroscopy **51**

3.12 Hardness and Fracture Toughness **51**

Chapter 4: Results **53**

4.1 Attrition Milling **54**

4.2 Overview of Results Obtained by Sinter Mullites Method **56**

4.3 Analysis of Samples by the Sol/ Gel Method **57**

4.3.1 X-Ray Diffraction – Sol/ Gel Method *57*

4.4 Analysis of Composites Produced by the Sinter Mullites Method **59**

4.4.1 X-Ray Diffraction – Sinter Mullites Method *59*

4.4.2 Scanning Electron Microscopy/ Energy Dispersive Spectroscopy *60*

4.4.2.1 Scanning Electron Microscopy/ Energy Dispersive Spectroscopy of as Received Powders 60

4.4.2.2 Scanning Electron Microscopy/ Energy Dispersive Spectroscopy of the Raw Powder Mixtures 62

4.4.2.3 Scanning Electron Microscopy/ Energy Dispersive Spectroscopy – 10 wt% Diamond Compact Samples 64

4.4.3 Raman Spectroscopy *68*

4.4.4 Hardness & Fracture Toughness – Samples by Sinter Mullites Method *71*

Chapter 5: Discussion **73**

5.1 X-Ray Diffraction 73

5.2 Scanning Electron Microscopy and Energy Dispersive Spectroscopy 73

5.3 Raman Spectroscopy (Diamond Containing Compacts) 75

5.4 Hardness and Fracture Toughness 77

Chapter 6: Conclusions & Recommendations 79

Appendix A: Reagent Mixing Calculations – Sol/ Gel Method 82

Appendix B: Density and Porosity Measurements 85

Appendix C: Hardness and Fracture Toughness Results 87

Appendix D: X-Ray Diffraction Patterns, Peak List and Reference Codes 90

List of Figures:

Figure 1: Schematic representation of toughening mechanisms in structural ceramics, after Ritchie [25], and as modified by [24]. 10

Figure 2: Crack path in SiC-TiB_2 composite ceramics. The incorporated TiB_2 grains show dark contrast, after Steinbrech [24]. 12

Figure 3: System Al_2O_3-SiO_2; (Cm = corundum, Mul = Mullite). Adapted from ACerS - NIST, *Phase Equilibria Diagrams CD-Rom database, version 3.1, NIST standard reference database 31, 2-5 users.* 2004-2005 [9]. 17

Figure 4: Lattice constants, a, b and c of mullite dependent from the Al_2O_3 content of the phase [39, 40]. 22

Figure 5: Fracture toughness K_{IC} as functions of the amount of mullite powder in the initial composition of mullite – zircon composites [27] 27

Figure 6: Relationship between wear rates and applied load for alumina/ mullite composite as after Luo H.H. et al. [52]. 29

Figure 7: K_{IC} of mullite/SiC composites as a function of SiC content: (a) mullite derived from sol-gel powder and hot pressed at 1650^{o}C for 1.5h under 15 MPa pressure; (b) mullite derived from kaolinite/α-alumina and hot pressed at 1600^{o}C for 1.5h under 15MPa pressure [7]. 32

Figure 8: Structure of diamond [56] 36

Figure 9: The *P-T* equilibrium phase diagram for C; A, B and C specify regions of metastability for the phase undergoing spontaneous transformation. [62] 38

Figure 10: Hot Press [65] 44

Figure 11: Graphite pot and piston configuration..... 47

Figure 12: Average particle size analysis of alumina and silica mixture in 3:2 molar ratios..... 54

Figure 13: XRD results of samples by sol/gel process 58

Figure 14: XRD of composite samples each with 10wt% diamond added and sintered at the various temperatures under investigation. Samples *MRD1/1400/Ar, MRD1/1450/Ar & MRD1/1500/Ar*..... 59

Figure 15: SEM micrograph of as received silica powder..... 60

Figure 16: Overall EDS of as received Silica Powder..... 60

Figure 17: SEM micrograph of as received silica powder..... 61

Figure 18: Overall EDS of as received alumina powder 61

Figure 19: SEM micrograph of milled alumina and silica in 3:2 stoichiometric composition for mullite..... 62

Figure 20: Overall EDS of milled alumina and silica in 3:2 stoichiometric composition for mullite..... 62

Figure 21: SEM micrograph of milled alumina and silica in 3:2 stoichiometric composition for mullite plus 10wt% diamond..... 63

Figure 22: Overall EDS of milled alumina and silica in 3:2 stoichiometric composition for mullite plus 10wt% diamond..... 63

Figure 23: SEM micrographs of cut and etched (A) and un-etched (B) surfaces of compact sample *MRD1/1400/Ar*. See spot analysis of the etched surface in proceeding figures. 64

Figure 24: SEM micrograph (2k magnification) and spot EDS of sample *MRD1/1400/Ar*, etched surface..... 64

Figure 25: SEM micrograph and overall EDS of un-etched surface of compact sample *MRD1/1450/Ar*..... 65

Figure 26: SEM micrograph (2k magnification) and spot EDS for the un-etched sample *MRD1/1450/Ar*..... 65

Figure 27: SEM micrographs of cut and etched (C) and un-etched (D) surfaces of compact sample *MRD1/1500/Ar*. See spot analysis of the etched surface in proceeding figures. 66

Figure 28: Overall EDS of etched (E) and un-etched (F) surfaces of compact sample *MRD1/1500/Ar.*..... 66

Figure 29: Spot analysis and EDS of etched compact sample *MRD1/1500/Ar* at 2k magnification 66

Figure 30: Spot analysis and EDS of etched compact sample *MRD1/1500/Ar* at 2k magnification 67

Figure 31: Spot analysis and EDS of etched compact sample *MRD1/1500/Ar*, the marked point shows is the grain boundary between alumina and silica phases at 20k magnification. 67

Figure 32: Raman Spectroscopy analysis for sample MRD1/1400/Ar..... 68

Figure 33: Raman Spectroscopy analysis for sample MRD1/1450/Ar..... 69

Figure 34: Raman Spectroscopy analysis for sample MRD1/1500/Ar..... 69

Figure 35: Raman Spectroscopy analysis for sample MRD1/1500/Ar – Second Examination using a different grating to the previous analysis (Figure 34 above) to give a larger spectral range, so that lower wavenumber peaks will also be visible if present. ... 70

Figure 36: Graphic representation of hardness against temperature for samples *MR1/1400/Ar, MR1/1450/Ar and MR1/1500/Ar* (no – diamond added) and samples with 10wt% diamond added, i.e. samples *MRD1/1400/Ar, MRD1/1450/Ar & MRD1/1500/Ar*. Fracture toughness against temperature for samples with no diamond added is also plotted. 77

Figure 37: XRD trace for compact *MRD1/1400/Ar*..... 90

Figure 38: Plot of Identified Phases for *MRD1/1400/Ar* 91

Figure 39: XRD trace for compact *MRD1/1450/Ar*..... 92

Figure 40: Plot of Identified Phases for MRD1/1450/Ar 93

Figure 41: XRD trace for compact *MRD1/1500/Ar*..... 94

Figure 42: Plot of Identified Phases for *MRD1/1500/Ar* 95

Figure 43: XRD trace for compact *MR1/1600/Ar* 95

Figure 44: Plot of Identified Phases for *MR1/1600/Ar* 96

Figure 45: XRD trace for compact *SG/1000/A* 97

Figure 46: XRD trace for compact *SG/1200/A* 97

Figure 47: XRD trace for compact *SG/1400/A* 98

Figure 48: XRD trace for compact *SG/1600/A* 98

List of Tables:

Table 1: Structural data of 3:2 and 2:1 mullites as after Schneider H. and Komarneni S., *Mullite.* Wiley-VCH, Weinheim, 2005: p. 46-70 [39]. 22

Table 2: Comparison of physical properties of diamond, alumina, mullite and diamond/ alumina composite. Data to construct this table was quoted from sources [1, 6, 7, 27, 40, 45-48]. 24

Table 3: Summary of properties of materials investigated by Zhang F.C. [49] 27

Table 4: Physical properties of alumina/ mullite composites after [52]. 30

Table 5: Chemicals used in the research work 40

Table 6: As received particle size analysis 54

Table 7: Milled Alumina-Silica Mixture (See section 3.2 for the milling conditions) 54

Table 8: Overview of result – sinter mullites method 56

Table 9: Elemental spot analysis of figure 21 65

Table 10: Elemental spot analysis of figure 23 65

Table 11: Elemental spot analysis of figure 28 67

Table 12: Criterion satisfaction of equation (ii), section 3.13, for fracture toughness calculation after [67]. 71

Table 13: Hardness and fracture toughness results 72

Table 14: Comparison of physical properties of some of the mullite composites reviewed in chapter two of this work to physical properties obtained from sintered compacts..... 81

Table 15: Green and sintered density measurements for the compacts obtained by the sinter mullite method 85

Table 16: Determination of density of compacts by sinter mullite method using the Archimedes method 86

Table 17: Hardness and fracture toughness measurements from samples *MR1/1400/Ar* and *MRD1/1400/Ar*, i.e. compact sample with no diamond and with added 10wt% diamond respectively 87

Table 18: Hardness and fracture toughness measurements from samples *MR1/1450/Ar* and *MRD1/1450/Ar*, i.e. compact sample with no diamond and with added 10wt% diamond respectively 88

Table 19: Hardness and fracture toughness measurements from samples *MR1/1500/Ar* and *MRD1/1500/Ar*, i.e. compact sample with no diamond and with added 10wt% diamond respectively 89

Table 20: Identified X-ray patterns list for *MRD1/1400/Ar* 90

Table 21: Identified X-ray patterns list for *MRD1/1450/Ar* 92

Table 22: Identified X-ray patterns list for MRD1/1500/Ar..... 94

Table 23: Identified X-ray pattern List for *MR1/1600/Ar*..... 96

Chapter 1: Introduction

1.0 Background and Motivation

This work is part of the investigation into economical alternative to diamond coated/polycrystalline diamond (PCD) materials for abrasion resistant applications. Similar investigations were carried out by A.M. McKie, et al, [1]; their work involved synthesis of diamond/ alumina composites through hot uni-axial pressing to an achieved density of 96% of theoretical and a hardness of approximately 20GPa.

Alumina and silica react to form alumino-silicates with intrinsic refractory and abrasive properties; the most prominent product of such reactions is mullite. The reason for choosing mullite over alumina is that mullite has a low coefficient of thermal expansion; this makes it more resistant to thermal stress in contrast to materials prepared from aluminium oxide. Mullite possesses a dielectric constant of approximately 5 or 6 and therefore is a very attractive material for use in integrated circuits. Mullite is the most stable compound in the Al_2O_3-SiO system. [2-4]. Mullite however has been reported to possess low fracture toughness ~2.0 $MPa{\cdot}m^{1/2}$ [5] and 2.5 $MPa{\cdot}m^{1/2}$ [6]. Secondary reinforcement phases can be added to the mullite matrix to improve the fracture toughness and other physical properties such as hardness. In this case the secondary phase increases fracture toughness through firstly crack deflection and secondly, modulus-load-transfer which is believed to increase toughness by transferring stresses at a crack tip to regions remote from the crack tip, so decreasing the stress intensity at that point [7]. Diamond has been used as reinforcing phase despite its tendency to oxidise

and phase transform to graphitic structures or per say "non-diamond forms". [1, 8]. Other processes that cannot be ruled out are the interaction of the diamond with silica resulting in SiC or SiO and CO under the synthesising conditions. Diamond addition is expected to improve fracture toughness as well as hardness. It is the expectation of improved fracture toughness offered by such a secondary phase and because of the advantages of mullite over alumina that motivated for this work, which involves the fabrication and study into the physical properties of mullite/ diamond composites and comparison of the same to other composites with mullite phase forming the matrix of the composite. The study also seeks to explore the benefits of mullite/ diamond composites in different applications.

1.1 Project Overview

Two methods were used to investigate the synthesis of mullite itself before addition of diamond to the starting powders. The first method was the use of solid state reactions to produce sintered mullites (sinter mullites method). In this case the starting materials (alumina and silica) were intimately mixed in stoichiometric compositions to form 3:2 mullites ($3Al_2O_3 \cdot 2SiO_2$). 18mm diameter compacts were produced from the dry milled powders. The compacts were then hot pressed in an argon atmosphere at a temperature at which if diamond was present, graphitisation will not occur or will occur to a much lesser extent; in this case the final hot press sintering temperatures investigated were 1400, 1450 and 1500^{o}C [8]. McKie et al [1] investigated the physical properties of diamond composites hot pressed at 1500^{o}C, however thorough investigations on the amount of diamond left after sintering or the extent of graphitization was not done. Full mullitisation

using the sinter mullite method tends to occur at temperatures above 1600^{o}C [9]; however the process of mullite formation begins at around 1050^{o}C [10, 11] with formation of acicular shaped primary mullites that grow into needle shaped secondary mullite with increase in temperature and time. Other methods used to aid mullitisation process would be to add up to 30% mullite powder to the stoichiometric starting powders (alumina and silica). In this case the mullite acts as a nucleus or "seed" that allows the reaction between aluminium oxide and silica to proceed to its equilibrium state at a sintering temperature in the range 1300 – 1600^{o}C [2]. This method however did not form part of the scope of this work.

On successful hot press sintering to produce a mullite compact by the sinter mullite method, 18mm diameter compacts of the dry milled powders in mullite stoichiometric composition were produced with 10wt% diamond (2μm particle size) added to form part of the compacts. The compacts were then hot press sintered to the maximum temperatures under investigations (1400, 1450 and 1500^{o}C) to try and synthesize a diamond/ mullite composite.

The second method attempted for mullite synthesis was the sol/ gel method. The overall aim was to attempt to synthesize pure mullite with less residual silica and alumina phases. The method evolved towards the formation of a gel-like diphasic system containing both a liquid phase and solid phase whose morphologies range from discrete particles to continuous polymer networks [12]. Aluminum alkoxide and silicon alkoxide were mixed in their stoichiometric Al/Si atomic ratio (weight) for the formation of 3:2 mullites ($3Al_2O_3{\cdot}2SiO_2$). In this method the resulting dried amorphous powders were used to produce 18mm diameter compacts which were sintered in a muffle furnace at trial initial

temperature of 1000^{o}C. Given a successful mullite compact from this second attempted method, 18mm diameter compacts from the dried amorphous powders would have been produced with 10wt% diamond added to try and synthesize a diamond/ mullite composite by hot pressing the compacts. It is reported by some authors that the mullite crystallization temperature using this method takes place at above 980^{o}C to less than 1000^{o}C [13]. The main focus of this work however is on compacts produced by the first method, that of sinter mullites.

Chapter 2: Literature Review

2.1 Composite Materials - General

Most composite materials show marked anisotropy – i.e. their properties vary significantly when measured in different directions as a result of crystallographic texture (preferred orientation). In making artificial composite materials, the potential for controlled anisotropy offers considerable scope for integration between the processes of material specification and component design. Large anisotropies in stiffness (Young's Modulus) and strength are possible and must be taken into account during design [14].

There are several different types of composites. More recently, there has been considerable interest in metal matrix composites (MMCs), such as aluminium reinforced with ceramic particles or short fibres, and Ti containing long fibres. The property enhancements being sought by the introduction of the reinforcements are often less pronounced than for polymers, with improvement in high-temperature performance or tribological properties often of interest. Ceramic based composites are also under study with the main objective of imparting toughness to the matrix by the introduction of other constituents, since the stiffness and strength are unlikely to be much affected. Such materials are still, for the most part, in the early stages of development, partly because they are rather difficult to manufacture [14].

Lastly when composite materials are subject to temperature changes (during manufacture and/ or in service), a mismatch between the thermal expansivities of the constituents

leads to internal residual stresses. These can have a pronounced effect on the mechanical behaviour of these materials [14]. The thermal residual stresses are of sufficient magnitude to generate lattice defects such as dislocations around the particle even in ceramic materials. The thermal residual stresses also depend on the change in temperature, Poisson's ratio and Young's modulus of the particle and matrix [15].

2.2.1 Physical Properties of Composites

Properties of composites can be obtained through estimation by "rules of mixtures" which maybe based on a number of simplifying assumptions. One such assumption is that a composite property is the volume weighed average of the properties of the phases (matrix and dispersed phase) [16]. The following subsections give background and different rules of mixtures used in estimating physical properties of composite materials.

2.1.1.1 Modulus of Elasticity

The normal modulus of the particulate composite is given by: [17]

$$E_{pc} = \frac{V_f^{0.67} E_b}{1 - V_f^{0.33} \cdot \left(1 - \frac{E_b}{E_p}\right)} + \left(1 - V_f^{0.67}\right) E_b$$

Where: E_{pc} = Normal modulus of elasticity of the particulate composite.

E_b, E_p = Modulus of elasticity of binder (matrix) and dispersed particle phase respectively

V_f = Volume fraction of the particles, given by expression: $A_f / (A_f + A_m)$

where A_f and A_m are the cross sectional areas of fibre and matrix respectively.

2.1.1.2 Density

$$\rho_c = (1 - f)\rho_m + f\rho_f$$

Where: ρ_c = Density of composite

ρ_m, ρ_f = Density of matrix and dispersed phase respectively

f = Volume fraction, given by expression: $A_f / (A_f + A_m)$

where: A_f and A_m are the cross sectional areas of fibre and matrix respectively

2.1.1.3 Brittleness Factor

The hardness and brittleness of ceramics are strongly interrelated. Fracture is not only an interference in the measuring of Vickers or Knoop hardness, but is an integral part of the hardness response of ceramic materials. Hardness versus load curves exhibit a dramatic transition point at which hardness becomes load independent. The transition corresponds to the onset of extensive micro-fracturing and is directly related to a new parameter:

$$B = H_v E / K_{IC}^2$$

The value ***B*** (units 1/m), quantifies the brittleness of ceramics. A brittleness factor of X < 1 implies that the ceramic material is relatively brittle, non-elastic and deformable [18].

2.1.2 Toughening Mechanisms in Composites

There are several methods of improving toughness in ceramic composite materials. These include; crack deflection, micro-cracking, transformation toughening, crack branching, crack pinning, crack bowing, plasticity in metallic phase, compressive matrix residual stresses, matrix micro-cracking, frictional interlocking, crack bridging and fibre pull-out. All these mechanisms in particular redistribute stress at the crack tip and increase the energy needed to propagate a crack through the composite material and thus resulting in improved toughening [19, 20]. Thermal residual stresses are inevitable during manufacture of composite materials as a result of the differences in thermal expansion coefficients between the hard inclusions and the matrix. The stresses will influence the direction of crack propagation initiated in the matrix or reduce the stress intensity factor at the crack tip [21, 22].

The above toughening mechanisms lead a material to a more crack tolerant behaviour as toughness is increased with increasing crack length (R-curve behaviour – toughness against crack extension curves) and consequent increase in degrees of energy dissipation by plastic deformation as the crack grows [23, 24]. The rise which is noted in the in the R-curves and the plateau value which is found for the toughness depend on the microstructure and on the chemical composition of the ceramic as well as on the history

of the crack prior to the crack extension [24]. The magnitude of toughness increase is related directly to the ability of the ductile particles to perform plastically, span the faces of a propagating crack and impose closure tractions which reduce the stress intensity at the crack tip [23].

As a consequence, the two mechanical fracture parameters namely strength, σ_B, and toughness, K_{IC}, can be associated with the critical crack length, a_c, by way of a crack instability criterion as proposed by Griffith.

$$\sigma_B = (1/Y)*(K_{IC}/\sqrt{a_c})$$

Y is a parameter which is dependent on the crack and sample geometries. The equation shows directly the strength improvement which is to be expected through a reduction in the defect size, as well as indicating that changes in the toughness exert as even stronger influence on the fracture stress [24].

The following sections will pay attention to a few of the mechanisms listed above. Figure 1 below illustrates different toughening mechanisms as explained in proceeding sections.

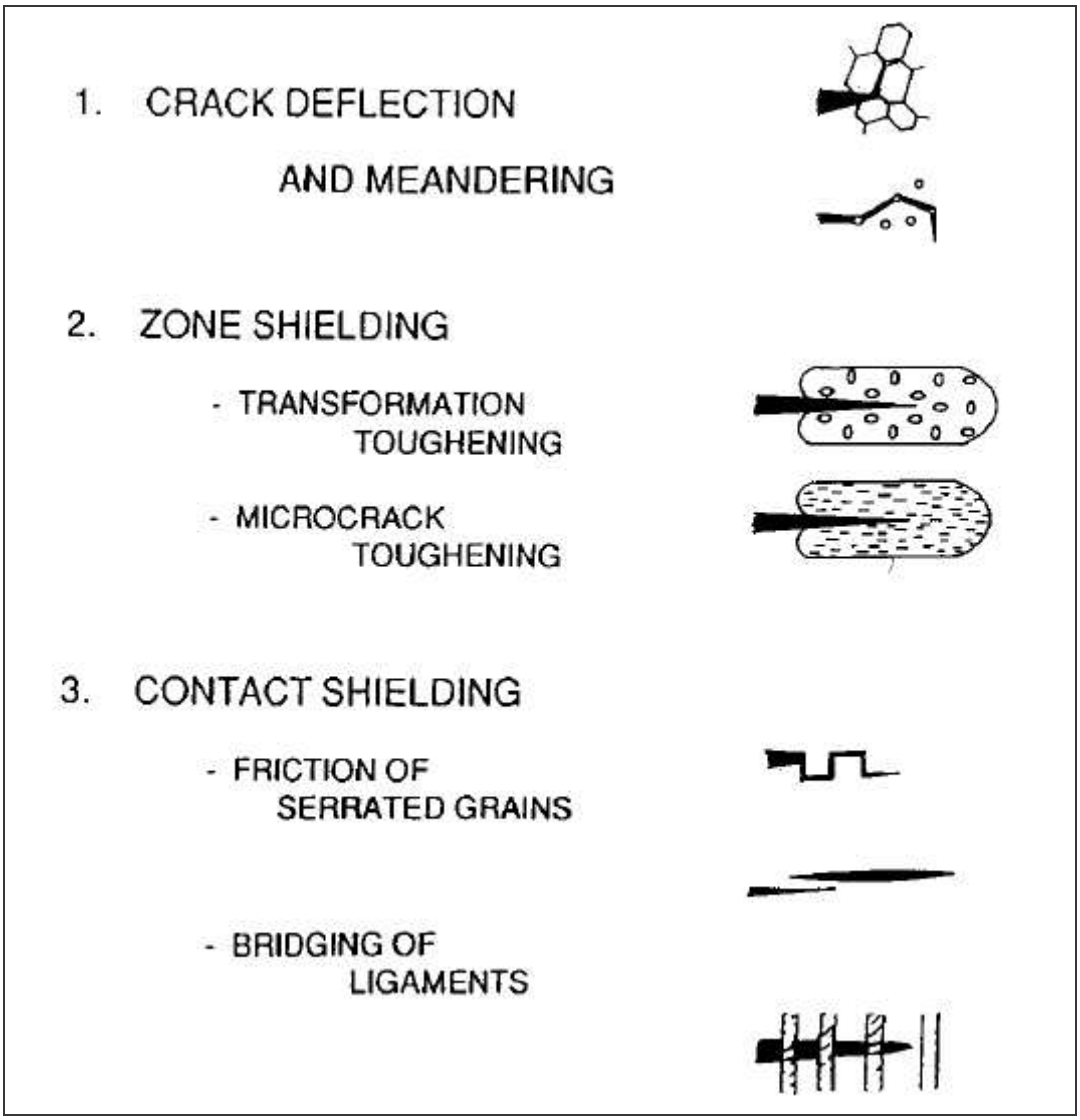


Figure 1: Schematic representation of toughening mechanisms in structural ceramics, after Ritchie [25], and as modified by [24].

2.1.3 Fibre Reinforcement Toughening Mechanisms

Fibre reinforcement combines crack bridging, fibre pullout, and crack deflection mechanisms. As an overall toughening technique, it appears to give the greatest improvement. Further, the use of metal fibres adds the toughening mechanism that comes from the plasticity of the metallic phase [20]. The proper characterization of bond at the fibre-matrix interface is a key element for understanding the behaviour, and for modelling

the response under load of high performance fibre reinforced cement and ceramic-based composites. It allows for the rational prediction of their mechanical, fracture, and ductility properties. From a mechanical viewpoint, it has been shown that the bond at the fibre-matrix interface can be best characterized by a bond stress versus slip relationship. However, the nature of bond in these systems is very complex, involving a cohesion/adhesion component, a decaying frictional component affected by radial stresses, and a mechanical component [26].

Crack Deflection Dependent Mechanism: Crack deflection occurs in the case of intercrystalline fracture. The development of composites with localized internal stresses and with crack deflecting second phases (particles, platelets, whiskers, fibres) use the effect of crack deflection. The extent of crack deflection does not in general increase with crack length so that long crack R-curve behaviour and a corresponding crack tolerance cannot be expected. R-curve behaviour requires in general toughening mechanisms which increase in effective with increasing crack length [24]. Figure 2 below shows an illustration of crack deflection and interlocking.

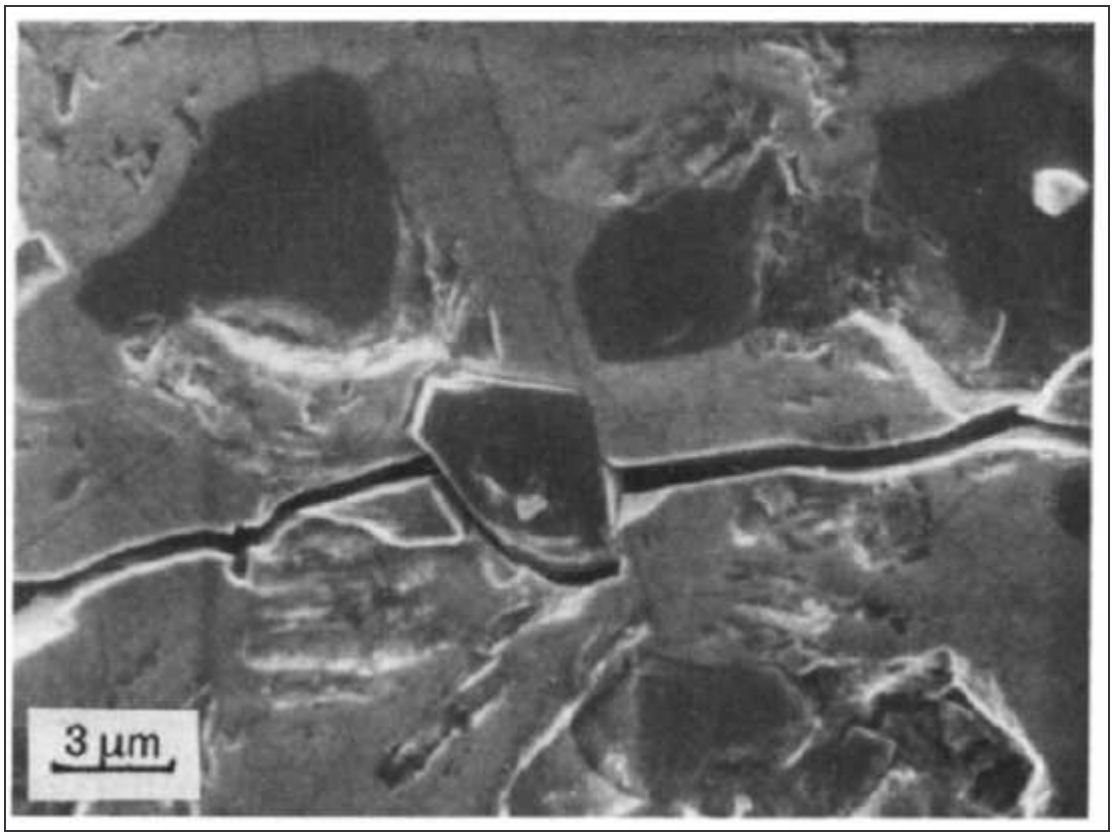


Figure 2: Crack path in SiC-TiB_2 composite ceramics. The incorporated TiB_2 grains show dark contrast, after Steinbrech [24].

Shielding of the Crack Tip: Shielding of the crack tip arises from an increasing screening of the crack tip from the applied stress as the crack grows. This condition is automatically fulfilled if the effects which depend upon the microstructure are intensified with growing crack length. The wake-controlled R-curve behaviour which arises from screening effects in the region of crack surfaces can have its origins in mechanisms involving process zone screening and/ or contact screening [24].

Zone Screening: Zone screening occurs as a toughening effect if structural elements in a process zone surrounding the crack display hysteresis in their stress-strain behaviour [24].

Contact Screening: Contact screening has its origins in localised interactions at the crack face. Material bridges which can cause crack closing forces at the crack faces can take the form of unbroken or partially fractured grains or interlocking grains or inclusions (platelets, whiskers, fibres, metallic phases). These bridge the crack and hinder crack opening. For a separation of the crack surfaces, additional energy is needed which then appears in macroscopic terms as a increased toughness [24].

As a note, it has been reported [23] that experimental work for composites which are reinforced with a discontinuous particulate phase, some cases resulted in positive toughening increment on crack-particle interaction while some did not. The latter cases occurred when matrix cracks were not attracted to the ductile particles due to unfavourable residual stress and Young's modulus mismatch conditions. The dominant toughening mechanism may thus be for example crack branching or crack bridging [23].

2.2 Mullite

Mullite is a structural refractory ceramic with nominal composition that ranges from $3Al_2O_3 \bullet 2SiO_2$ to approximately $2Al_2O_3 \bullet SiO_2$. It is the only crystalline phase in the aluminosilicate system, under normal atmospheric pressure from room to elevated temperature [27]. Mullite finds wide applications in the refractory industry because of its intrinsic physical properties including superior high temperature mechanical stability, excellent electrical insulating ability, resistance toward chemical attack, low thermal expansion coefficient ($4 \times 10^{-6}/^{o}C$ in the 20-200 ^{o}C range) which is comparable to that of

silicon (3.5 x 10^{-6}/^{o}C), creep resistance, low density (3.17g/cm^{3}), low thermal conductivity (k=2.0 W/m/K, low dielectric constant (ε=6.5 at 1MHz) [28] etc. The interlocking grain structure of mullite contributes to an improved fracture toughness of the whole ceramic body. The commercial production of mullite from pure silica and alumina occurs at high temperatures which obviously make the production route expensive. Some silica - alumina clays (kaolinite, pyrophyllite, etc) have been used in the production of mullite. These contain impurities that tend to lower the liquid formation temperature thus allowing for liquid phase sintering. The production of mullite from clays has been studied. The kaolinite clay is used in most of the studies [29-31]. Two types of mullite (primary and secondary) have been shown to occur during thermal transformations of silica – alumina clays. Primary mullite (2:1) is the first to form and is derived from firing of the clay component in whiteware bodies at temperature around 1050^{o}C whereas secondary mullite (3:2) results from interaction of the clay component with any fluxes (typically alkali-rich feldspars) [29, 32] at higher temperatures in excess of 1400^{o}C – 1600^{o}C. Primary mullite has a fine, cuboidal or scaly morphology and secondary mullite has an acicular morphology [29]. In some studies tertiary mullite has been observed to precipitate from alumina-rich liquid adjacent the alumina filler [32]. Energy dispersive spectroscopy (EDS) examination of mullite from clay is difficult due to the fact that mullite grains grow while embedded in an aluminosilicate glass matrix [29].

Pyrophyllite (a hydrous aluminium silicate) has been shown to result in thermal transformations that lead to the formation of mullite and cristobalite at temperatures ranging from 1050 to 1600^{o}C [10, 11]. Secondary mullite formation in sintering of

kaolinite clay takes place at a temperature above 1400 ^{o}C by dissolution of alumina into transient liquid phase, followed by precipitation of the mullite crystals [30, 33]. The rate of mullite formation is said to be very slow till the eutectic liquid formation at 1587 ^{o}C and fast at 1600^{o}C [30, 34]. Mullite content is however controllable by extending heat treatment time and temperature. Other variables affecting mullite formation include type of flux, levels of alkali and Fe impurities (act as mineraliser supporting mullite growth in clay based systems) and the atmosphere in which mullitisation takes place. Heat treatments in oxidising atmosphere favour larger primary and secondary mullite crystals than in reducing atmosphere [29]. These variables influence mullite formation by affecting the composition and viscosity of the liquid in which it grows.

2.2.1 Mullite Formation

Carl L. Eggerding et al [2] in their patent claim a method of forming a ceramic material which includes mullite ($3Al_2O_3 \cdot 2SiO_2$) in any desired percentage. The mullite in this case is first added to act as a nucleate or "seed" that allows the reaction between aluminium oxide and Silica to proceed to its equilibrium state. If the mullite is not added alpha alumina and Silica would not form any mullite; however, the mixture of alpha alumina and silica would sinter to a 0% apparent porosity. Any desired amount of mullite can be formed up to substantially 100%. In order to form 100% mullite ceramic material the stoichiometric amounts of alumina and silica are combined with the initial mullite seed. During sintering the components are formed into mullite at temperatures from a minimum of 1300^{o}C. If less than 100% mullite is desired, the ratio of total alumina

content to silica content must be in excess of stoichiometric ratio. After reaction, this will leave the desired mullite plus alumina phase structure[2]. The patent has examples of sintering of the mixture done in the range 1300 – 1600^{o}C wherein the alumina and silica reacted to form mullite under the influence of the initially added mullite.

William B. Hillig et al [4] further patented work on mullite by reactive hot pressing as well as work on mullite matrix composite. In all this work a mixture of alumino-silicate glass and alumina having a composition corresponding to mullite and containing a nucleating mullite powder was used to produce a dense polycrystalline mullite body having an average grain size of less than 15μm [3, 4].

Silica in all cases is added to promote densification of the particulate mixture and the medium in which aluminium oxide and silicon dioxide react to form mullite. The reaction to form mullite is not possible unless some minimum amount of mullite is added to the raw material mixture [2].

2.2.2 Other Methods of Forming Mullite

Mullite formation can be deduced from the fact that the equilibrium Al_2O_3-SiO_2 phase diagram (see figure 3 below) predicts that if alumina and silica are in contact and heated sufficiently, mullite will form as a natural product. This technique requires the Alumina and Silica to diffuse to a common boundary and react chemically. The distance the constituents diffuse is primarily influenced by the temperature, the time the material is held at temperature, and the particle size of the raw materials. The rate decreases rapidly with increase in the diffusion distance. Therefore, the reaction is interrupted before

completion of the simultaneously occurring sintering reaction. In other patented work [35] flame pyrolysis is said to be used to prepare ultra-fine Al_2O_3 and SiO_2. This technique drastically reduces the diffusion distance and makes possible the production of 100% mullite and complete sintering to 0% open porosity. However the utilization of such ultra-fine particle size in a sheet casting technique for sample fabrication was reported to be very difficult, if not impossible [2, 35].

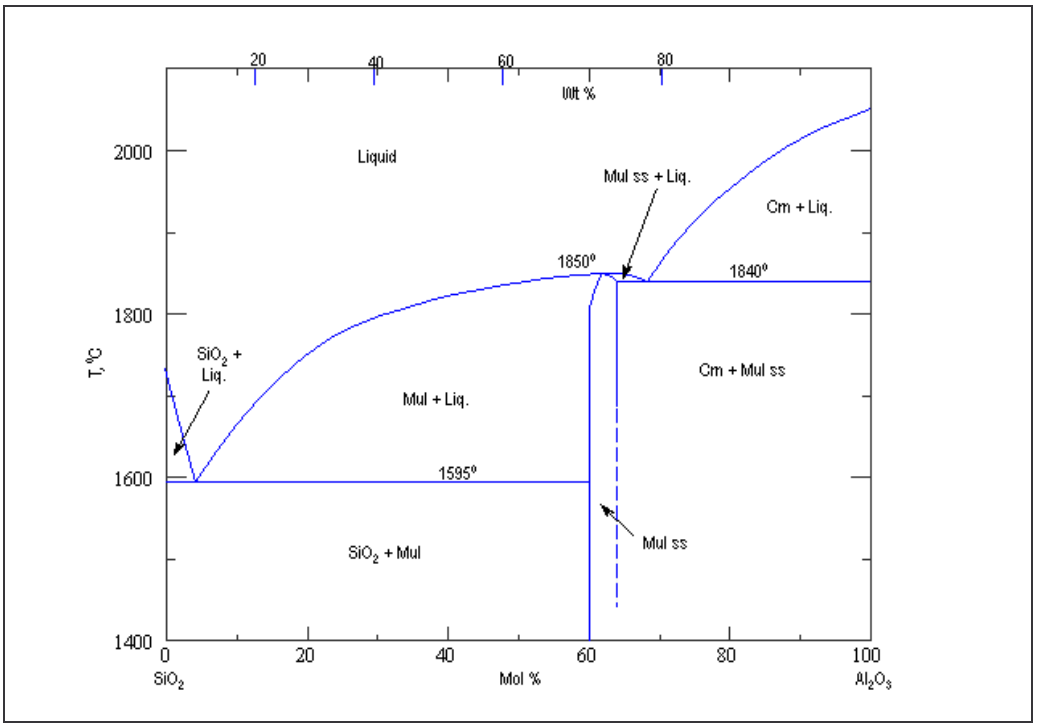


Figure 3: System Al_2O_3-SiO_2; (Cm = corundum, Mul = Mullite). Adapted from ACerS - NIST, *Phase Equilibria Diagrams CD-Rom database, version 3.1, NIST standard reference database 31, 2-5 users.* 2004-2005 [9].

2.2.3 Mullite Preparation: Sol-gel process

The **sol-gel** process is a wet-chemical technique (a.k.a. chemical solution deposition) widely used recently in the fields of materials science and ceramic engineering. Such methods are used primarily for the fabrication of materials (typically a metal oxide) starting from a chemical solution which acts as the precursor for an integrated network (or *gel*) of either discrete particles or network polymers. Typical precursors are metal alkoxides and metal chlorides, which undergo various forms of hydrolysis and polycondensation reactions. The formation of a metal oxide involves connecting the metal centers with oxo (M-O-M) or hydroxo (M-OH-M) bridges, therefore generating metal-oxo or metal-hydroxo polymers in solution. Thus, the sol evolves towards the formation of a gel-like diphasic system containing both a liquid phase and solid phase whose morphologies range from discrete particles to continuous polymer networks [12]. Bulent E. Yoldas et al [36], patented work on formation of mullite using silicon alkoxide and aluminum alkoxide. In their patent they claim a method for preparing mullite which comprises the steps of:

(a) Partially hydrolyzing a solution of a silicon alkoxide in an alcohol by adding about 0.1 to 1.0 moles of water per mole of stoichiometric mullite to said silicon alkoxide solution;

(b) Adding a solution of an aluminum alkoxide in an alcohol to the resulting partially hydrolyzed silicon alkoxide solution in a ratio of 3 moles of aluminum alkoxide per mol of silicon alkoxide to provide a solution having a concentration of not greater than about 10 percent by weight equivalent oxide;

(c) Heating the resulting solution to a temperature about 50° to 0°C below the normal boiling temperature of the alcohol diluent for about 8 to 48 hours;

(d) Recovering an amorphous material having the mullite composition from said resulting solution; and

(e) Heating said amorphous material to about 985 °C thereby converting said amorphous material to crystalline mullite.

Calcination temperatures below 900 °C would yield poor results in the crystallization of mullite, while calcination temperatures exceeding 1600 °C would not affect the end use as a heat-resistant structural material but would lead to reduced surface area of the product when used as a combustion catalyst support. Differential thermal analysis of the product normally show a crystallization temperature of mullite at around 980 ^{o}C; a peak at 1300 ^{o}C is attributed to glass phase formation [13].

Aluminum alkoxide and silicon alkoxide are mixed at an Al/Si atomic ratio (weight) of 2:1 to 7:1 preferably 2.5:1 to 6.5:1 and more preferably 2.5:1 to 6.5:1. Al/Si atomic ratios less than 2:1 would result in excess silica during reaction growing into glass phase or cristobalite which tends to crystallize upon calcination. Conversely, more than 7:1 atomic ratios would lead to increased alumina content and hence less pure mullite product [13].

2.2.4 Advantages of the Sol/ Gel Method

The sol-gel method has the following advantages: very high purity ceramic can be obtained, because the former purification methods, such as distillation or recrystallization, have to be applied to liquids or alkoxides; highly homogenous multicomponent ceramics and composite ceramics can be obtained, since the energy and therefore the synthesis temperature, is low; it is possible to prepare various special types of material, for instance thin films, coatings, fibres, powders and so on, because it is easy to control reaction conditions [37]. The fact that low temperatures are employed in sol-gel process makes the process less expensive in light of energy costs despite the raw materials being expensive and large shrinkage of the compacts during firing which causes cracks in the materials [38].

2.2.5 Types of Mullite

As reported by Schneider et al [39], mullite displays variable Al to Si ratios with solid solution series $Al_{4+2x}Si_{2-2x}O_{10-x}$, with *x* ranging between about 0.2 and 0.9 (corresponding to about 55-90 mol% Al_2O_3). This however differs slightly with the phase diagram of figure 3 which shows mullite forming in the range 60 to about 66 Mol% Alumina. Different synthesizing methods can produce various types of mullite:

Sinter Mullites: Produced from the starting materials essentially by solid state reactions. Their alumina content is influenced by sintering temperatures, duration of the heat treatment, the initial bulk composition, the grain size and efficiency of mixing of the

starting materials and whether α-alumina nucleated. These mullites tend to have "stoichiometric", i.e., 3:2 composition ($3Al_2O_3{\cdot}2SiO_2$, i.e., approx 72 wt % Al_2O_3, x=0.25) [39, 40] and alumina contents with a frequency maximum at about 60 mol%.

Fused-mullites: Produced by either melting the raw materials in an electric arc furnace above 2000°C with subsequent crystallization of the mullite during cooling of the bath or by laboratory scale crystal growth techniques. Alumina contents are ideally at about 66.7 mol% (78 wt% Al_2O_3) maximum frequency. They are designated 2:1 mullite ($2Al_2O_3{\cdot}SiO_2$, x=0.40). It is also stated as a conclusion that formation of 2:1 or alternatively 3:2 mullites is controlled by synthesis process, while the bulk chemical composition of the system plays a less important role [39].

Chemically synthesized Mullites: These are sol-gel-derived mullites with compositions that are greatly dependent on the starting materials and temperature treatment. They are formed from organic and inorganic precursors by polymerisation and ceramization. Mullitisation takes place at low temperatures (900 -1300°C) with the low temperature mullites normally being Al_2O_3 rich (>90 wt% Al_2O_3, x>0.80) [39].

2.2.6 Structural Data of 3:2 and 2:1 Mullites [39]

The structural data including space group and lattice constants obtained for 3:2 mullite (x=0.25) and 2:1 mullite (x=0.40) are summarised in the table below in comparison to those of sillimanite.

Table 1: Structural data of 3:2 and 2:1 mullites as after Schneider H. and Komarneni S., *Mullite.* Wiley-VCH, Weinheim, 2005: p. 46-70 [39].

Composition, *x*	**Name**	**Space Group**	**Lattice Parameters**			
			a, Å	*b*, Å	*c*, Å	*V*, Å^3
0	Sillimanite	*Pbnm*	7.486	7.675	5.775	331.8 [41]
0.25	3:2-Mullite	*Pbam*	7.553	7.686	2.8864	167.6 [42]
0.40	2:1-Mullite	*Pbam*	7.588	7.688	2.8895	168.6 [43]
The *x*-value refers to the general composition of mullite $Al_{4+2x}Si_{2-2x}O_{10-x}$ giving the number of oxygen vacancies per unit cell.						

2.2.7 Lattice Constants for Mullite vs. Alumina content

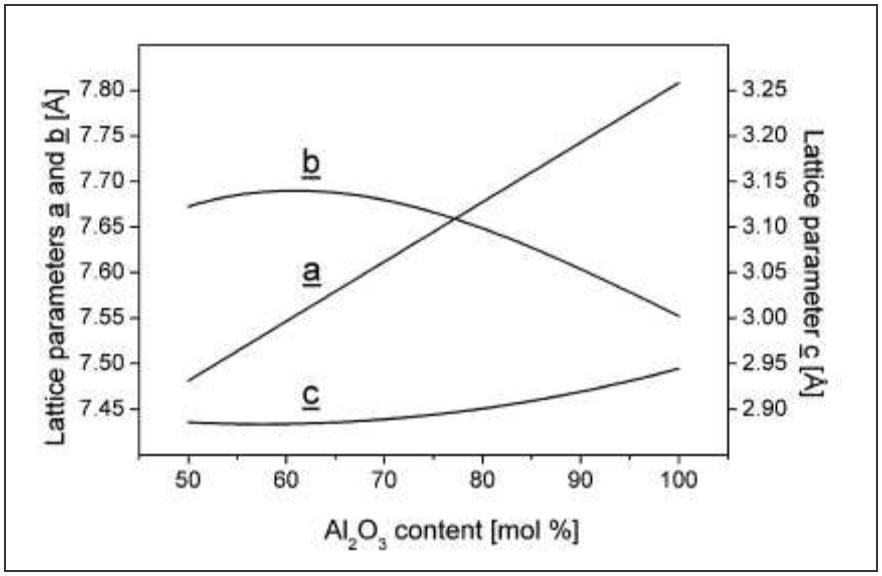


Figure 4: Lattice constants, a, b and c of mullite dependent from the Al_2O_3 content of the phase [39, 40].

If mullite is a simple solid solution with little structural variations, the cell parameters should depend linearly on the Al_2O_3 content. It has been shown that *a* lattice constant and the cell volume, V of the mullite actually increases linearly with the Al_2O_3 content, while *b* decreases slightly and non-linearly and *c* increases non-linearly. Extrapolation of *a* and

b curves towards *x*=0.00 (i.e., 50 mol% Al_2O_3 content) results in the lattice constants of sillimanite. At $a = b$, $x = 0.67$ (approx 80 mol% Al_2O_3) the phase formed is not tetragonal, but is better designated "mullite with pseudo-tetragonal" since the mullite symmetry is clearly orthorhombic [39, 40].

It is quoted in [39] that the mullite structure theoretically fits all compositions between (disordered) sillimanite ($x = 0.00$ in series $Al_{4+2x}Si_{2-2x}O_{10-x}$) and aluminium oxide with mullite structures (so called í-alumina, $x = 1.00$) and that there is no obvious reason why the composition should be restricted to 3:2 mullite ($x = 0.25$ in series $Al_{4+2x}Si_{2-2x}O_{10-x}$) or 2:1 mullite ($x = 0.40$ in series $Al_{4+2x}Si_{2-2x}O_{10-x}$) or to mixed crystals between them. Further to this, it is said there exists a miscibility gap between sillimanite ($x = 0.00$ in series $Al_{4+2x}Si_{2-2x}O_{10-x}$) and SiO_2-rich mullite ($x < 0.20$ in series $Al_{4+2x}Si_{2-2x}O_{10-x}$). The miscibility gap between sillimanite and mullite has been explained by the different formation conditions (sillimanite = moderate pressure, moderate temperature; mullite = low pressure, high temperature) and by different ordering schemes of the phases [40].

2.2.8 Mullite over Alumina

Mullite is the most stable compound in the Al_2O_3-SiO_2 system. It is an attractive high temperature structural ceramic material because of its high melting temperature, relatively low thermal expansion coefficient and thermal conductivity compared to alumina. As reported by Hillig W. B. et al [3] low thermal expansion coefficient makes mullite more resistant to thermal stresses in contrast to similar bodies prepared from aluminium oxide materials. However, pure mullite ceramics are relatively difficult

materials to produce. Conventionally made material does not have outstanding strength [3]. Mullite possesses a dielectric constant of approximately 5 or 6 and therefore presents a very attractive electrical characteristic in integrated circuits. However Commercially available mullite always contains significant amounts of impurities such as silica and iron oxide and titania which have an effect on the physical, electrical and chemical properties of the mullite. [17-19]. On the other hand aluminium oxide has exceptionally good properties like hardness, chemical inertness, melting point and wear resistance. However, alumina is a brittle ceramic material and it is strengthened by addition of secondary phase ceramic particles, fibres and whiskers in the alumina matrix [44]. Table 2 below gives a comparison in physical properties for alumina and mullite.

Table 2: Comparison of physical properties of diamond, alumina, mullite and diamond/ alumina composite. Data to construct this table was quoted from sources [1, 6, 7, 27, 40, 45-48].

Material	**H_v, GPa**	**σ_B, MPa**	**Comp. Yield Strength, MPa**	**K_{IC}, MPa·m$^{1/2}$**	**MP, ^oC**	**E, GPa**	**Density, g/cc**	**λ, $Wm^{-1}K^{-1}$**	**α, [x10^{-6}/^oC]**	**Crystal Structure**
Natural Diamond	30	-	4500-5800	3.40	-	700-1200	3.51-3.52	1000-10000	1	Cubic
Alumina	13.39	-	3000	4.0	-	370	3.96	30	5.5$^+$	Rhombohedral
Mullite	-	150-500	1310	1.5-3.0	~1830	204	3.13	-	4.5-5.5	
Diamond/ Alumina Composite*	24.19	-	-	3.7	-	498.4	3.85	-	-	-

* Recent work by [1], et al. Results quoted are those obtained using grade 12A results

$^+$ At 25 Degree Centigrade

2.3 Mullite Composites

The following subsections take a look at the synthesis and physical properties of some of the developed mullite composites by various authors, these include: zirconia-mullite; SiC-mullite; aluminium-mullite and alumina-mullite composites. The scope of this work investigates the physical properties of diamond-mullite composites. A physical properties comparison to other composites will be done in later sections.

2.3.1 Zirconia-Mullite Composites

Park et al [5] first points out that mullite could well develop even wider applications if its low fracture toughness (~2.0 MPa·m1/2) could be improved. The improvement comes by dispersing or precipitating metastable tetragonal zirconia particles in a mullite matrix resulting in monoclinic zirconia under an applied stress. Stress-induced phase transformation led to beneficial toughening mechanisms. The transformation toughening occurs most readily when the metastable t-ZrO_2 particles exist on the point of transformation. The transformation of t-ZrO_2 to m-ZrO_2 during cooling from sintering temperature depends on its chemical composition, grain size and shape. Consequently, it is necessary to retain any t-ZrO_2 at room temperature for enhancement of toughness of the composite. [5]. The most commonly used preparation route, low processing cost reaction sintering, of zirconia and mullite precursors has the disadvantage of difficulties in process control due to the simultaneous occurrence of densification and reaction. The work by [5] involved fabricating Y-PSZ/mullite by infiltrating partially sintered porous reaction mullite bodies with aqueous solution of zirconium and yttrium chloride hydrates which later decomposed during sintering. They concluded a mean four bend strength,

toughness and microhardness of composites (7.2wt% $Zr(Y)O_2$) with three repeated infiltrations and sintered for 10 hours at 1620^{o}C of 207MPa, 4.6 MPa·m1/2 and 853kg/mm2, respectively. A final sintered density of 94.6% of theoretical value with an apparent porosity of approx 1.2% was achieved.

Rendtorff N.M. et al [27] studied the influence of the different phase content and distribution for zircon-mullite composites with 15 – 45% mullite on physical properties and thermal shock resistance. The mullite content increased the zircon ($ZrSiO_4$) thermal dissociation with resulting product ZrO_2 positively influencing the mechanical and fracture properties of the composite through several combined mechanisms as compared to pure zircon. Figure 5 shows that fracture toughness increased with mullite addition from which the zirconia formation was enhanced.

The induced microcracks and the increase in the occurrence of transformation toughening were concluded in the investigation to promote the fracture resistance of these zircon-mullite composites.

Rietveld method was used to evaluate the amount of total zirconia for each composite. The zircon-mullite composite that was present around 4wt% of ZrO_2, i.e. composites with zircon as the matrix phase, had a fracture toughness around 2 MPa·m$^{1/2}$ and the zircon-mullite materials with approximately 10wt% of ZrO_2, i.e. composites that had a mullite matrix, had a fracture toughness around 2.5 MPa·m$^{1/2}$.

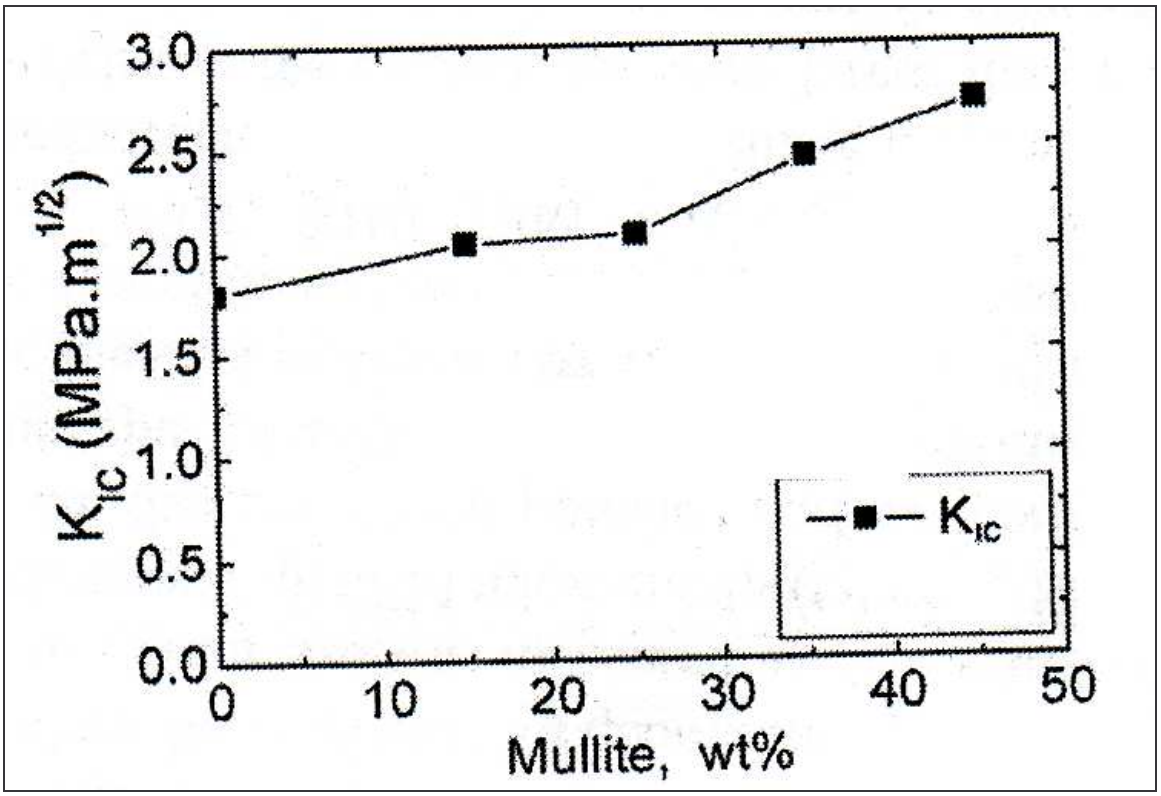


Figure 5: Fracture toughness K_{IC} as functions of the amount of mullite powder in the initial composition of mullite – zircon composites [27]

2.3.2 Aluminium/ Alumina-Mullite Composites

In previous investigations by Zhang F.C. et al [49] mullite was formed in situ after reaction sintering of alumina and SiC at 1600 in air. The summary of the properties of materials investigated are as shown in the table 3 below. Work by a different author [50] (ref: 11 in table 3 below) was included by Zhang F.C. et al for comparison purposes.

Table 3: Summary of properties of materials investigated by Zhang F.C. [49]

Material	ρ (%)	Grain size (μm)	σ_f (MPa)	K_{IC} (MPa m$^{1/2}$)	Hv (GPa)	E (GPa)	ν
Al_2O_3	98.2	2.4 ± 0.51	409 ± 34	3.30 ± 0.27	16.2 ± 0.5	350 ± 2	0.23
Al_2O_3/5 vol.% mullite	97.9	2.2 ± 0.36	494 ± 25	2.98 ± 0.21	16.9 ± 0.5	343 ± 3	0.23
Al_2O_3/5 vol.% SiC [11]	99.8	4.0 ± 1.1	646 ± 41	4.6 ± 0.1	–	–	–

Medvedovski E. [51] points out that the presence of mullite phase in alumina ceramics may have a positive effect on ceramic properties if the Al_2O_3 content does not exceed 98%. Reference is made to alumina ceramics with an Al_2O_3 content of 72-76% containing mullite and aluminosilicate with demonstrated flexural strength of up to 350MPa. In other investigations by the same author alumina ceramics with some quantity of mullite phase reinforcing a glassy phase exhibited high wear resistance comparatively superior to different kinds of alumina ceramics with higher Al_2O_3 contents but with only corundum crystalline phase bonded by a glassy phase. Further to this, a high content of the glassy phase was found to greatly affect ballistic performances of the ceramic when tested for armor applications though addition of mullite lowered the bulk density of the composite [51].

Luo H.H. et al [52] demonstrated the wear resistance of alumina/ mullite composite with a mullite content of 0.96 – 8.72 vol%. The composites were subjected to an abrasive wear test under loads of 0.1 – 2.0N with a ball-on-disc apparatus described in the same work. The composites were found to have higher wear resistance by a factor of 1 – 2 than that of pure alumina. They further conclude that fracture wear mechanism is operating in alumina and a combination of fracture and plastic wear mechanism is operating in the alumina/ mullite composites. Modes of wear were further explained by adhesion theory to support the stable wear resistance as observed the loads were increased to be higher than 0.4N. Figure 6 and table 4 below shows results of their findings:

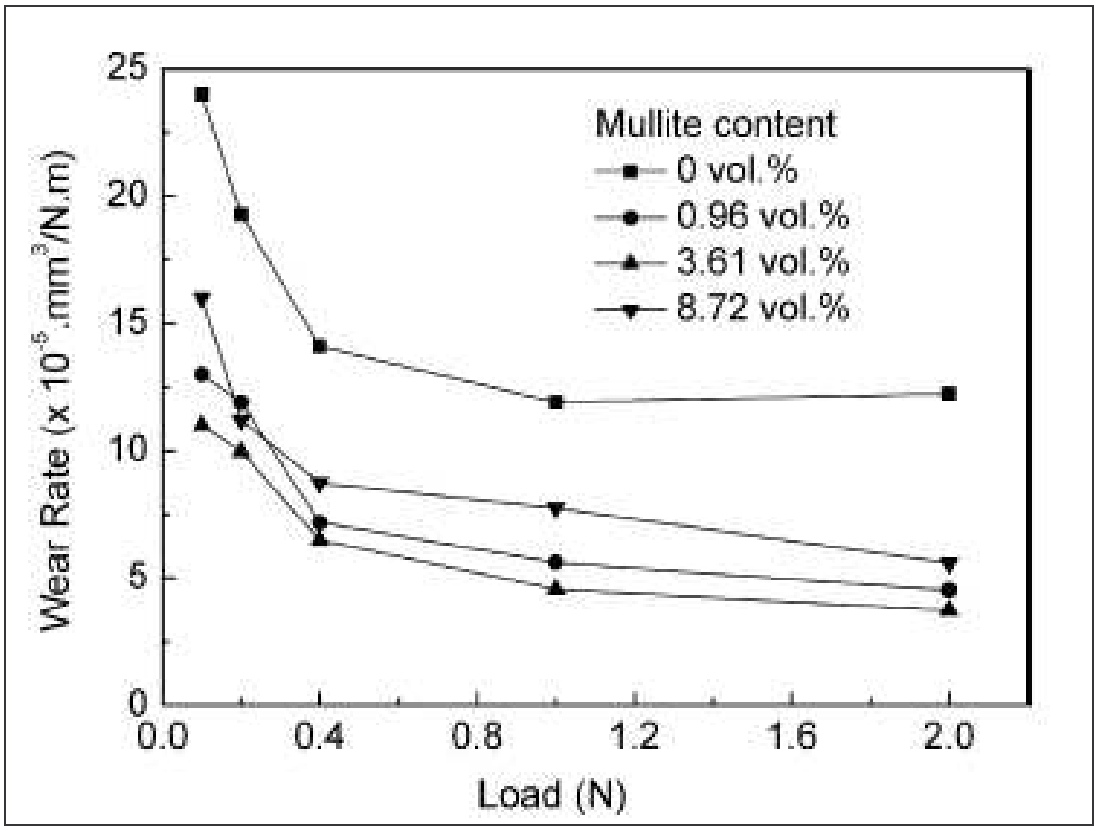


Figure 6: Relationship between wear rates and applied load for alumina/ mullite composite as after Luo H.H. et al. [52].

The addition of mullite resulted in reinforcement of the matrix grain boundaries and a substantial reduction in wear rates compared with the monolithic. The better wear resistance of the alumina/ mullite composites compared to alumina was explained by the reduction of the area fraction of pullout on the worn surface caused by the change in fracture mode. [52]. The sample with the 3.61 vol% mullite had the best wear resistance under the conditions the investigations were performed.

Table 4: Physical properties of alumina/ mullite composites after [52].

Mullite content, vol%	Mean grain size, µm	Relative density, %	H, GPa	K_{IC}, MP·m$^{1/2}$	E, GPa
0	2.4 ± 0.5	98.1 ± 0.4	16.2 ± 1.5	3.3 ± 0.3	350 ± 2
0.96	2.7 ± 0.5	97.6 ± 0.5	17.1 ± 1.8	3.2 ± 0.2	352 ± 5
3.61	2.2 ± 0.4	97.9 ± 0.5	16.9 ± 1.1	3.0 ± 0.2	343 ± 3
8.72	2.0 ± 0.3	97.5 ± 0.3	18.2 ± 1.5	2.6 ± 0.2	357 ± 2

In previous demonstrations by Taktar S. et al [53] friction and wear behaviour of alumina and alumina/ mullite composites, coupled with WC-6%Co ball, were investigated using a ball-on-disc apparatus at different sliding speed and load. Their results also show higher wear rates in alumina in the order of $6.76x10^{-5}$ – $1.66x10^{-4}$ mm^3/Nm while the wear rates of alumina/ mullite composites were in the order of $4.6x10^{-5}$ – $1.3x10^{-4}$ mm^3/Nm indicating a decreased friction coefficient due to the presence of mullite in the material.

Aluminium-mullite composites are commonly regarded as MMCs (Metal Matrix Composites). These composites were particularly reported [54] to offer advantages of reduction in mass, enhanced stiffness and strength, high corrosion resistance and improved wear resistance. Disadvantages noted were poor tensile ductility and low fracture toughness. Zhang H. et al [54] demonstrated structure and interface properties of nano-crystallihne aluminium/mullite composites through the use of sub-micrometer-sized nanocrystalline mullite (reinforcing phase) and aluminium particles. In this work atomic diffusion was concluded to play a significant role in aluminium wetting the mullite particles. The nanocrystalline aluminium and mullite powders used were synthesized by high-energy ball milling and samples were produced by hot isostatic pressing (HIP). No significant change of the grain size and density was observed in the nano-composite samples when the processing pressure was increased from 1.0 – 1.5GPa. Processing

temperature and composition of the samples had an overall effect on the final composite density. The increase in volume fraction of mullite contributed to a decrease in the final density that being attributed to weak interfacial bonding or some porosity developing on the mullite-aluminium interface. The chemistry of the interface between the aluminium matrix and mullite particles was neither mullite nor alumina but rather Al, O and Si distributed linearly over the interface [54].

2.3.3 SiC-Mullite Composites

SiC whiskers have been incorporated into numerous ceramic matrices in an attempt to improve their mechanical properties, in particular their resistance to catastrophic failure. This was done with inherent detrimental effect on the densification processes and potential health problems to the lungs if whisker diameter is less than 1 micron [7]. Rezaie H.R. et al [7] carried out a comparative study on mullite and SiC platelets-mullite composites using mullite derived from kaolinite mixed with α-alumina, and form sol-gel processing of boehmite and colloidal silica precursors. Fracture toughness and hardness was demonstrated to increase with SiC content, thus from 2.9±0.1 $MPa \cdot m^{1/2}$ for the monolith to 3.9±0.1 $MPa \cdot m^{1/2}$ for the 20vol% SiC composite. Their results are as shown in figure 7. Applied pressure during hot pressing had a more significant effect on improving density in mullite with SiC platelets additions. A maximum density of 97.5% of theoretical density was achieved after 1.5h at 1650^{o}C with 15 MPa pressure.

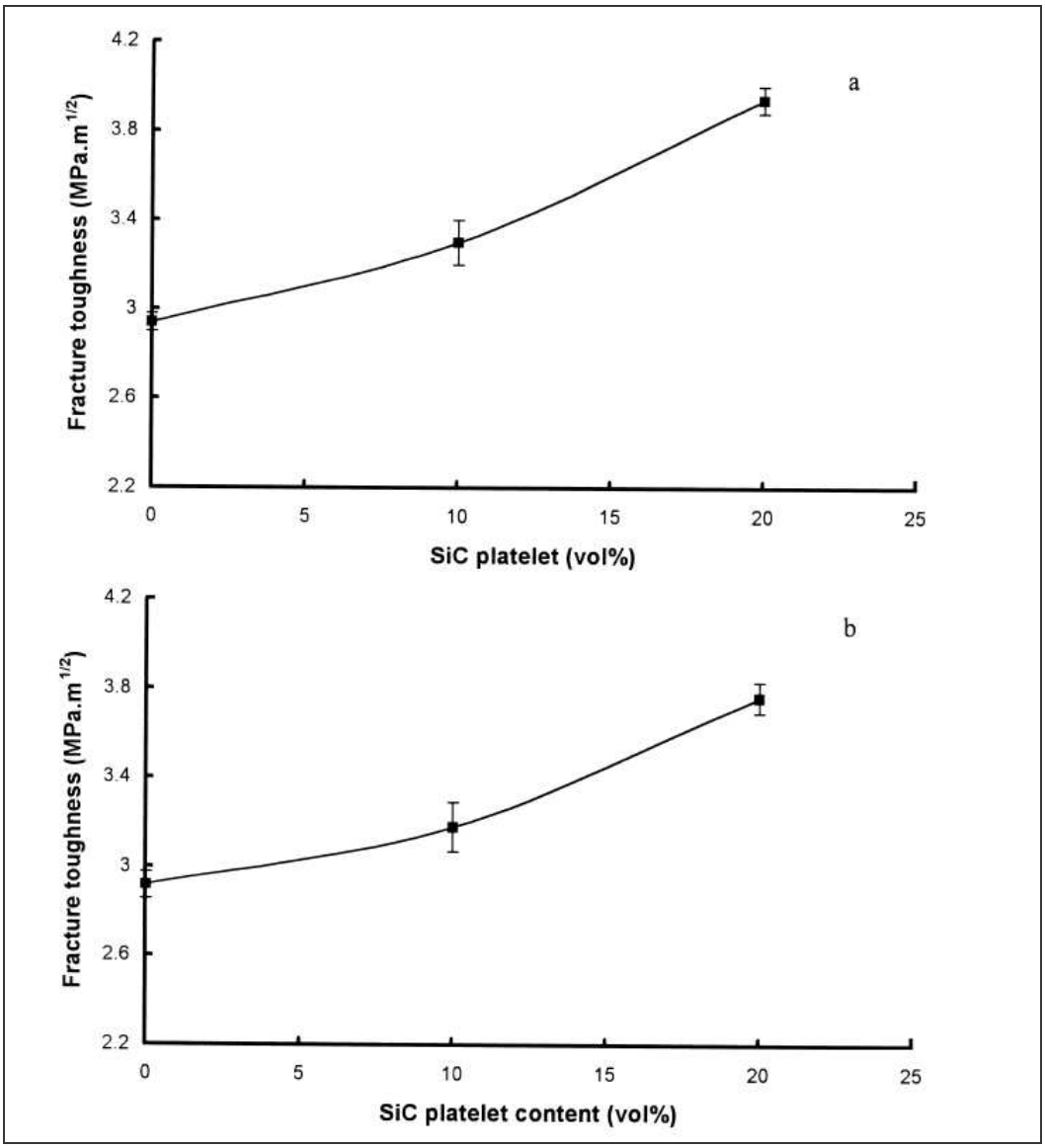


Figure 7: K_{IC} of mullite/SiC composites as a function of SiC content: (a) mullite derived from sol-gel powder and hot pressed at 1650°C for 1.5h under 15 MPa pressure; (b) mullite derived from kaolinite/α-alumina and hot pressed at 1600°C for 1.5h under 15MPa pressure [7].

2.3.4 Diamond-Mullite Composites

This section forms the main core of this work. Mechanical, chemical and structural properties of the diamond-mullite composites produced in this work will be compared to

the similar composites containing mullite in the previous sections. It is thus important to examine in detail the other component of such composite, that being diamond.

2.3.4.1 Synthetic Diamonds

Diamond is a strong covalently bonded material, unstable at high temperatures under ambient pressure [55]. The first synthetic diamonds were produced by Balzar von Platen in 1953. Since then improvements has been made, and nowadays bigger diamonds with good quality can be produced.

Diamonds can be produced from graphite under high pressure and temperature, in the presence of a catalytic metal. (Synthetic diamonds have metals enclosed, which might be detected with a polarization microscope).

2.3.4.2 Polycrystalline Diamond, Manufacture and Industrial Purposes

Polycrystalline diamond is tougher than single crystalline diamond because of the random orientation of the crystallites making up the material (no significant cleavage). Both poly- and single crystalline diamond have a high hardness. Thus, natural and synthesized polycrystalline diamond composite materials are useful in cutting tools, wire-drawing dies and rock-drilling bits. Particularly in rock-drilling applications, high hardness and high toughness materials are required [55]. As reported from [45] today diamonds are the most important abrasive in the industry. 90% of all produced diamonds (both natural and synthetic) are used for industrial purpose[45]. Such polycrystalline diamond for industrial

applications has been produced by means of high-pressure sintering techniques using diamond powders. The sintering of the powders is done using additives such as iron, nickel and cobalt which can act a catalyst for diamond formation, but also as the liquid phase sintering additive.

The use of industrial diamonds includes fragments of diamond crystals in glass cutting instrument, and fine diamond powder in polishing of for example precious stones.

Diamonds are also used in drill heads and in cutting instruments for stones or other hard materials [45]. Some kind of diamond such as framesite, carbonado and ballas are available for cutting tools and rock drilling bits, but the amount of these materials is limited [55].

2.3.4.3 Properties and degradation of Diamond

The density of diamond is 3.52 g/cm^3 and the hardness is 10 (in Mohs hardness scale). That is the highest of all known materials. Despite its hardness diamond is very brittle and impact sensitive. Diamond has the highest heat conductivity of all known materials. Therefore diamonds in drill heads do not get heated although high amounts of heat are generated by friction during the drilling operation. [45].

As quoted in work by Zhensong Tong, et al [8], when temperatures are in the range 700 – 1400^{o}C (in vacuum), surface graphitization of diamond particles takes place. When the temperature is higher than 1800^{o}C, bulk graphitization of diamond occurs. Thermal degradation of diamond can proceed mainly by two mechanisms: allotropic reconversion of metastable ***sp3*** structure into the thermodynamically more stable ***sp2*** structure or into

amorphous or graphite or fullerene structures. Whereas the transition of pure diamond to graphite in inert atmosphere usually begins at temperatures above 1500^{o}C, the presence of reactive external agents such as impurities, defects and particularly the presence of oxygen, may lead to the formation of a gray/ black coating on the surface of diamond at temperatures starting from 650^{o}C, depending on pressure, oxygen concentration and exposed crystallographic diamond faces. Hydrogen however has been reported to retard the thermal degradation of diamond [8].

2.3.4.4 Structure of Diamond

The crystal structure shows that each carbon atom is bonded to four others at a constant distance, so that the crystal structure is build up from tetrahedrons. The hardness in this structure comes from the strong forces between the atoms and the directionality of the C – C bonds. The hardness varies with crystallographic directions of the exposed facet.

This is the reason why diamond can be polished with diamond powder. The powder is applied to a plate. Because of the random orientation in the powder there will always be particles with the "hardest orientation" against the diamond that is to be polished [45]

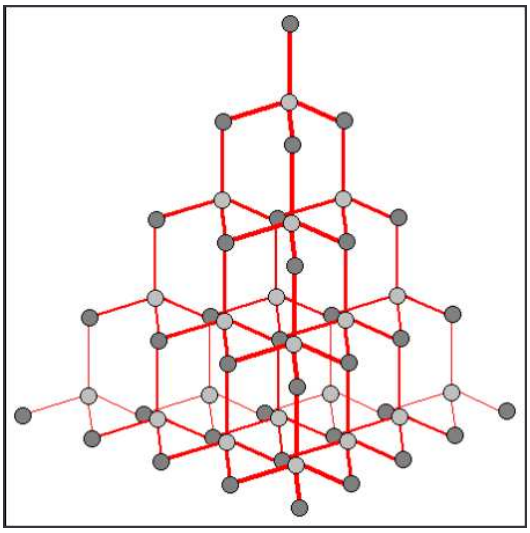


Figure 8: Structure of diamond [56]

The crystal structure of diamond is equivalent to a face-centred cubic (**FCC**) lattice, with a basis of two identical carbon atoms: one at (0, 0, 0) and the other at (1/4, 1/4, 1/4), where the coordinates are given as fractions along the cube sides. This is the same as two interpenetrating **FCC** lattices, offset from one another along a body diagonal by one-quarter of its length. The conventional unit cell is cubic, with a side length a_0 approximately equal to 3.567 Å (0.3567 nm) at room temperature [57].

2.3.4.5 Carbon Phase Diagram [9]

The pressure-temperature phase diagram for elemental carbon has been studied thoroughly over a period of many years, probably because of the economic and technological importance of two well-known allotropic forms of carbon, namely, graphite and diamond. Reports over the last several decades suggest that carbon may exist in many solid forms, including amorphous, various graphitic and carbynes (polyacetylenic-type

structures), diamond-like, and crystalline diamond. There is also evidence for the existence of two liquid phases of carbon, one metallic and the other nonmetallic [58].

The general features of the diagram, figure 9, which is considered to be the most probable for elemental carbon as of March 1988, show stability fields for graphite (hexagonal, space group $P6_3/mmc$), diamond (cubic, space group $Fd3m$), and liquid phases, with the associated triple point. Metastable extensions of the diamond-liquid and graphite-liquid phase boundaries are included as dashed lines. Three regions, A, B and C, have been specified in the diagram to identify *P-T* parameters where spontaneous direct phase transformations occur in the carbon system without catalyst-solvent assistance [58]. Region A denotes the area where a slow martensitic transition from hexagonal graphite to hexagonal diamond occurs. Region B involves a fast graphite-to-diamond transformation, and region C is where a fast diamond-to-graphite transition occurs. The diamond phase occupies a rather large region of the diagram. The experimentally-determined phase boundaries delineating the solid-liquid stability fields (liquidus) are not well defined because of difficulty in measuring the pressure and temperature parameters under the extreme conditions needed for producing these polymorphic changes in carbon. Laser-melting experiments in a diamond-anvil cell (DAC) were carried out to determine the liquidus curve [59]. In those experiments, temperatures in the 5000-6000^{o}K (4727-5727^{o}C) region were reported to be accurate to about 300^{o}K (27^{o}C) and results indicated roughly that the melting point of diamond increases somewhat with pressure [59]. Recent shock compression experiments have provided some indication of the melting temperature of diamond at higher pressures [60, 61]. Results of those experiments showed that the diamond form of carbon existed in the range of 80 GPa, 1500^{o}K

(1227°C) to 140 GPa, 5500°K (5227°C). Extrapolating to 150 GPa the melting point of diamond very probably must be in the 6000°K (5727°C) regime.

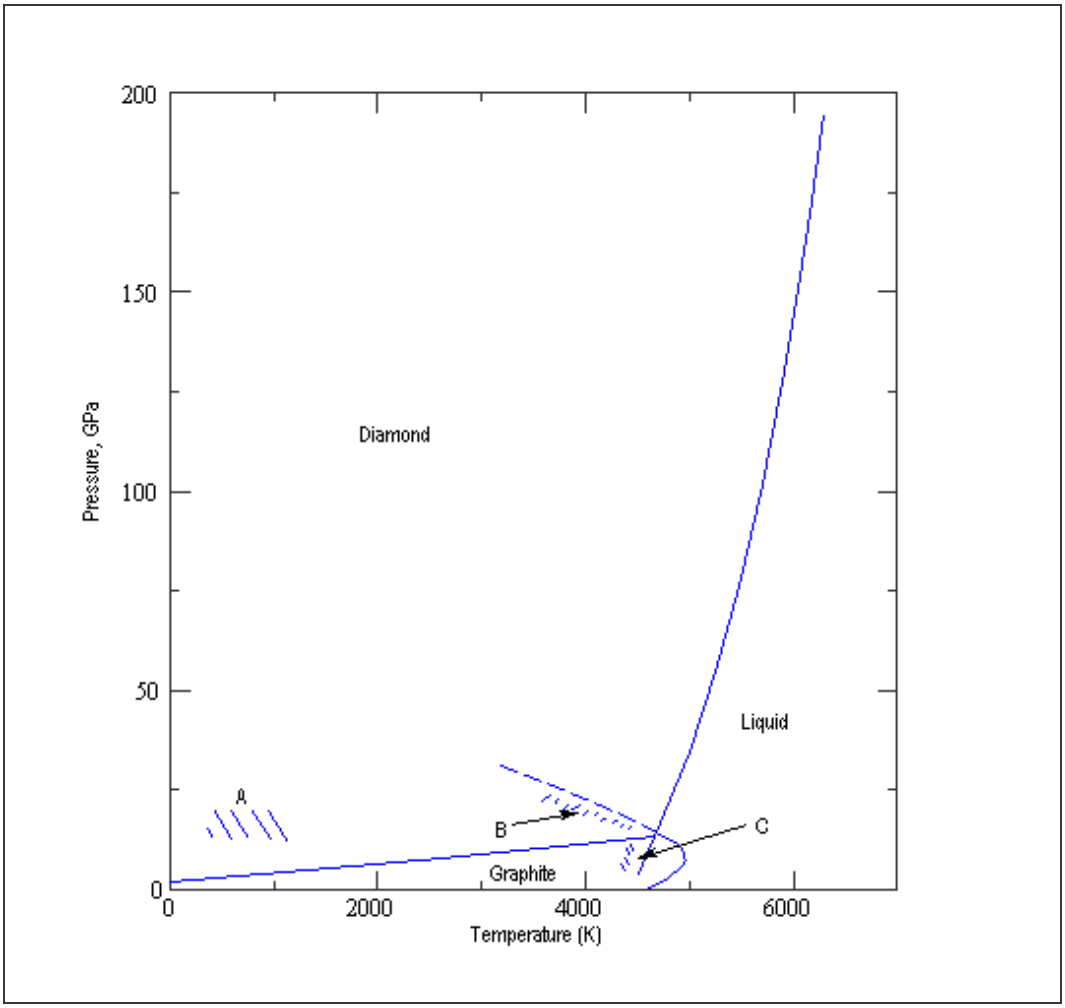


Figure 9: The *P-T* equilibrium phase diagram for C; A, B and C specify regions of metastability for the phase undergoing spontaneous transformation. [62]

The graphite-diamond and the graphite-liquid phase boundaries have been studied intensively and are much more firmly established than the melting curve for diamond [63]. In the low-temperature regime *{T < 1500°K (1227°C)}* the boundary is determined from experimental thermodynamic data for graphite and diamond. For example, the *P-T* point *{4.8 GPa, 1500°K (1227°C)}* has been calculated using thermodynamic data which

is in reasonable agreement with the experimentally-determined diamond-graphite equilibrium line, but there is still room for greater accuracy [63, 64]. For intermediate temperatures *{1500-3000^{o}K (1227-2727^{o}C)}*, the boundary line has been determined from direct conversion using transition-metal catalysts. Uncatalyzed conversion experiments were carried out at temperatures above 3000 K.

The graphite-liquid phase boundary has been studied to a lesser degree, but the general consensus is that there is a maximum in the liquidus at about 4800-5000^{o}K (4527-4727^{o}C) in the 5-6 GPa region indicating that liquid carbon is more dense than graphite at the higher pressures [63]. Electrical resistance measurements over the entire pressure range of the liquidus suggest that the liquid has metallic properties [63]. The graphite-diamond-liquid triple point was put at 10-12GPa and 4000^{o}K (3727^{o}C) in earlier work, [63] but the present diagram shows the point at somewhat higher temperatures with 4500-5000^{o}K (4227-4727^{o}C) as the most probable range.

In general, experimental data at pressures greater than 20GPa are somewhat uncertain; and considerable reasoning and, perhaps, intuition has been exercised to produce phase equilibria information in this part of the phase diagram for elemental carbon.

Chapter 3: Experimental Techniques

3.1 Chemicals

Table 5 below list all the powders and chemicals used in this work.

Table 5: Chemicals used in the research work

Chemical	**Supplier, Purity**	**As Received Particle Size, µm**
α-Al_2O_3	Sumitomo Chemical Co. Ltd (Japan), Type AKP 50 99.99%	D_{50} = 10.5
SiO_2	ACE (SA),	D_{50} = 9.62
Diamond	Element Six, (SA)	2.00
Tetra-ethylorthosilicate	Alfa Aesar (USA), 99.91%	-
Aluminium Secondary Butoxide	Alfa Aesar (USA), 95.0%	-
Water	Distilled, deionised	-
Argon	Afrox (SA), UHP	-

3.2 Attrition Milling

The as received alumina and silica were weighed in stoichiometric composition for 3:2 mullite ($3Al_2O_3$•$2SiO_2$) and mechanically mixed. The mixture was placed in a Szervari

Attritor System (Union Process, Ohio, US) for the attrition milling of the powders. The attritor system was equipped with an alumina shaft (stirrer) and the powder mixture was placed in an alumina container. The stirrer speed was set at 400rpm during milling of all powder mixtures. 2mm alumina balls were used as the milling media in weight ratios of 10:4:1 with respect to alumina balls, water and material to be milled. On attaining approximately a 2μm particle size (after 3.5hours milling time) the media was separated from the slurry mixture using a sieve of size 37μm and the slurry was placed in an oven set at 100^{o}C for 24 hours to drive off the water. The dried powder was then crushed and passed over a sieve of size 37μm. 2.5 – 5.0g of the powder mixture was cold uniaxialy – pressed at 30MPa to final disc samples of diameter of 18mm. The green densities of the cold uni-axially pressed samples were measured and reported.

3.3 Sample Preparation, Heat Treatment and Composite Nomenclature

The scope of this work explored two methods of synthesizing diamond/ mullite composites. The first method which involved the synthesis of mullite through hot press sintering (to produce sinter mullites) of the milled mixture of alumina and silica in their appropriate stoichiometric ratio will be the only method to be reported and discussed further in this work as it was successfully concluded. After successfully concluding the first method, 10 wt% diamond was introduced into the process in order to obtain diamond/ mullite composite samples. The second attempted method involved synthesizing the mullite from alumino and silicon alkoxides thus employing the sol/ gel process. (See appendix A for detailed calculations on reagent mixing). The overall aim after successfully concluding the method was to introduce 10 wt% diamond into the

process mixtures in order to obtain the diamond/ mullite composite samples. This method was not successfully concluded hence is not extensively reported and discussed in this dissertaion. For the purposes of future references for further development of this method the basis and concepts behind this approach will be reported in the following subsections.

3.3.1 The Sinter Mullites Method

The objective was to first observe if mullite is formed under the hot pressing condition; thus the milled alumina/ silica mixture produced disc samples were first sintered without addition of diamond. The samples were hot pressed (Thermal Technology Industries, USA), figure 10, sintered at 1400^{o}C, 1450^{o}C and 1500^{o}C in an argon atmosphere and labeled *MR1/1400/Ar, MR1/1450/Ar, MR1/1500/Ar* respectively. As from the Al_2O_3 – SiO_2 phase diagram in figure 3, full mullitization occurs at 1600^{o}C. Under this consideration a sample was also sintered using the milled alumina/ silica mixture at this temperature (1600^{o}C) to investigate the extent of mullitization under the given conditions and materials. The compact disc sample was labeled *MR1/1600/Ar*. The following heating profile was used (including sample sintered in the Muffle Furnace) in sintering of all the composites:

Ambient to 1400^{o}C at 40^{o}C/min and dwell at 1400^{o}C for 10 minutes,

(to allow for sintering load application during the 10 minutes)

from 1400^{o}C to maximum sintering temperature at 40^{o}C/min

and dwell at maximum sintering temperature for 60 minutes,

and lastly furnace natural cool to ambient temperature.

The sintering time at the maximum sintering temperature for all the composite samples was one hour. The sample sintering in air was done to investigate if mullite was formed from the two powders in their mixture following the alumina/ silica phase diagram.

For the synthesis of 10 wt% diamond/ mullite composite after successfully concluding the above work, 40g of the milled stoichiometric mullite powder mixture of particle size D_{50} = 2.1μm was weighed into a beaker followed by 100ml of acetone. 10 wt % diamond was then added to the mixture and the mixture was mechanically stirred for about 10minutes after which it was placed in an ultrasonic bath for 20 minutes to enhance a homogenous diamond dispersion within the mixture. This was also done to try and break any suspected agglomeration within the mixture. The slurry mixture was dried and 2.5 – 5.0g of the powder mixture was cold uni-pressed at 30MPa to a final disc sample of diameter 18mm. The green densities of the cold uni-axially pressed samples were measured. The sample discs were then sintered at temperature of 1400^{o}C, 1450^{o}C and 1500^{o}C in a hot uni-axial press (Thermal Technology Industries, USA) under an argon atmosphere and pressure of 70MPa at the sintering temperature. The samples were then labeled *MRD1/1400/Ar, MRD1/1450/Ar and MRD1/1500/Ar* respectively to the sintering temperatures. All the samples were subjected to a dwell time of 1 hour at each of the maximum sintering temperature. Figure 11 (section 3.4) below illustrates the configuration under which the sample was sintered in the hot press.



Figure 10: Hot Press [65]

3.3.2 The Sol/ Gel Preparation Method

This attempted method is only reported in this work as basis and reference for any future work to synthesize diamond/ mullite composites through the sol/gel processing route. Stoichiometric calculations in appendix A were used in the preparation of the mullite samples. Larger sample masses were prepared from stoichiometric ratios of the quantities required. The procedure followed in this method was according to patented work by Yoldas Bulent E. et al [36].

In this work, 20ml of tetraethylorthosilicate was placed in conical flask. 115ml of ethanol was also added to the conical flask with about 4ml of water for partial hydrolysis. The mixture was covered with aluminium foil and left for about 15 minutes to stand at room

temperature. 74.4ml of aluminium secondary Butoxide was added to the mixture in the conical flask. The mixture was briefly shaken and placed in an oven preset at 60^{o}C for 24 hours. 50ml of the resulting solution was measured and 50ml of ethanol and 50ml of distilled water were added to form a thick white precipitate in the process. The mixture was covered with an aluminium foil and shaken in order to homogenise in the solution. The mixture was then placed in an oven preset at 100^{o}C and left to dry.

The powder was ground and passed through a 37μm size sieve. 2.5 – 5g of the powder mixture was taken and cold uniaxialy – pressed at 30MPa to a final sample discs with a diameter of 18mm. The discs were placed and sintered in a muffle furnace (Elite Technologies, USA) in air and the following sintering profile was used:

Ambient to maximum sintering temperature (1000, 1200, 1400 and 1600^{o}C) at 10^{o}C/min,

dwell at maximum sintering temperature for 60 minutes,

furnace natural cool to ambient temperature.

The sintered disc samples were then characterized to determine phase composition. The results were used to decide whether to add diamond in order to produce a diamond mullite composite. The Different compacts were sintered to final temperatures 1000, 1200, 1400 and 1600^{o}C and were then labeled *SG1000_A, SG1200_A, SG1400_A* and *SG1600_A*. The following method was followed to synthesize diamond/ mullite composites thus after successfully concluding the first stage above with an aimed result of crystalline mullite.

Method: 40g of the powder that was produced from the sol/ gel preparation above would be weighed and placed in a beaker with 100ml acetone. 10 wt% 2μm particle size diamond powder was placed in the same beaker and the mixture stirred for about 10minutes before placing in an ultrasonic bath for about 20minutes in order to achieve homogenous diamond particle dispersion. The mixture was placed in an oven preset at 100 deg centigrade till dry. The resulting powder mixture was then ground and passed through a 37μm sieve. 2.5 – 5g of the sieved powder mixture would then be taken and cold uniaxialy – pressed at 30MPa to a final sample discs with a diameter of 18mm. The discs were placed and sintered in a hot press (Thermal Technology Industries, USA), figure 10, under an argon atmosphere and pressure of 50MPa at the maximum sintering temperature of 1000^{o}C. Figure 11 (section 3.4) below illustrates the configuration under which the sample was to be sintered in the hot press. The following sintering profile was observed:

Ambient to 800^{o}C at 10^{o}C/min, and dwell at 800^{o}C for 10 minutes,

(to allow for sintering load application during the 10 minutes),

from 800^{o}C to maximum sintering temperature (1000^{o}C) at 10^{o}C/min,

dwell at 1000^{o}C for 60 minutes,

furnace natural cool to ambient temperature.

3.4 Hot Press Sample Preparation

The cold uniaxialy pressed sample disc was placed in a graphite pot previous coated with an h-BN suspension stabilised with poly – vinyl pyrrolidone. An h-BN suspension coated graphite piston was then placed inside the pot over the sample inside, see configuration in figure 11 below. The same configuration was placed in a graphite die, in between a lower and upper punch. In this case the upper punch is screwed on the upper part of the hot press furnace. The die and punch set was also coated with an h-BN suspension stabilised with poly – vinyl pyrrolidone. The coating was done to avoid carbon contamination during sintering as well as enhance easy sample removal from the die after the hot pressing process.

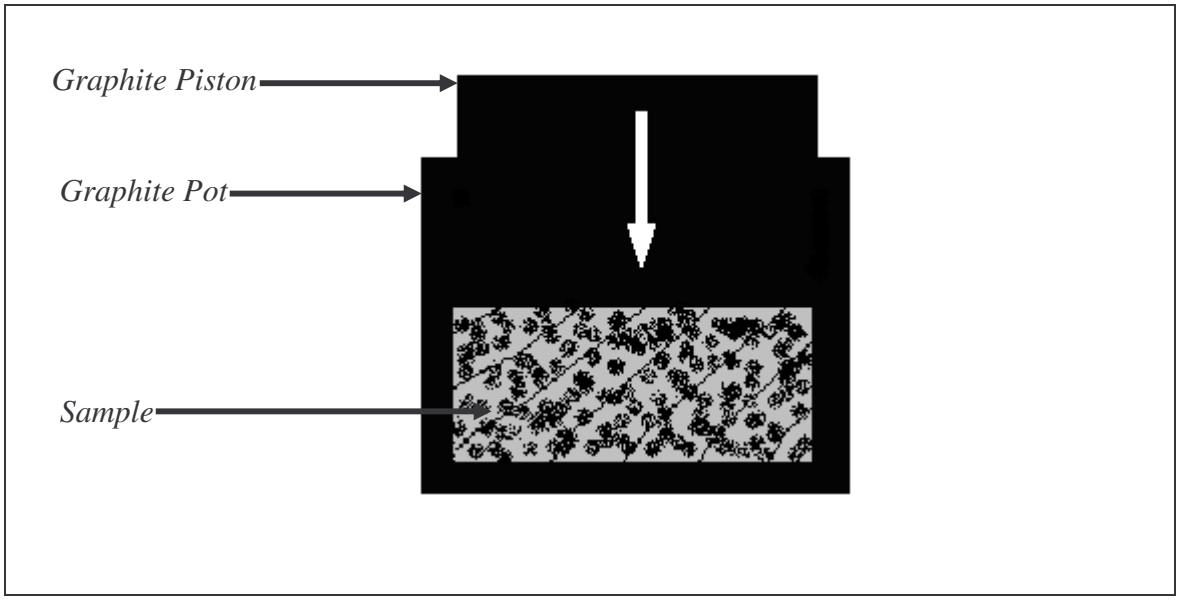


Figure 11: Graphite pot and piston configuration

3.5 Particle Size Analysis

Particle size analysis after each milling interval was carried out using a Malvern Mastersizer Hydro 2000MU (Malvern Instruments, UK). The suspension of the attrition milled sample was added to water, which was used as the dispersant with no surfactants added during each measurement. 3 minute ultrasonic displacement was initiated before each measurement was carried out.

3.6 Density and Porosity

Archimedes' method for density determination was used on all the disc samples for both density and porosity measurements. The samples were first boiled in distilled water for 5hours prior to weighing them. The suspended weight, M_s (See appendix B, table 16) of each sample was measured five times together with the wet weight, M_w, (See appendix B, table 16) obtained after wiping off water from the surface of the sample. The average of each determination was then computed. The samples were then dried for 30mins at 120^{o}C and the dry weight, M_d, (See appendix B, table 16) of the samples was obtained.

3.7 X-Ray Diffraction

Phase composition was determined using an X-ray diffraction (XRD) machine with type Phillips PW 1710 generator operating at 40 kV and 20 mA. Radiation of CuKα1 was used. Each powder sample was run from 10° to 80° 2θ with a step size of 0.02° 2θ and step time of 1 second.

3.8 Scanning Electron Microscopy / Energy Dispersive Spectroscopy

Morphological examination of the diamond containing compact samples was done using a model Philips – XL30 Series emission Scanning Electron Microscope – SEM (Element Six, SA). Elemental analysis of the samples was done using Energy Dispensive Spectroscopy (EDS). The alumina and silica powders attritor milled in stoichiometric composition for 3:2 mullite were analyzed under SEM and the images obtained were labeled *MR1 powder*. An overall EDS for the image was done to investigate the elemental composition. Images and EDS of the initial diamond containing powders were also taken and labeled *MRD1 powder*.

3.9 Sample Cutting and Mounting

The 18mm sample discs were cut using a Struers Sectom – 10 (Struers, SA) cutting machine to two semi-discs and one was mounted under Bakelite using a LECO PR – 25, Model 814 – 300 (LECO Corporation, USA) mounting machine with the transverse section on the outer part of the resulting Bakelite solid.

3.10 Sample Surface Grinding and Polishing

The mounted transverse section was then rough and fine ground over a series of silicon carbide grinding paper (220 – 1200 grit size) using a LECO Spectrum System2000 polisher (LECO Africa, SA). The polishing was done in four stages; the first stage was done using an MD-LARGO polishing cloth and a 9μm diamond particle suspension

(Struers, SA) applied periodically together with an extender (lubricant). The second stage was done using an MD-DAC (Struers, SA) polishing cloth with periodic application of a 3μm diamond particle suspension together with an extender. The third stage was done using an MD-NAP (Struers, SA) polishing cloth with periodic application of a 1μm diamond particle suspension together with an extender. The fourth and final polishing stage was done using an MD-CHEM (Struers, SA) polishing cloth with application of 0.04μm OPS suspension and extender (Struers, SA). After each polishing stage the mounted samples were cleaned in an Ultrasonic Cleaner model SB-120DT for 10 minutes.

3.11 Etching

Cut surfaces for diamond containing compact samples, *MRD1/1400/Ar, MRD1/1450/Ar and MRD1/1500/Ar*, were etched using 10% HF [66] for 3 minutes in order to reveal the microstructure of the compacts. The samples were then washed with running water and dried before imaging. Other cut sample surfaces were mounted as described in section 3.10. The mounted and polished samples were not etched and these were used in hardness determination, section 3.13. SEM imaging of the un-etched surfaces of the three compacts was also done to observe the extent of the etchant effects.

3.12 Raman Spectroscopy

Raman spectroscopy was done at the Physics department (University of the Witwatersrand, SA). Random spots on the cut surface of a diamond-mullite composite mounted in resin (Bakelite) were measured with micro-Raman spectroscopy using the 514.5nm line of an argon ion laser. The laser spot size was ~1.5micron in diameter. The Raman measurements were done with the micro-Raman attachment of a Jobin-Yvon T64000 Raman spectrometer operated in single spectrograph mode.

3.12 Hardness and Fracture Toughness

A Vickers LECO V-100-A2 (LECO Corporation, USA) hardness machine was used in the determination of hardness and fracture toughness of the mounted and polished sample. A load of 10kgf was applied on the sample. The dimensions of the indentations were measured together with the crack length at each apex. The Vickers number was then calculated using equation (i) below using the average diagonal of each indent. The fracture toughness was calculated from the Shetty equation, equation (ii):

$$\mathbf{H_v = 1.85437 \cdot P/d^2} \qquad \textbf{(i)}$$

$$\mathbf{K_{IC} = 0.0889 \cdot \sqrt{(H_v \cdot P/4 \cdot \mathit{l})}} \qquad \textbf{(ii)}$$

Where: H_v is the Vickers number, MPa

P is the load applied, N

l is the average crack length, μm

d is the average diagonal, μm

As proposed by Shetty D.K., et al, [67] equation (ii) above must satisfy criterion $c/a > 1.3$ and $0.25 < l/a < 2.5$ for a reliable fracture toughness - measurement a, is the half-diagonal length of the indentation and the total crack length, $c = l + a$.

In other work by [51] fracture toughness was determined using the well known formula:

$$\mathbf{K_{IC} = 0.941 \cdot P c^{-3/2}\ (MPa \cdot m^{1/2})} \qquad \textbf{(iii)}$$

Where: P is the load applied, N

c is the crack length, m

Indentation fracture toughness was used because of the simplicity of the approach and its good applicability. However the technique has a number of drawbacks, namely the small volume of material sampled, errors in measuring the crack length, the uncertainty of whether cracks are radial or Palmqvist, the presence of lateral cracking and the potential for time dependent crack propagation on removal of the indenter [7]. Other methods to determine fracture toughness can thus be explored to further verify fracture toughness results. For the measurements presented in this work equation (ii) was used after satisfaction of the above criterion.

Chapter 4: Results

This chapter gives a summary of all the results of the investigations conducted by the sinter mullites method, with a brief discussion of the results obtained with less successful sol-gel technique. The first section gives an overview of all the results obtained from all the investigations undertaken in this work through the sinter mullites method. A brief analysis is given after each result is presented. A full discussion of all the results follows in the proceeding chapter 5. The results include: characterisation on all the powders used – this involved particle size analysis, XRD and SEM –, analysis of composites synthesised by the sinter mullites method and physical property investigations (hardness, fracture toughness). Raman spectroscopy results on composites were also presented particularly done to investigate the presence and state of diamond after hot press sintering of the composites at the various sintering temperatures.

4.1 Attrition Milling

In this section we present the result for the milling of the stoichiometric mixture of alumina-silica. Table 6 gives the particle size analysis of the as received materials. Table 7 then gives the particle size analysis of the attritor milled mixture of alumina and silica in 3:2 stoichiometric composition for mullite. Figure 12 gives the undersize particle size distribution of milled composition which was mixed with 2µm (Grade 2) diamond.

Table 6: As received particle size analysis

Raw Material		Alumina	Silica	Diamond
Particle Size Analysis	**D_{10}, µm**	0.13	1.41	0.75
	D_{50}, µm	10.5	9.62	1.91
	D_{90}, µm	34.7	35.3	3.78

Table 7: Milled Alumina-Silica Mixture (See section 3.2 for the milling conditions)

Mixture		Alumina and Silica in 3:2 molar ratio
Particle Size Analysis	**D_{10}, µm**	1.19
	D_{50}, µm	2.11
	D_{90}, µm	4.25

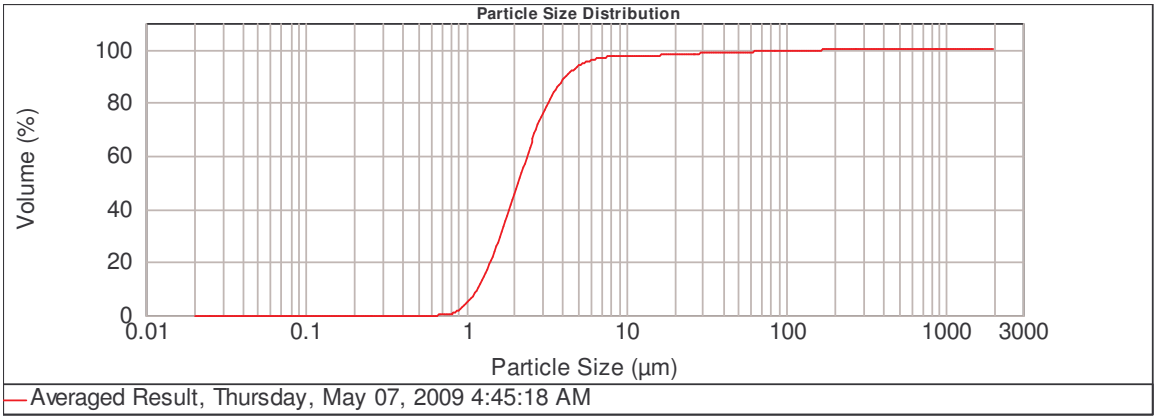


Figure 12: Average particle size analysis of alumina and silica mixture in 3:2 molar ratios.

After attrition milling for 3.5 hours of mixture of alumina and silica mixture in stoichiometric ratio for 3:2 mullite a D_{50} particle size of 2.11μm was achieved. Figure 12 shows the undersize particle size distribution of the milled mixture. This was then mixed with 10wt% Grade 2 diamond with a D_{50} particle size of 1.91μm as shown in table 6 above. This mixing was as described in section 3.3.

4.2 Overview of Results Obtained by Sinter Mullites Method

Table 8: Overview of result – sinter mullites method

Composite Identity	**MR1/1400/Ar**	**MRD1/1400/Ar**	**MR1/1450/Ar**	**MRD1/1450/Ar**	**MR1/1500/Ar**	**MRD1/1500/Ar**
Sintering Temperature (Atmosphere)	1400 (Ar)	1400 (Ar)	1450 (Ar)	1450 (Ar)	1500 (Ar)	1500 (Ar)
Approx Sintering Pressure, MPa	70	70	70	70	70	70
Composition	Al_2O_3/SiO_2 in 3:2 mullite molar ratio	Al_2O_3/SiO_2 in 3:2 mullite molar ratio + 10wt% Diamond	Al_2O_3/SiO_2 in 3:2 mullite molar ratio	Al_2O_3/SiO_2 in 3:2 mullite molar ratio + 10wt% Diamond	Al_2O_3/SiO_2 in 3:2 mullite molar ratio	Al_2O_3/SiO_2 in 3:2 mullite molar ratio + 10wt% Diamond
Theoretical Density, g/cm^3	3.45	3.46	3.45	3.46	3.45	3.46
Achieved Bulk Density, g/cm^3 (%)	3.25 (94.3)	3.24 (93.7)	3.28 (95.2)	3.27 (94.6)	3.33 (96.5)	3.31 (95.8)
Open Porosity, %	1.91	0.06	0.62	0.27	1.76	1.34
Closed Porosity, %	3.8	6.3	4.2	5.1	1.7	2.9
Average Hv (10kgf Load), GPa	13.2 ± 0.12	15.5 ± 0.33	12.7 ± 0.24	14.2± 0.43	12.2± 0.15	13.5 ± 0.27
Average K_{IC}, MPa•m$^{1/2}$	4.8 ± 0.10	-	4.4± 0.10	-	4.1± 0.09	-
Final Phases, Crystalline	Mullite, Cristobalite Corundum Quartz	Mullite Cristobalite Corundum Diamond	Mullite Cristobalite Corundum	Mullite Cristobalite Corundum Diamond	Mullite, Corundum, Cristobalite	Mullite, Corundum, Cristobalite, Diamond

Table 8 above shows an overview of the results obtained from compacts synthesized using the sinter mullites method. The hot pressing pressure was the same, 70MPa, for all the compacts. The same table 8 shows the various physical properties determined after each hot press cycle. These include density, hardness and fracture toughness. The final crystalline phases determined by x-ray diffraction for each compact are also tabulated for comparison purposes.

4.3 Analysis of Samples by the Sol/ Gel Method

4.3.1 X-Ray Diffraction – Sol/ Gel Method

As stated earlier work preliminary stages on the sol/ gel method was not successfully concluded. No crystalline phase of mullite was obtained after mixing all the reagents and sintering up over a range of trial temperatures 1000 – 1600^{o}C as can be observed in the X-ray traces of figure 13 below. It is imperative to point out the great potential the sol/gel method has in synthesising diamond/ mullite composite. Temperatures reported [36] to form mullite can be as low as < 1000^{o}C in an inert atmosphere compared to the sinter mullites route (1400 – 1600^{o}) which has adverse effects on the state of the final diamond form. Thus may lead to poor mechanical properties of the resulting compact. A decision was reached during execution of this work to pay particular attention to the synthesis of diamond/ mullite composites by the sinter mullites route only. Further developmental work on the sol/ gel process will be undertaken as another project to be embarked at a later stage at the University of the Witwatersrand, school of chemical and metallurgical engineering under the supervision of Prof. Iakovos Sigalas.

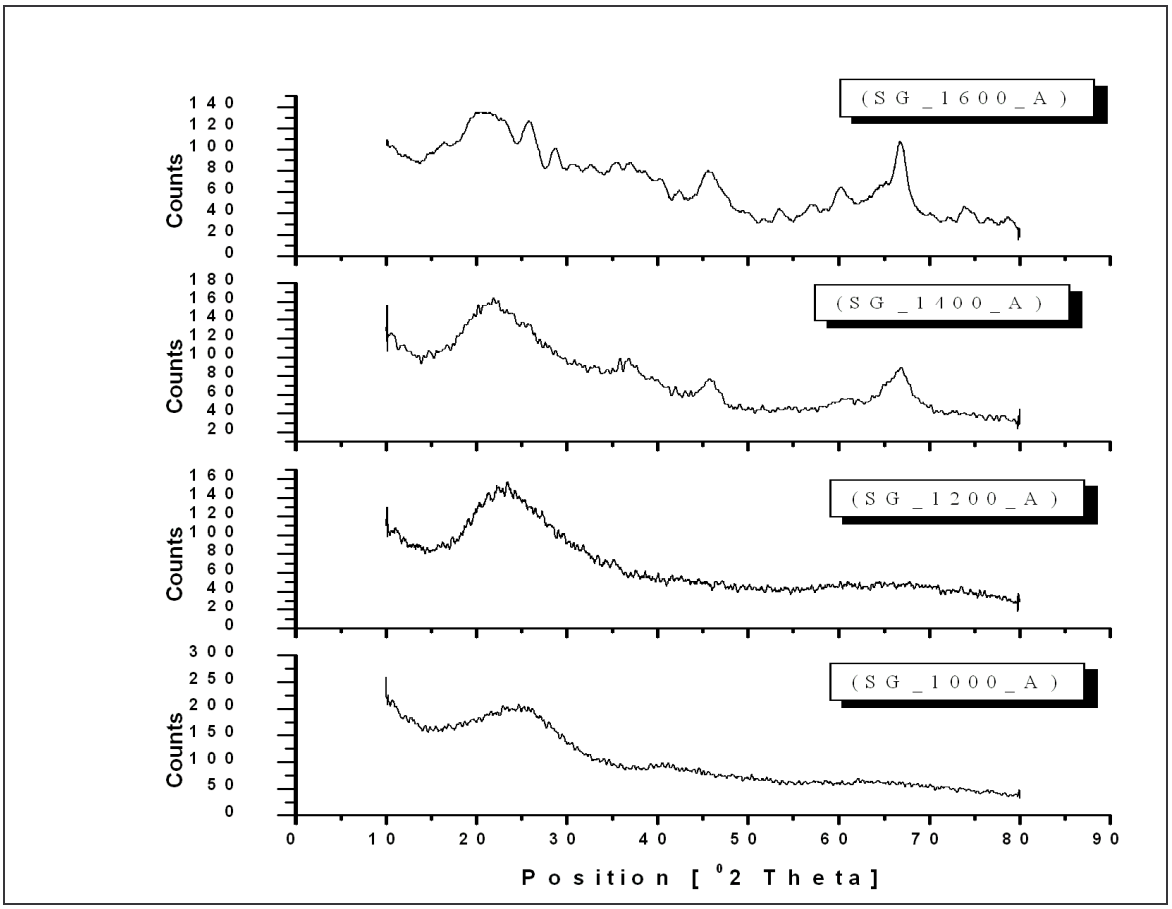


Figure 13: XRD results of samples by sol/gel process

Figure 13 shows XRD results obtained from first stage of the sol/ gel method of sintered samples *SG/1000/A, SG/1200/A, SG/1400/A* and *SG/1600/A* at temperatures 1000, 1200, 1400 and 1600^{o}C respectively. An amorphous phase was obtained from each sample. The sample sintered at 1600 produced some unidentified peaks. See appendix D, figures 45 – 48, of the same X-ray traces from where data was obtained to plot stacked traces of figure 13 for comparison purposes.

4.4 Analysis of Composites Produced by the Sinter Mullites Method

4.4.1 X-Ray Diffraction – Sinter Mullites Method

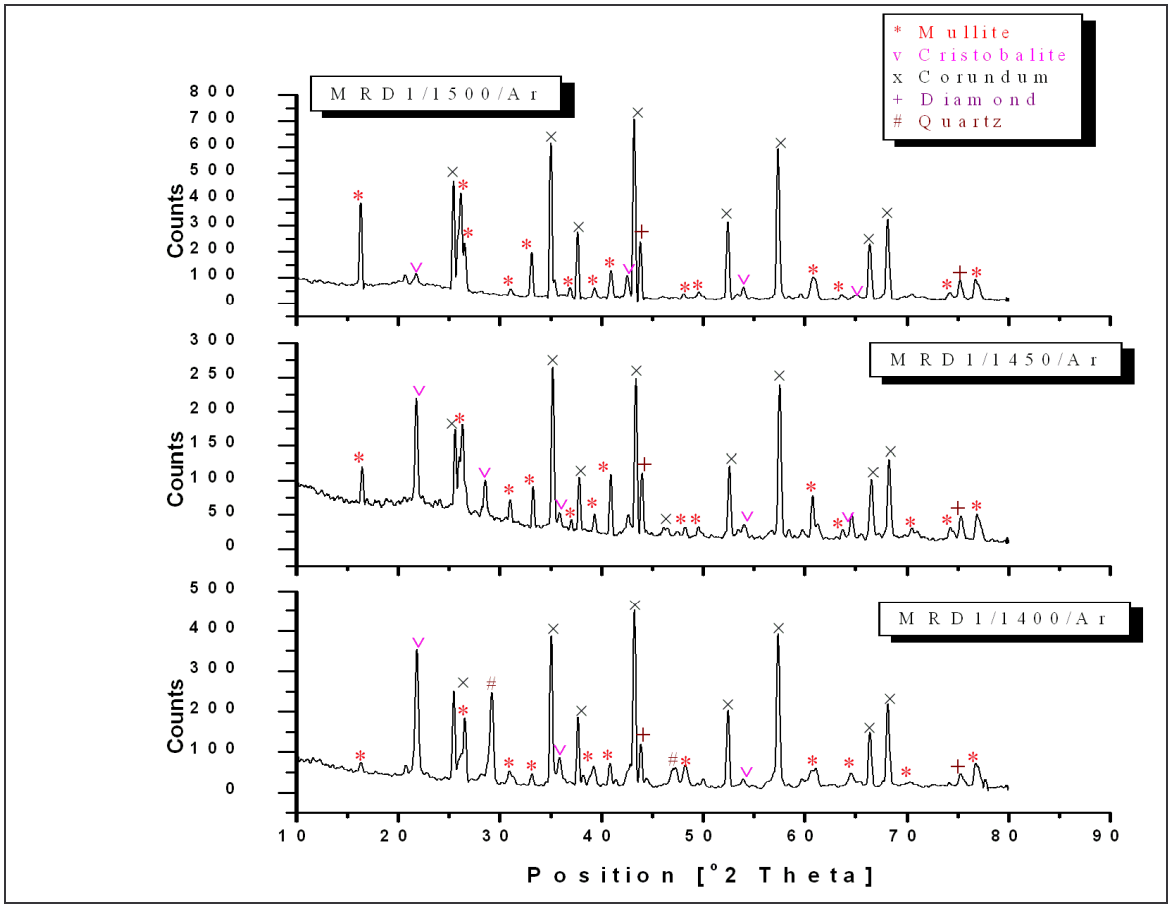


Figure 14: XRD of composite samples each with 10wt% diamond added and sintered at the various temperatures under investigation. Samples *MRD1/1400/Ar, MRD1/1450/Ar & MRD1/1500/Ar*

Figure 14 gives a comparison of the x-ray traces of diamond containing composites *MRD1/1400/Ar, MRD1/1450/Ar and MRD1/1500/Ar* produced by the sinter mullites method. See Appendix D for the complete reference codes and peak pattern lists. An increase in the intensity of mullite with a decrease in the amount of silica phase (cristobalite) was observed with increasing temperature. Sample *MRD1/1400/Ar* showed the presence of residual un-reacted quartz.

4.4.2 Scanning Electron Microscopy/ Energy Dispersive Spectroscopy

4.4.2.1 Scanning Electron Microscopy/ Energy Dispersive Spectroscopy of as Received Powders

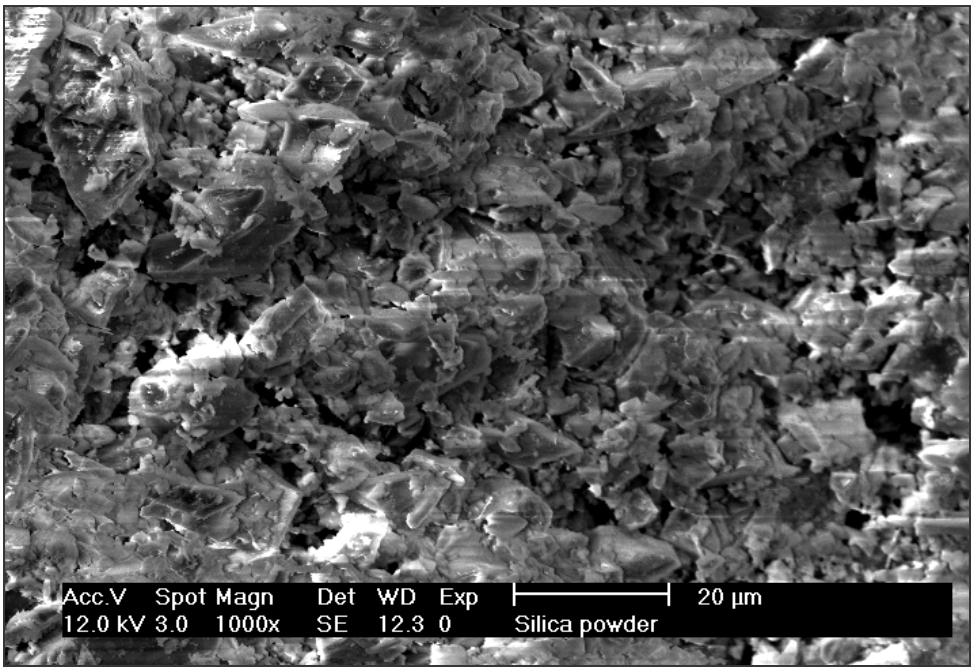


Figure 15: SEM micrograph of as received silica powder

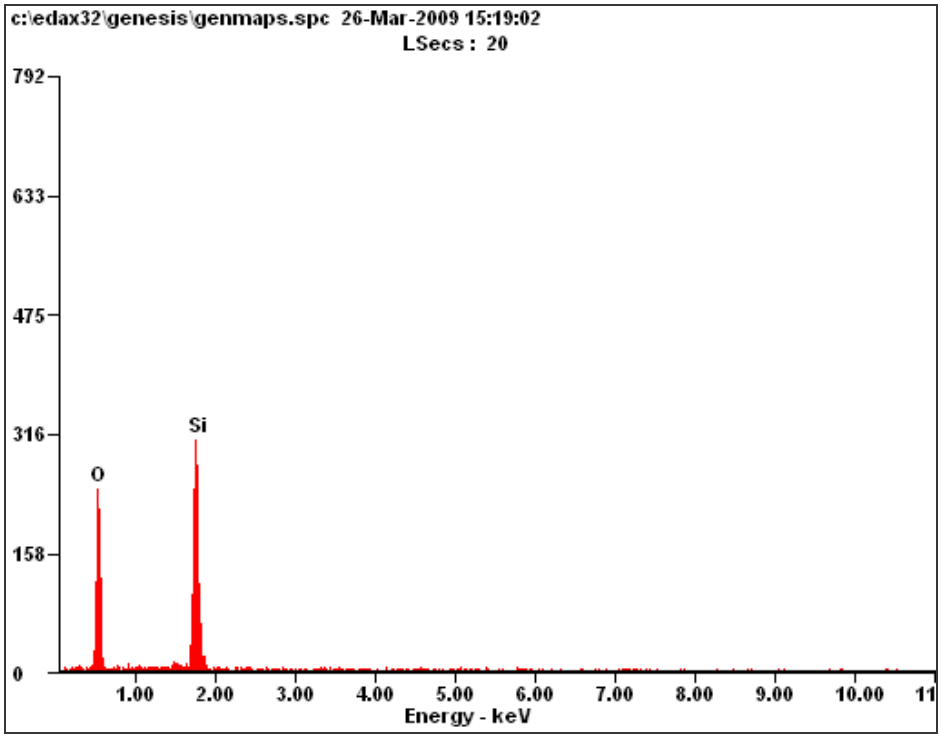


Figure 16: Overall EDS of as received Silica Powder

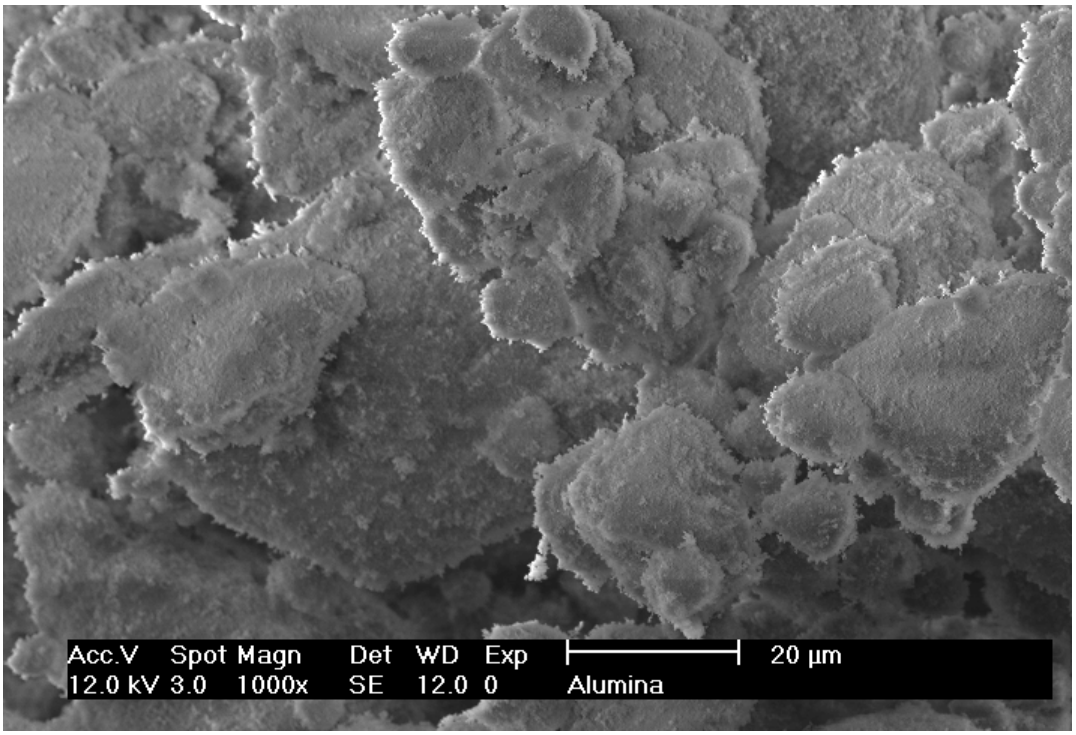


Figure 17: SEM micrograph of as received silica powder

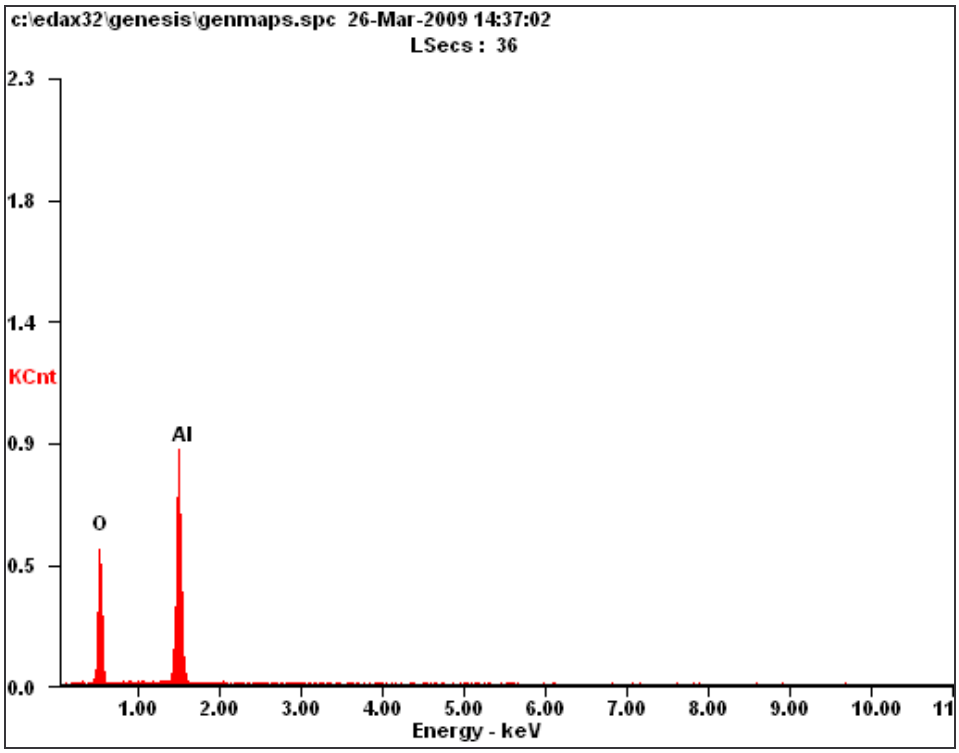


Figure 18: Overall EDS of as received alumina powder

4.4.2.2 Scanning Electron Microscopy/ Energy Dispersive Spectroscopy of the Raw Powder Mixtures

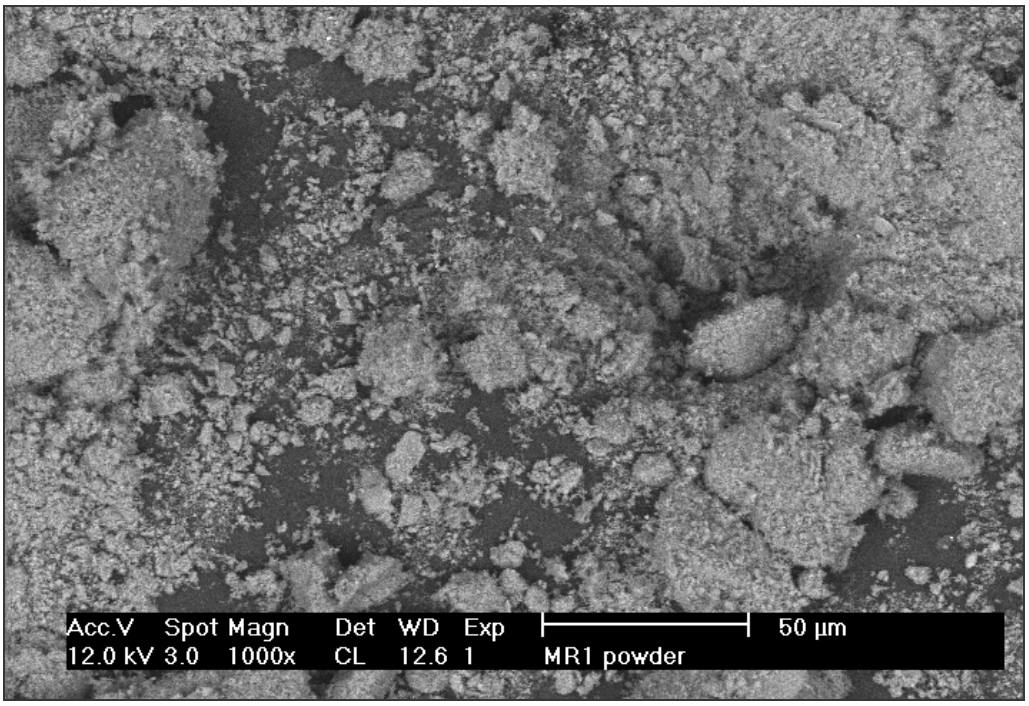


Figure 19: SEM micrograph of milled alumina and silica in 3:2 stoichiometric composition for mullite.

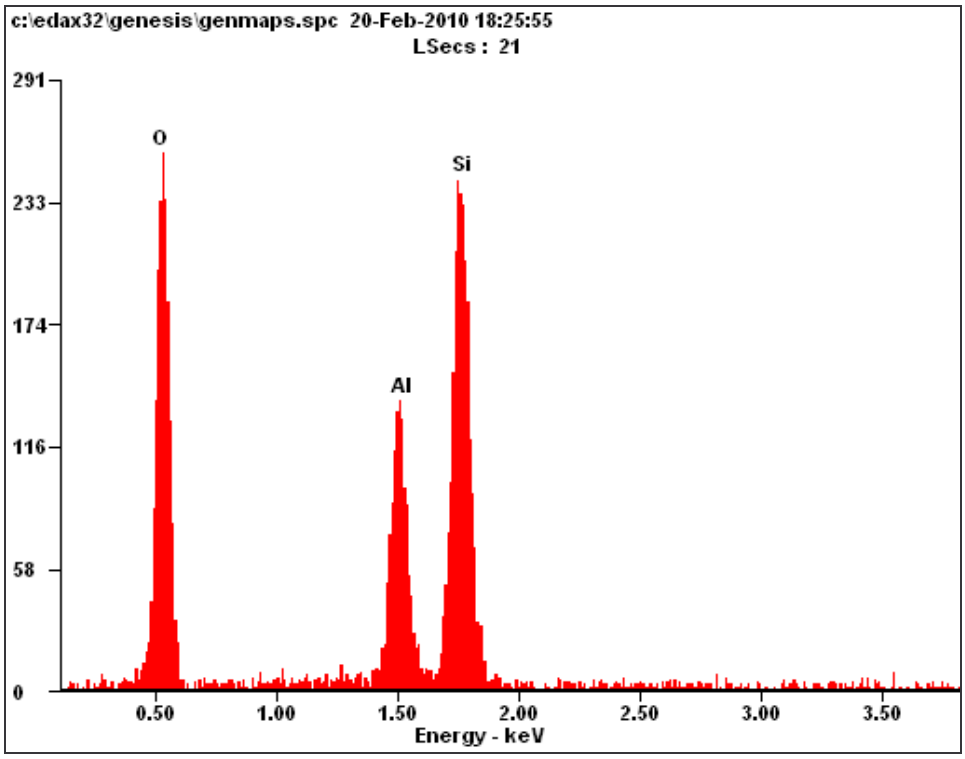


Figure 20: Overall EDS of milled alumina and silica in 3:2 stoichiometric composition for mullite

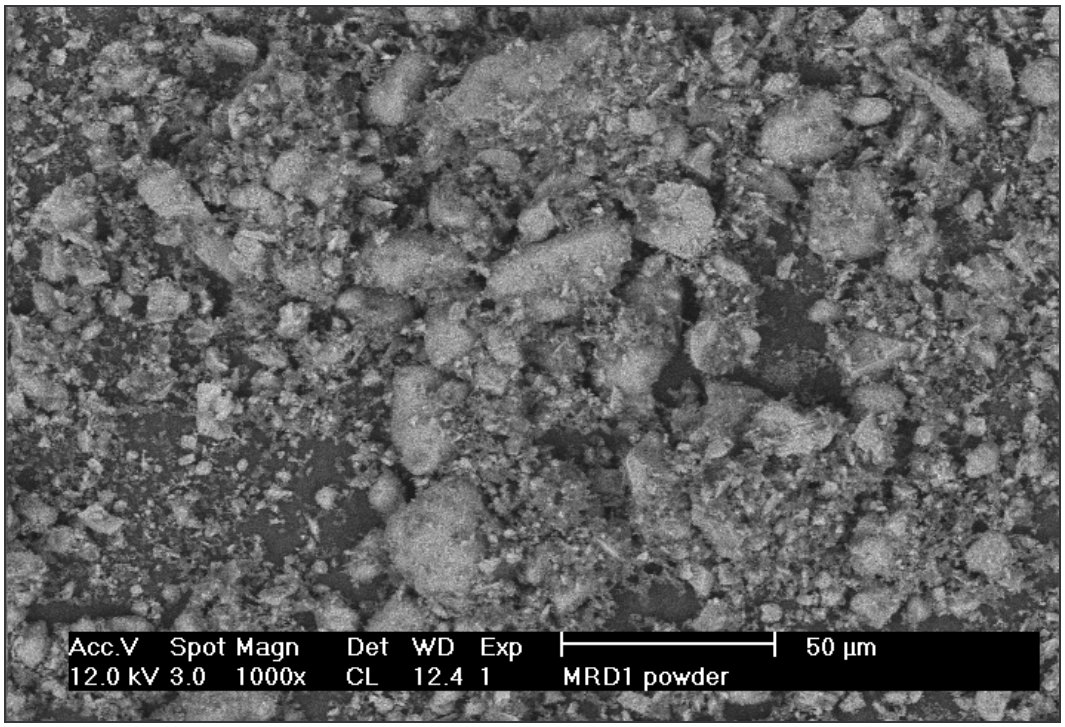


Figure 21: SEM micrograph of milled alumina and silica in 3:2 stoichiometric composition for mullite plus 10wt% diamond.

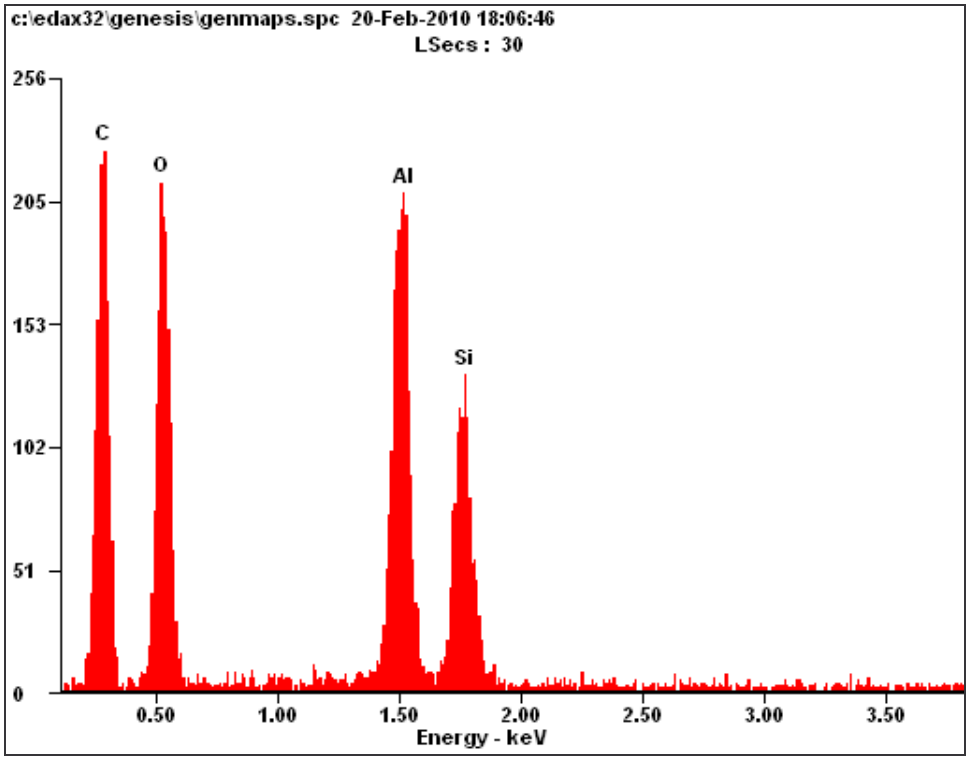


Figure 22: Overall EDS of milled alumina and silica in 3:2 stoichiometric composition for mullite plus 10wt% diamond.

Figures 17, 19 and 21 show SEM micrographs of the as received alumina, *MR1 powder* and *MRD1 powder* respectively. The carbon content of figure 22 for diamond was high due to additional carbon picked up by the equipment from the conductive carbon tape on to which the powders were spread for imaging and EDS during sample preparation.

4.4.2.3 Scanning Electron Microscopy/ Energy Dispersive Spectroscopy – 10 wt% Diamond Compact Samples

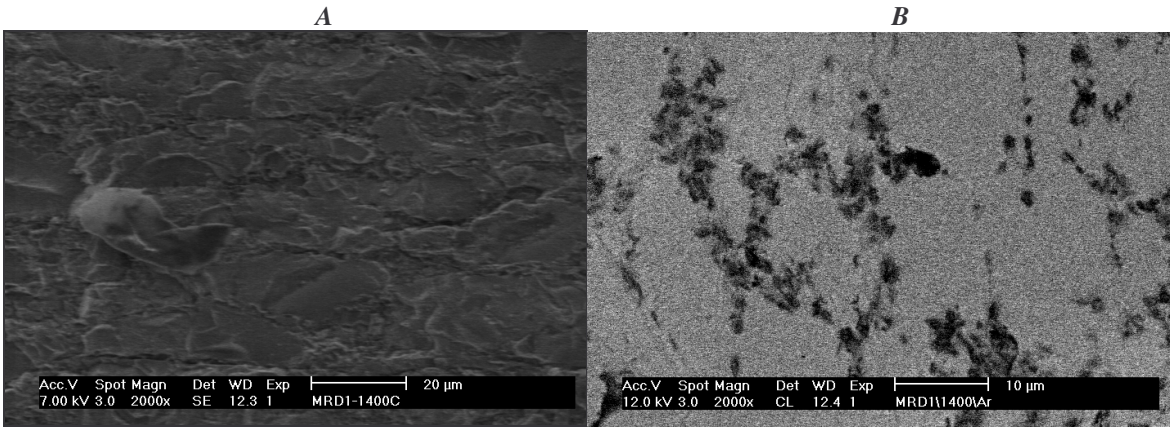


Figure 23: SEM micrographs of cut and etched (A) and un-etched (B) surfaces of compact sample *MRD1/1400/Ar*. See spot analysis of the etched surface in proceeding figures.

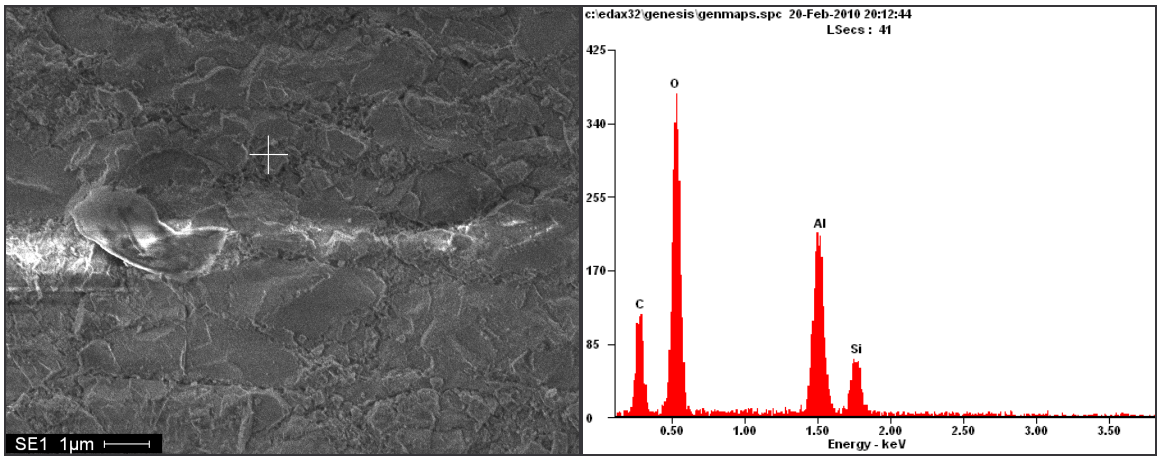


Figure 24: SEM micrograph (2k magnification) and spot EDS of sample *MRD1/1400/Ar*, etched surface.

Table 9: Elemental spot analysis of figure 21

Element	Wt%	At%
C	18.36	28.21
O	40.63	45.63
Al	31.62	20.23
Si	8.89	5.92

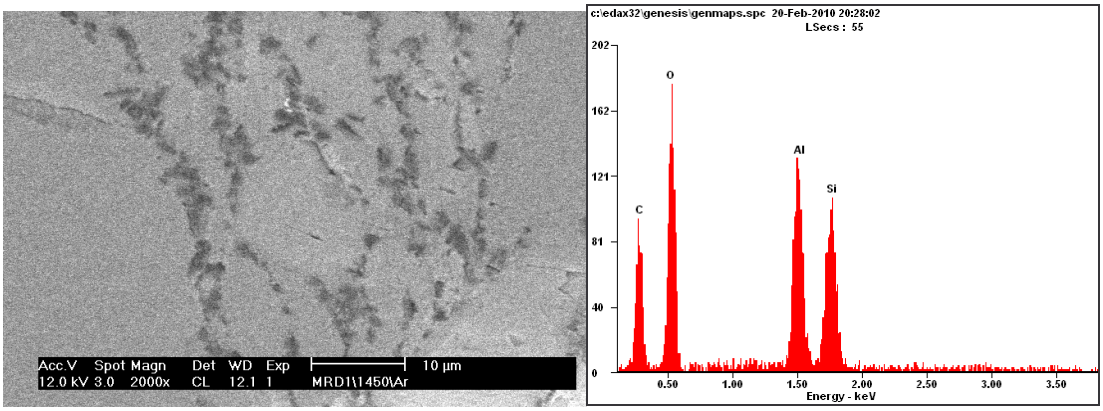


Figure 25: SEM micrograph and overall EDS of un-etched surface of compact sample *MRD1/1450/Ar*

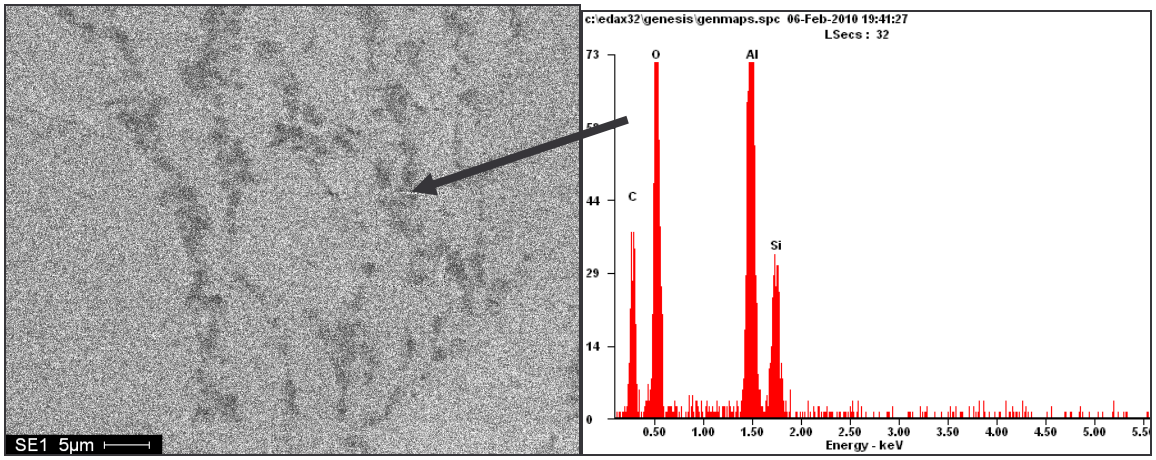


Figure 26: SEM micrograph (2k magnification) and spot EDS for the un-etched sample *MRD1/1450/Ar*

Table 10: Elemental spot analysis of figure 23

Element	Wt%	At%
C	36.56	49.26
O	31.36	31.72
Al	22.90	13.74
Si	7.73	4.28

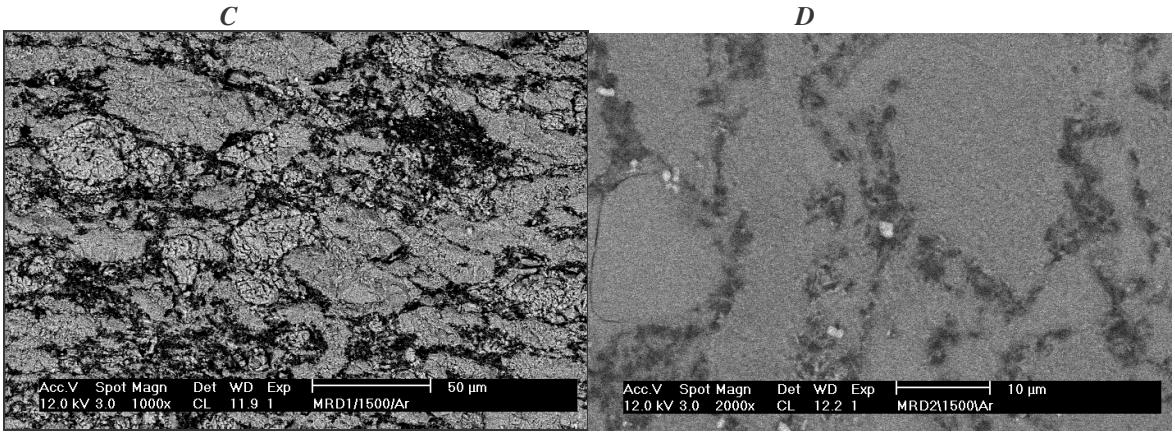


Figure 27: SEM micrographs of cut and etched (C) and un-etched (D) surfaces of compact sample *MRD1/1500/Ar*. See spot analysis of the etched surface in proceeding figures.

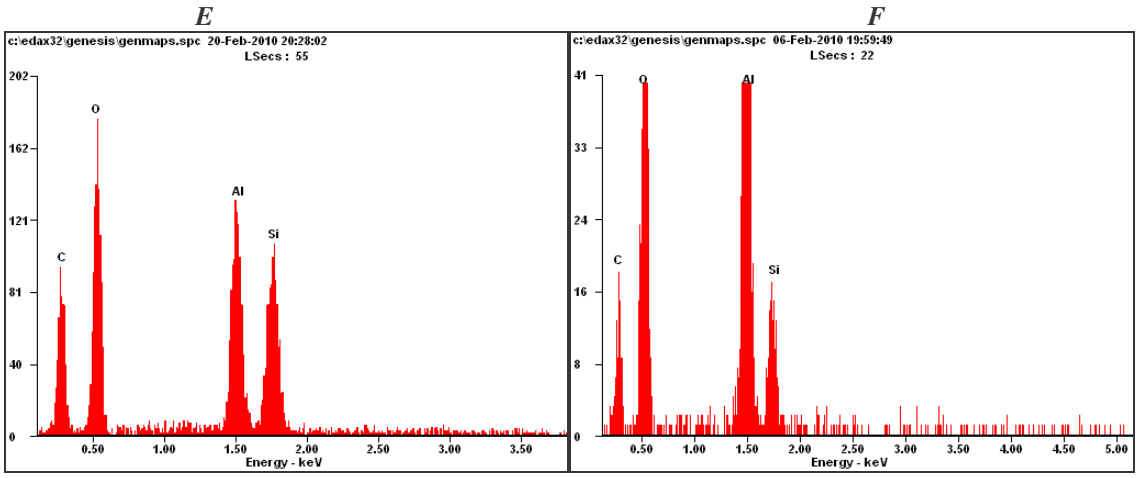


Figure 28: Overall EDS of etched (E) and un-etched (F) surfaces of compact sample *MRD1/1500/Ar.*

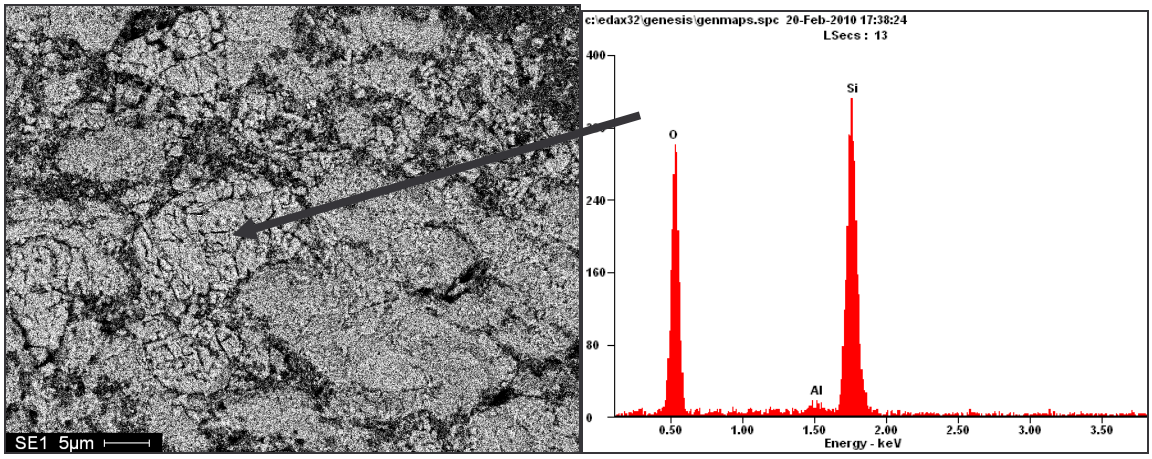


Figure 29: Spot analysis and EDS of etched compact sample *MRD1/1500/Ar* at 2k magnification

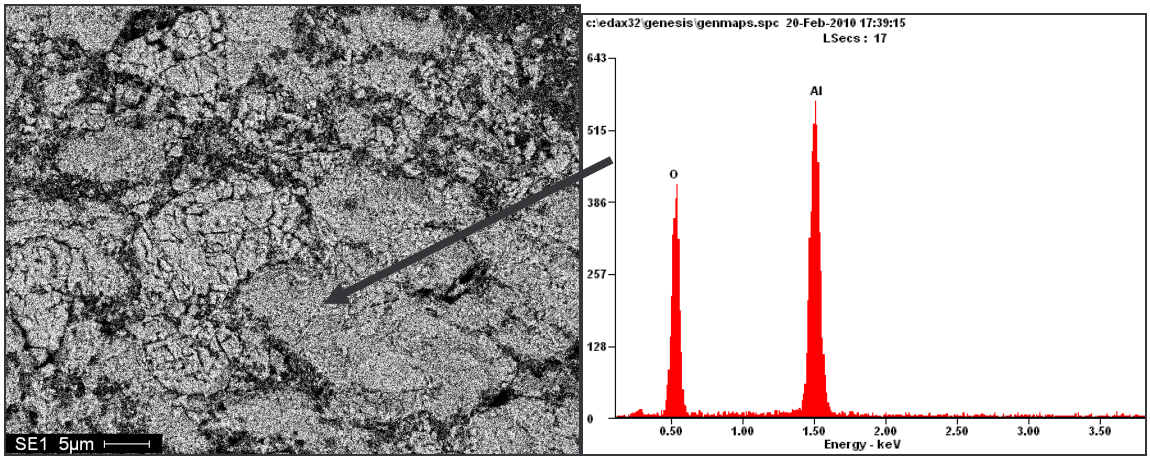


Figure 30: Spot analysis and EDS of etched compact sample *MRD1/1500/Ar* at 2k magnification

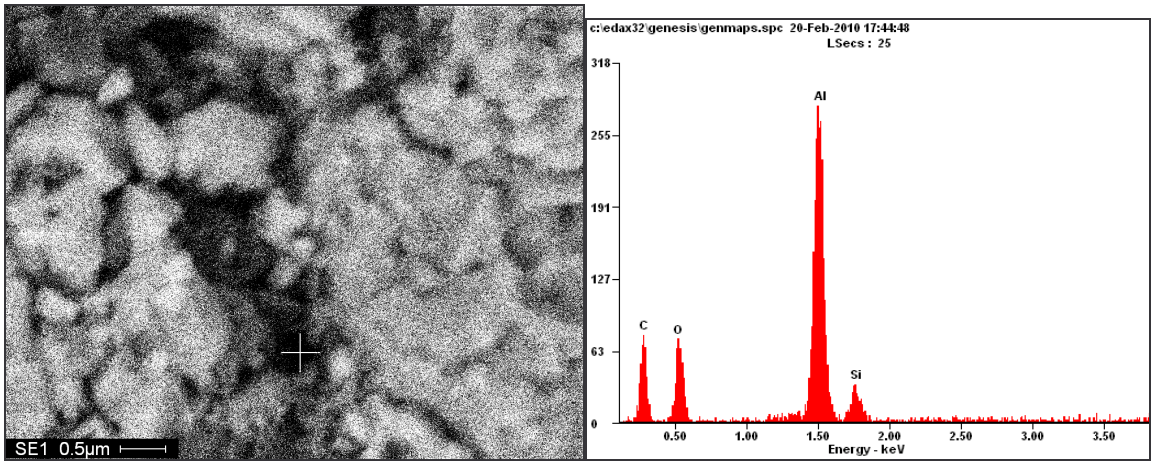


Figure 31: Spot analysis and EDS of etched compact sample *MRD1/1500/Ar*, the marked point shows is the grain boundary between alumina and silica phases at 20k magnification.

Table 11: Elemental spot analysis of figure 28

Element	Wt%	At%
C	42.66	58.31
O	16.59	17.02
Al	35.76	21.75
Si	4.99	2.92

4.4.3 Raman Spectroscopy

Figure 32 – 34 shows the analysis of Raman shift observed on random spots on the cut surface of the samples containing diamond (*MRD1/1400/Ar, MRD1/1450, and MRD1/1500/Ar*). For all three samples containing diamond *(MRD1/1400/Ar, MRD1/1450/Ar and MRD1/1500/Ar)* five random spots were analyzed on the cut face mounted in resin for each of the samples.

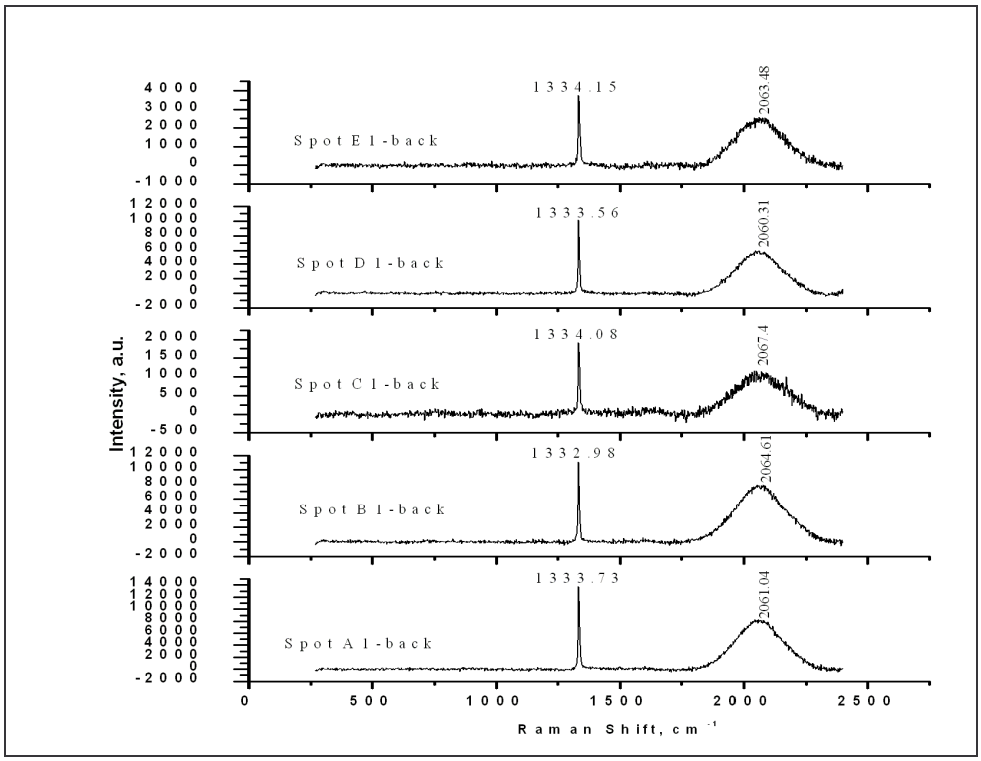


Figure 32: Raman Spectroscopy analysis for sample MRD1/1400/Ar.

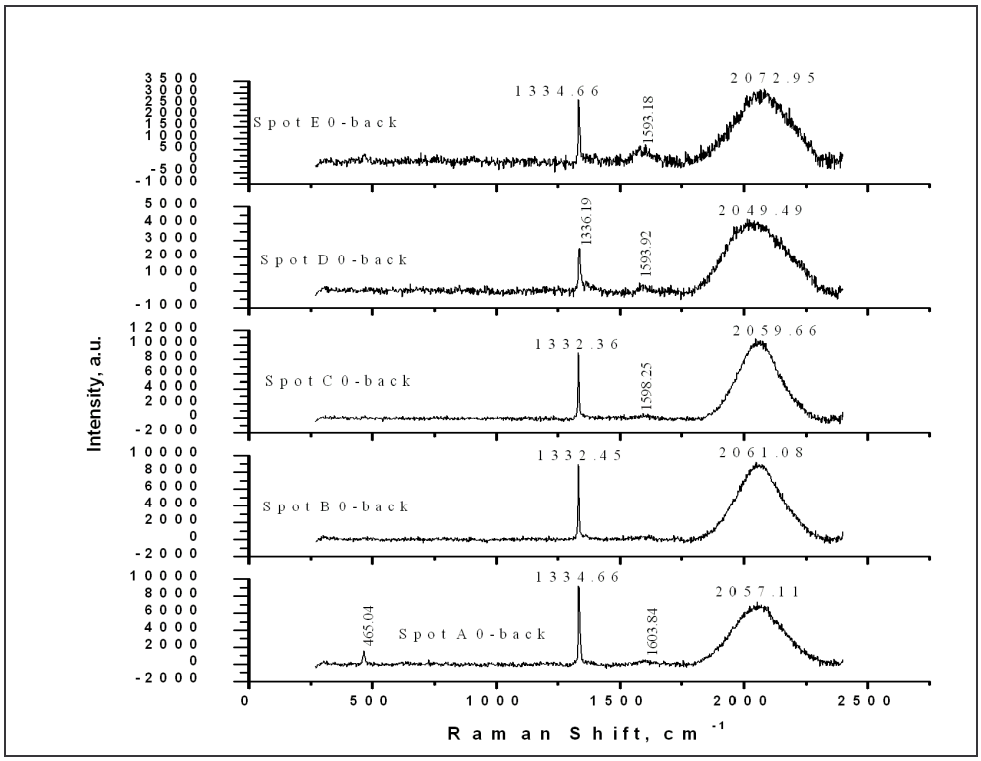


Figure 33: Raman Spectroscopy analysis for sample MRD1/1450/Ar.

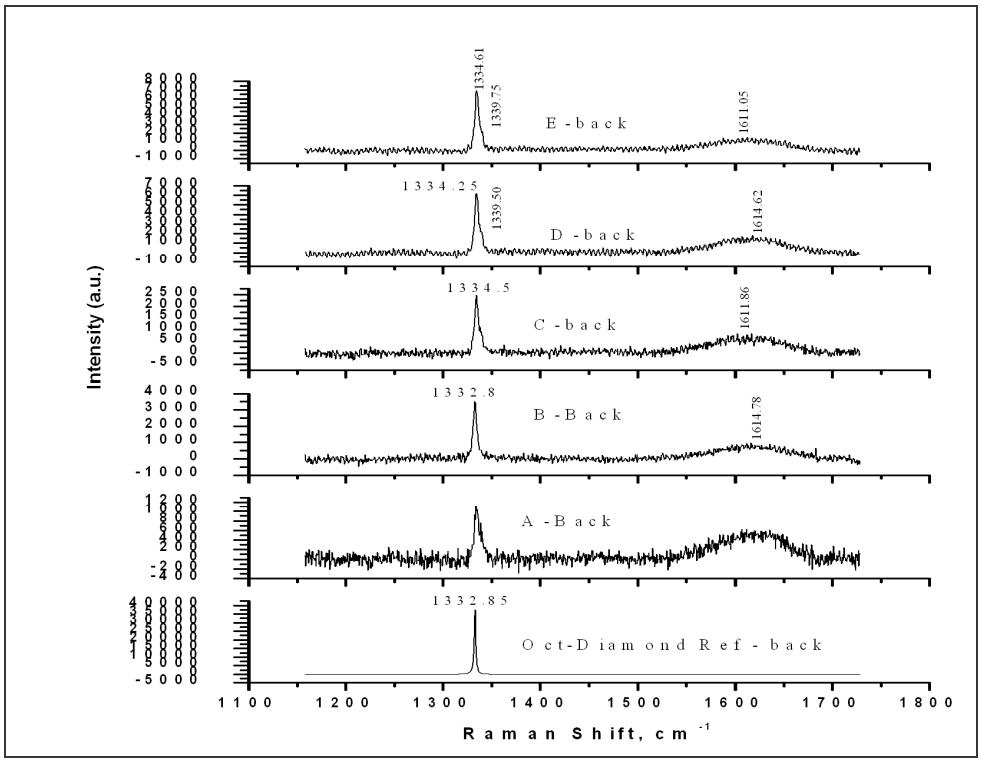


Figure 34: Raman Spectroscopy analysis for sample MRD1/1500/Ar.

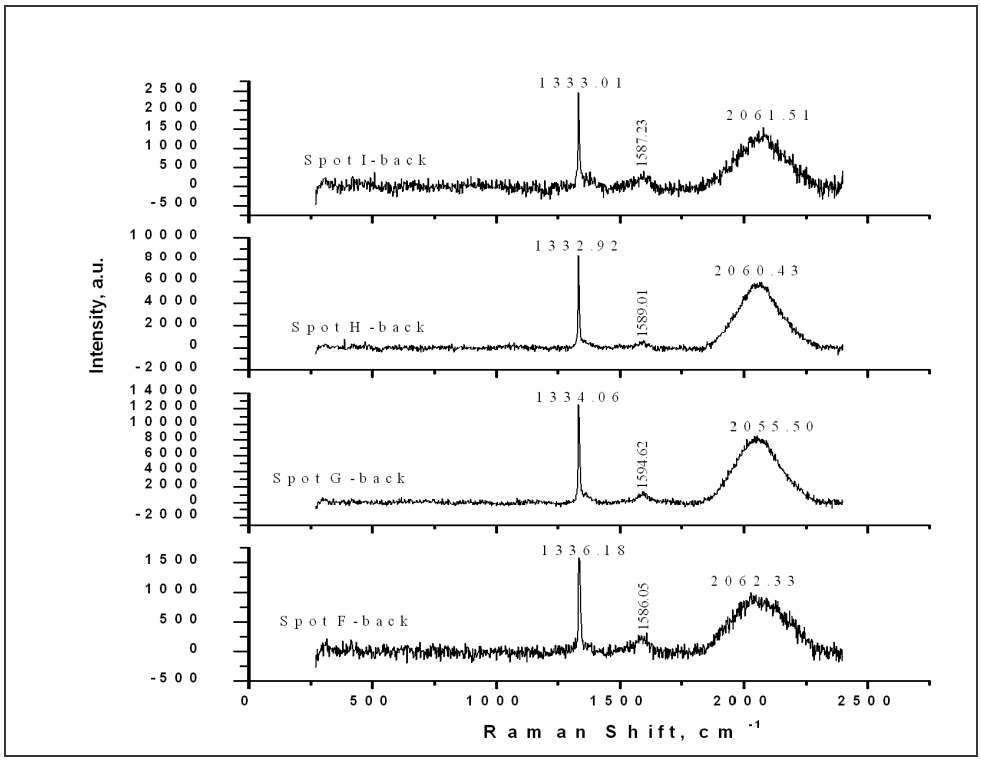


Figure 35: Raman Spectroscopy analysis for sample MRD1/1500/Ar – Second Examination using a different grating to the previous analysis (Figure 34 above) to give a larger spectral range, so that lower wavenumber peaks will also be visible if present.

All Raman Spectroscopy plots (figure 32 – 35) presented in this work had background subtracted. For all three samples containing diamond *(MRD1/1400/Ar, MRD1/1450/Ar and MRD1/1500/Ar)* several random spots were analyzed on the cut face mounted in resin. All spectra show the presence of the diamond Raman peak around 1332cm^{-1}. There is also a strong, broad peak present in all the spectra at around 2050cm^{-1}. This was most likely the zero phonon line from the luminescence due to the neutral nitrogen vacancy defect in the diamond. This defect forms in diamond where substitutional nitrogen is present as an impurity, and when there is vacancy formation and diffusion at high temperature. The other reason for this broad band could be the luminescence band of structural defects or

impurities in diamond, which reveals a lower quality of the silicon/ diamond buffer interface as also reported by Kromka A. et al [68].

4.4.4 Hardness & Fracture Toughness – Samples by Sinter Mullites Method

This subsection presents results from measurements obtained from the determination of hardness and fracture toughness by Vickers indentation. See appendix C for the complete results obtained in the determination of hardness and fracture toughness by Vickers indentation. Graphical plots of hardness and fracture toughness against temperature are also presented.

Table 12: Criterion satisfaction of equation (ii), section 3.13, for fracture toughness calculation after [67].

Sample	**Average values for each sample**			***c/a***	***l/a***
	a	***l***	***c***		
MR1/1400/Ar	58.7	113.6	172.3	2.94	1.94
MR1/1450/Ar	59.7	125.4	185.1	3.10	2.10
MR1/1500/Ar	60.95	139.5	200.45	3.29	2.29
For equation (ii), section 3.13, to hold criterion $c/a > 1.3$ and $0.25 < l/a < 2.5$ must be satisfied					

From table 9 above, equation (ii), section 3.13 criterion is satisfied thus can be used in the determination of fracture toughness [67].

Table 13: Hardness and fracture toughness results

Composite Identity	MR1/1400/Ar	MRD1/1400/Ar	MR1/1450/Ar	MRD1/1450/Ar	MR1/1500/Ar	MRD1/1500/Ar
Average Hv (10kgf Load), GPa	13.2 ± 0.12	15.5 ± 0.33	12.7 ± 0.24	14.2± 0.43	12.2± 0.15	13.5 ± 0.27
Average K_{IC}, $MPa \bullet m^{1/2}$ (Calculated using equation (ii))	4.75 ± 0.10	-	4.43± 0.10	-	4.13± 0.09	-

Fracture toughness results for compact samples *MRD1/1400/Ar, MRD1/1450/Ar* and *MRD1/1500/Ar* were not calculated as no visible fracture cracks were observed during Vickers indentation measurements. The diagonals for the indents could only be measured and were used in the determination of hardness. Figure 37 which show a graphical representation of the hardness and fracture toughness against temperature for both samples with 10 wt% diamond added and samples with no diamond added. Visible fracture cracks after indentation of samples *MR1/1400/Ar, MR1/1450/Ar* and *MR1/1500/Ar* were observed and used in the determination of fracture toughness. Appendix C, tables 17 – 19, give only the average crack length of the four cracks measured on each indent.

Chapter 5: Discussion

Discussion of the results as presented in chapter 4 follows. The focus is only on composites produced by sinter mullites method. An in depth explanation of the results is explored for each investigation undertaking.

5.1 X-Ray Diffraction

As was observed in figure 14, an increase in the intensity of mullite with a decrease in the amount of the silica phase (cristobalite) was observed with increase in temperature, thus from 1400 to 1500^{o}C. An amorphous glassy phase was noted at position around 20^{o} 2θ in all the XRD traces of compact samples *MRD1/1400/Ar, MRD1/1450/Ar and MRD1/1500/Ar*. Residual corundum was prevalent in all the compact samples to maximum temperature investigated, 1500^{o}C. *MR1/1600/Ar* trace of figure 43 hot press sintered to 1600^{o}C of compact with no diamond added revealed only mullite as the crystalline phase. This compact disc was sintered to investigate the extent of mullitisation using non-diamond containing milled mixture of alumina and silica in stoichiometric 3:2 mullite composition.

5.2 Scanning Electron Microscopy and Energy Dispersive Spectroscopy

Scanning electron microscopy for all the etched and un-etched composite samples containing 10wt% diamond showed a silica phase (cristobalite as from X-ray traces) and a corundum phase. The C atom as per EDS appeared to have segregated between the grain

boundaries of the two phases, see figures 26 and 31. The initial powder mixture, *MRD1 powder*, showed partial agglomeration of the particles, see figure 21. This could have contributed to the segregation of the particles during sintering as agglomeration tends to inhibit a homogenous dispersion of the diamond particles, though ultrasonic displacement was initiated. The un-etched samples also showed a grey fine grained structure (compare figures 23, 25 and 27) with black area with elements C (diamond), Al, Si and O. It is in such black areas where diamond appeared to have segregated (see figure 26 and 31), is it suggested that the diamond could have acted as nucleation points for growth of mullite grains. This suggestion is however open for further evaluation in separate projects. With sufficient temperature and time more mullite would grow around the diamond particles from the surrounding alumina and silica phases, this suggestion as stated still stands for further validation. It is also suggested that the mullite identified in all the composite X-ray traces could be embedded in either the cristobalite and corundum phases as all the SEM micrographs taken from the composite samples showed no phases with the characteristic needle or acicular structural morphology for secondary mullite even after etching the samples. It could also be that the mullite formed is predominantly present as primary mullite which has a characteristic fine, cuboidal or scaly morphology [29]. Figure 24, for sample *MRD1/1400/Ar*, shows spot analysis of such a structure with EDS elemental analysis, table 9, for Al/Si atomic ratio falling within the range for stoichiometric atomic ratio for 3:2 (secondary mullite) to 2:1 (primary mullite) of between 2.8 to 3.84 respectively. From table 9 the weight ratio of Al/Si was calculated to be 3.42 which could lend support to the suggestion that the spot is indeed primary mullite as the ratio is closer to the primary mullite ratio of 3.84 than to the secondary mullite ratio of 2.8. As a note,

however, as described in section 2.2.5, mullite displays variable Al to Si ratios with solid solution series $Al_{4+2x}Si_{2-2x}O_{10-x}$, with *x* ranging between about 0.2 and 0.9 (corresponding to about 55-90 mol% Al_2O_3) [39]. For the same dark phase for sample *MRD1/1450/Ar*, figure 26, the atomic Al/Si ratio for elemental spot analysis was calculated to be 3.21 which lie more close to the Al/Si stoichiometric 3:2 secondary mullite ratio, see table 10 for the EDS spot elemental analysis for sample *MRD1/1450/Ar*. This could also further support the conclusion that with increase in temperature mullite initially formed would transform to secondary mullite.

5.3 Raman Spectroscopy (Diamond Containing Compacts)

In the case of the sample hot press sintered at 1400^{o}C, figure 32 only the diamond Raman peak and the luminescence peak is visible. If there was any ***sp2*** graphitic carbon, it was in very small quantities. In the case of the composite sample sintered at 1450^{o}C, figure 33, some spots show weak evidence of the ***G*** and ***D*** bands expected of ***sp2*** graphitic carbon (peaks at around 1590 cm^{-1}). These peaks were somewhat difficult to fit, as they were barely visible above the background. No mullite bands produced any clear peaks in all the three samples. This could be caused by the fact that the mullite was not crystalline enough, thus the peaks may be weak and broad and therefore difficult to observe using Raman spectroscopy. X-ray diffraction gave a better observation with regard to mullite crystallinity. For the same sample, *MRD1/1450/Ar*, one spot (***spot A-back***, figure 33) gave a peak at ~465cm^{-1}. This was typically due to SiO2.

All the spots taken from a composite sintered at 1500^{o}C showed the presence of diamond, which peak is around 1332cm^{-1} for single crystal diamond (see reference spectrum ***Oct-Diamond Ref - back***, figure 34, taken on a single crystal synthetic diamond with octahedral habit).

All the spots plotted for sample *MRD1/1500/Ar* in figure 34 also had a sloping background subtracted. Spectrum for spot B in the same figure shows a diamond peak at virtually an identical position to the reference diamond spectrum. This indicated that the diamond particle being sampled was nominally unstressed.

The other spectra of figure 34 ***(spot C, D and E)*** showed a diamond Raman peak shifted by ~1.7cm^{-1} to higher wave numbers. This was indicative of the presence of a residual compressive stress of ~0.9GPa in magnitude. There was also some indication of splitting of the peak (shoulder at ~1340cm^{-1}), which would indicate non-isotropic local stresses, but more detailed analysis was difficult without knowledge of the orientation of the diamond crystallite.

There was a broad, weak peak, around 1620cm^{-1}, probably due to the presence of a small amount of ***sp2*** co-ordinated carbon. This however could be verified by taking spectra at longer acquisition times. As can be observed in figure 35, the second examination of the same composite sintered at 1500^{o}C, *MRD1/1500/Ar*, the ***G*** and ***D*** bands (peaks around 1590 cm^{-1}) expected of ***sp2*** graphitic carbon are more clearly visible though they were still weak, but definitely present.

5.4 Hardness and Fracture Toughness

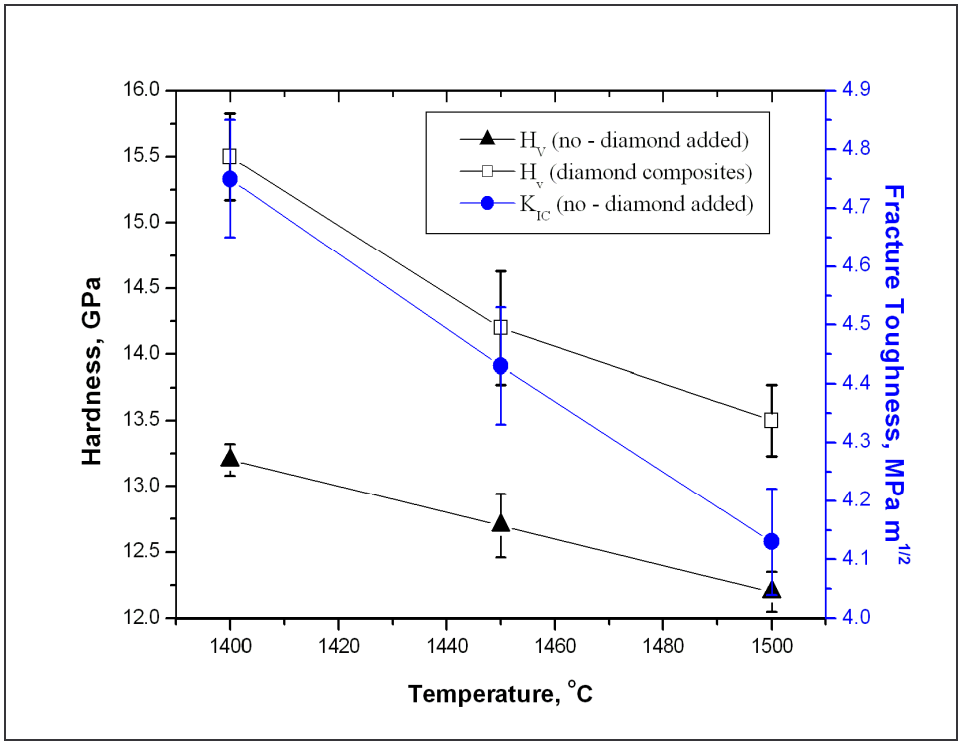


Figure 36: Graphic representation of hardness against temperature for samples *MR1/1400/Ar, MR1/1450/Ar and MR1/1500/Ar* (no – diamond added) and samples with 10wt% diamond added, i.e. samples *MRD1/1400/Ar, MRD1/1450/Ar & MRD1/1500/Ar*. Fracture toughness against temperature for samples with no diamond added is also plotted.

As was observed and presented in figure 36, H_v and K_{IC} decreased with increase in temperature for compact samples (*MR1/1400Ar, MR1/1450Ar and MR1/1500/Ar*). This could have been due to the increase in the amount of the mullite phase being formed which has lower values of H_v and K_{IC} as compared to alumina (see table 2, section 2.2.8). At the lowest sintering temperature investigated, 1400^{o}C, the dominant alumina phase is suggested to have contributed to the higher hardness and fracture toughness values. In the compacts with secondary diamond phase incorporated in them (*MRD1/1400Ar, MRD1/1450Ar and MRD1/1500/Ar*) the hardness of the samples deceased with increase in

temperature. This could be explained by the partial diamond degradation to non diamond carbon forms observed during Raman spectroscopy with increase in temperature. The observed gradual increase in the noise to signal ratio from sample *MRD1/1400/Ar* to *MRD1/1450/Ar* to *MRD1/1500/Ar* in figures 32 – 34 as compared to the reference diamond which is lorentzian (sharp) in figure 34 imply structural transformation from one carbon form to the other. This increase in the peak width observed on the various spots investigated (compare figure 32 and 34) also further support these transformations. In this case from diamond to non diamond carbon forms, which are the soft forms of carbon. Tentatively this could be the suggested to have caused the decrease in the hardness with increase in temperature. However, the difficulties or say the non visible cracks from the indents made on the compacts could also suggest improved fracture toughness in all the samples containing diamond. Fracture toughness of composites containing diamond can be measured by other available methods to further verify the suggestion.

Chapter 6: Conclusions & Recommendations

- Hardness, Hv of diamond containing composites were found to decrease with increase in temperature. This was attributed to mainly the degradation of diamond to non diamond carbon forms.
- The lower temperature investigated (1400^{o}C) yielded the highest hardness of 15.5 ± 0.33GPa with however a low content of mullite as compared to composite samples sintered at higher temperatures as observed from X-ray spectra of all the sintered diamond containing compacts. The density achieved at the sintering temperature was 93.7% to the theoretical. The density was somewhat lower as compared to the compact with no diamond and sintered at the same temperature (94.3% of the theoretical) due mainly to hindrance from the diamond particles to achieve a closely packed structure of all the particles at the sintering temperature and the susceptibility to agglomeration of the 2μm diamond used. The agglomeration is not only connected to the diamond, but to the large grain size of the synthesized mullite. The preparation process could also do with significant improvement for an better product.
- The hardness and fracture toughness of samples containing no diamond were better at the lowest temperature investigated (1400^{o}C), thus 13.2 ± 0.12GPa and 4.75 ± 0.10MPa·m$^{1/2}$ respectively. The seemingly high fracture toughness as compared to data in 13.2 versus 15.5 is because of the residual alumina after the sintering process. At this point it can be suggested the characteristic needle and cuboidal mullite structure as well as the presents of residual alumina could result in this high value of fracture toughness.

- The Raman spectroscopy carried out revealed some prevalence of diamond form in nominally unstressed form after sintering at the highest temperature investigated, 1500^{o}C though transformation to non-diamond form occurred leading to the observed presence of Raman shift of ~1.7cm^{-1} of estimated residual compressive stress of ~0.9GPa in magnitude and splitting of the diamond peak (shoulder at ~1340cm^{-1}), which indicated non-isotropic local stresses. Thus synthesizing diamond/ mullite composites at even higher temperatures (above 1600^{o}C) as predicted by the Al_2O_3 – SiO_2 phase diagram to form mullite with no residual silica and alumina would lead to most of the diamond transforming to non-diamond forms and adverse effects on the physical properties as observed in this work.
- The processing of diamond/ mullite composites through the sol/ gel route could still be further explored from the basis laid in this work and other authors [36].
- The density of composite compacts by sinter mullites could be further improved by using coarser diamond particles that are less susceptible to agglomeration and easier to disperse with the matrix.
- An optimum (higher) wt% of diamond could be investigated to further improve the hardness of the compacts.

Table 14: Comparison of physical properties of some of the mullite composites reviewed in chapter two of this work to physical properties obtained from sintered compacts.

		Physical Properties			
	Temp, ^oC (atm)	**Density, g/cm^3 (%)**	**H_v, GPa**	**K_{IC}, $MPa \cdot m^{1/2}$**	**Mullite content, wt% (vol %)**
This work, 10wt% diamond	1400 (Ar)	3.24 (93.7)	15.5 ± 0.33	-	-
	1450 (Ar)	3.27 (94.6)	14.2 ± 0.43	-	-
	1500 (Ar)	3.31 (95.8)	13.5 ± 0.27	-	-
Zircon/ mullite, 10wt% ZrO_2	1620 (Air)	-	-	2.5	90
Zircon/ mullite; 7.2wt% $Zr(Y)O_2$	1620 (Air)	(94.6)	-	4.6	92.8
Al, Alumina/ mullite	1600 (Air)	(97.9)	16.9 ± 0.5	2.98 ± 0.21	(5)
SiC/ Mullite, 20 vol % SiC	1650	(97.5)	-	3.9± 0.1	-

Appendix A: Reagent Mixing Calculations – Sol/ Gel Method

$2SiO_2$ + $3Al_2O_3$ = $3Al_2O_3 \cdot 2SiO_2$ (ii)

22{(28.086)+(15.994)2} *3{(26.9815)2+(15.994)3}*

3(101.945)+2(60.074)

120.148 **305.835** **425.983**

Stoichiometric weight of Al = 161.889228g

Stoichiometric weight of Si = 56.171g

Stoichiometric Ratio of Al/ Si = **2.88**

Purity of as received Si-$(OC_2H_5)_4$

(Tetra-ethylorthosilicate)

Industrial Chemicals, SA based on

the certificate of analysis = 99.91%

Si *(assay)* = 13.47%

Density = 0.934g/cm^3 (g/ml)

Purity of as received Al-$(OC_4H_9)_3$

(Aluminium Secondary Butoxide)

Industrial Chemicals, SA based on

the certificate of analysis = 95.0% and,

Al *(assay)* = 10.41%

Density = $0.9671 g/cm^3$(g/ml)

Aim: To mix the reagents to a stoichiometric ratio of Al/ Si = 2.88

We take a basis of 5ml (4.67g) of Si-(O**R**)$_4$ (0.022 mole)

Mass of Si in the 4.67g = 0.629g (i)

We need to calculate the amount of Al-(O**R**)$_3$ to be added to make a ratio of Al/ Si = 2.88 (The stoichiometric weight ratio for 3:2 mullite) and also taking into consideration the purity of the as received Al-(O**R**)$_3$.

$2.88^{Parts}{}_{Al}$ to $1^{Part}{}_{Si}$

Thus from (i) above we need 1.81g of Al

Therefore amount of Al-(O**R**)$_3$ to be added:

0.950*26.981538 / 246.322518 * Amount (Al-(O**R**)$_3$) = 1.81g

Amount (Al-(O**R**)$_3$) = 17.41g

Hence in total we add **17.41g** (0.071 moles) of Al-(O**R**)$_3$, which is equivalent to **18.0ml of** Al-(O**R**)$_3$ to be added.

Overall General Reaction Equation

$$6Al(O\mathbf{R})_3 + 2Si(O\mathbf{R})_4 + xH_2O \rightarrow 2Al_3Si(OH)_{13}{\bullet}xH_2O + 26\mathbf{R}OH$$

Recovery of the material by dilution with excess water directly yields an amorphous finely divided powder having the mullite composition. The powder maybe dried to ensure dehydration of the hydroxyaluminosilicate to amorphous mullite as shown below:

$$2Al_3Si(OH)_{13} \rightarrow 3Al_2O_3{\bullet}2SiO_2 + 13H_2O$$

The amorphous mullite powder is converted to crystalline mullite by heating the powder at a temperature of about 985 – 1000^{o}C.

Appendix B: Density and Porosity Measurements

Green Density Measurements

Table 15: Green and sintered density measurements for the compacts obtained by the sinter mullite method

Green and Sintered Density Measurements Compared									
Sample Identity	**State**	**Mass, g**	**Radius, cm**	**Height, cm**	**Area, sq cm**	**Volume, cc**	**Density, g/cc**	**Expected Theoretical Density*, g/cc**	**Final Sintered Density, %**
MR1/1400/Ar	Green	3.571	0.900	0.691	2.546	1.759	2.03	3.45	**94.3**
	Sintered	3.25							
MRD1/1400/Ar	Green	3.571	0.900	0.624	2.546	1.589	2.25	3.46	**93.7**
	Sintered	3.24							
MR1/1450/Ar	Green	4.435	0.900	0.864	2.546	2.199	2.02	3.45	**95.2**
	Sintered	3.28							
MRD1/1450/Ar	Green	4.036	0.900	0.710	2.546	1.807	2.23	3.46	**94.6**
	Sintered	3.27							
MR1/1500/Ar	Green	3.069	0.900	0.592	2.546	1.507	2.04	3.45	**96.5**
	Sintered	3.33							
MRD1/1500/Ar	Green	4.483	0.900	0.786	2.546	2.001	2.24	3.46	**95.8**
	Sintered	3.31							
* The expected theoretical density was calculated using the rule of mixtures on assumption of zero porosity being achieved upon sintering.									

Table 16: Determination of density of compacts by sinter mullite method using the Archimedes method

Sample Identity	MR1/1400/Ar		MRD1/1400/Ar		MR1/1450/Ar		MRD1/1450/Ar		MR1/1500/Ar		MRD1/1500/Ar	
	M_s	M_w	M_s	M_w	M_s	M_w	M_s	M_w	M_s	M_w	M_s	M_w
Suspended Mass, M_s and Wet Mass, M_w	1.6798	2.4188	0.8612	1.2457	1.7386	2.5003	3.0039	4.3277	2.4065	3.4375	0.9079	1.2951
	1.6781	2.4175	0.8628	1.2458	1.7388	2.4960	3.0041	4.3268	2.4069	3.4281	0.9055	1.2974
	1.6795	2.4179	0.8613	1.2455	1.7389	2.4971	3.0034	4.3265	2.4095	3.4293	0.9076	1.2966
	1.6783	2.4185	0.8601	1.2463	1.7396	2.5001	3.0048	4.3255	2.4055	3.4356	0.9060	1.2973
	1.6793	2.4177	0.8602	1.2453	1.7399	2.4999	3.0067	4.3261	2.4057	3.4299	0.9053	1.2947
Average, g	**1.6790**	**2.4181**	**0.8611**	**1.2457**	**1.7392**	**2.4987**	**3.0046**	**4.3265**	**2.4068**	**3.4321**	**0.9065**	**1.2962**
Initial Mass of Sample, g	2.4040		1.2455		2.4940		4.3230		3.4140		1.2910	
Oven Dried Mass (M_d), g	2.4020		1.2453		2.4930		4.3230		3.4128		1.2900	
Apparent Density, g/cc	3.32		3.24		3.30		3.28		3.39		3.36	
Apparent Volume, cc	0.73		0.38		0.75		1.32		1.01		0.38	
Bulk Density, g/cc	3.25		3.24		3.28		3.27		3.33		3.31	
Apparent Porosity, %	1.91		0.06		0.62		0.27		1.76		1.34	
Vol. of open porosity, cm3	0.01		0.0002		0.005		0.004		0.018		0.005	
Bulk Vol., cm3	0.74		0.38		0.76		1.32		1.03		0.39	
Theoretical Density, g/cc	3.45		3.46		3.45		3.46		3.45		3.46	
Densification Achieved, %	94.3		93.7		95.2		94.6		96.5		95.8	
Closed Porosity, %	3.8		6.3		4.2		5.1		1.7		2.9	

Appendix C: Hardness and Fracture Toughness Results

Table 17: Hardness and fracture toughness measurements from samples *MR1/1400/Ar* and *MRD1/1400/Ar*, i.e. compact sample with no diamond and with added 10wt% diamond respectively

MR1/1400/Ar Composition - 10kgf applied						**MRD1/1400/A Composition - 10kgf applied**					
	1st Indent	**2nd Indent**	**3rd Indent**	**4th Indent**	**5th Indent**		**1st Indent**	**2nd Indent**	**3rd Indent**	**4th Indent**	**5th Indent**
1st Diagonal	118.0	116.0	119.0	117.0	118.0	**1st Diagonal**	107.0	109.0	107.0	111.0	109.0
2nd Diagonal	117.0	117.0	117.0	118.0	117.0	**2nd Diagonal**	109.0	108.0	108.0	110.0	107.0
Average Diagonal	**117.5**	**116.5**	**118.0**	**117.5**	**117.5**	**Average Diagonal**	**108.0**	**108.5**	**107.5**	**110.5**	**108.0**
Average Crack Length, µm	114.0	103.7	123.7	113.0	114.7	**Average Crack Length, µm**	-	-	-	-	-
Hv, GPa	13.176	13.403	13.065	13.176	13.176	**Hv, GPa**	15.596	15.453	15.742	14.898	15.596
K_{IC}, MPa·$m^{1/2}$	4.733	5.006	4.525	4.754	4.719	**K_{IC}, MPa·$m^{1/2}$**	-	-	-	-	-
Average d value for sample	**117.4**					**Average d value for sample**	**108.5**				
Average Hv, GPa	**13.2**					**Average Hv, GPa**	**15.5**				
Average K_{IC}, MPa·$m^{1/2}$	**4.7**					**Average K_{IC}, MPa·$m^{1/2}$**	**-**				
Standard Deviation for Hv	0.12					**Standard Deviation for Hv**	0.33				
Standard Deviation for K_{IC}	0.17					**Standard Deviation for K_{IC}**	-				
Standard Deviation for c	14.8					**Standard Deviation for c**	-				
Standard Deviation for d	0.84					**Standard Deviation for d**	1.35				

Table 18: Hardness and fracture toughness measurements from samples *MR1/1450/Ar* and *MRD1/1450/Ar*, i.e. compact sample with no diamond and with added 10wt% diamond respectively

MR1/1450/Ar Composition - 10kgf applied.						**MRD1/1450/Ar Composition - 10kgf applied**					
	1st Indent	**2nd Indent**	**3rd Indent**	**4th Indent**	**5th Indent**		**1st Indent**	**2nd Indent**	**3rd Indent**	**4th Indent**	**5th Indent**
1st Diagonal	119.0	120.0	120.0	121.0	119.0	**1st Diagonal**	112.0	114.0	115.0	116.0	115.0
2nd Diagonal	121.0	123.0	118.0	119.0	118.0	**2nd Diagonal**	109.0	113.0	111.0	114.0	113.0
Average Diagonal	**120.0**	**121.5**	**119.0**	**120.0**	**118.5**	**Average Diagonal**	**110.5**	**113.5**	**113.0**	**115.0**	**114.0**
Average Crack Length, µm	111.0	130.0	118.0	130.0	135.0	**Average Crack Length, µm**	-	-	-	-	-
Hv, GPa	12.633	12.323	12.846	12.633	12.955	**Hv, GPa**	14.898	14.121	14.247	13.755	13.998
K_{IC}, MPa·$m^{1/2}$	4.697	4.286	4.594	4.340	4.313	**K_{IC}, MPa·$m^{1/2}$**	-	-	-	-	-
Averaged value for sample	**119.8**					**Averaged value for sample**	**113.2**				
Average Hv, GPa	**12.7**					**Average Hv, GPa**	**14.2**				
Average K_{IC}, MPa·$m^{1/2}$	**4.4**					**Average K_{IC}, MPa·$m^{1/2}$**	**-**				
Standard Deviation for Hv	0.24					**Standard Deviation for Hv**	0.43				
Standard Deviation for K_{IC}	0.19					**Standard Deviation for K_{IC}**	-				
Standard Deviation for c	9.94					**Standard Deviation for c**	-				
Standard Deviation for d	1.55					**Standard Deviation for d**	2.10				

Table 19: Hardness and fracture toughness measurements from samples *MR1/1500/Ar* and *MRD1/1500/Ar*, i.e. compact sample with no diamond and with added 10wt% diamond respectively

MR1/1500/Ar Composition - 10kgf applied.						**MRD1/1500/Ar Composition - 10kgf applied**					
	1st Indent	**2nd Indent**	**3rd Indent**	**4th Indent**	**5th Indent**		**1st Indent**	**2nd Indent**	**3rd Indent**	**4th Indent**	**5th Indent**
1st Diagonal	121.0	123.0	122.0	123.0	121.0	**1st Diagonal**	118.0	111.0	116.0	116.0	117.0
2nd Diagonal	121.0	121.0	122.0	123.0	122.0	**2nd Diagonal**	117.0	119.0	118.0	114.0	116.0
Average Diagonal	**121.0**	**122.0**	**122.0**	**123.0**	**121.5**	**Average Diagonal**	**117.5**	**115.0**	**117.0**	**115.0**	**116.5**
Average Crack Length, µm	139.0	142.0	160.0	149.0	140.0	**Average Crack Length, µm**	-	-	-	-	-
Hv, GPa	12.425	12.222	12.222	12.024	12.323	**Hv, GPa**	13.176	13.755	13.289	13.755	13.403
K_{IC}, MPa·m$^{1/2}$	4.162	4.084	3.848	3.955	4.130	**K_{IC}, MPa·m$^{1/2}$**	-	-	-	-	-
Averaged value for sample	**121.9**					**Averaged value for sample**	**116.2**				
Average Hv, GPa	**12.2**					**Average Hv, GPa**	**13.5**				
Average K_{IC}, MPa·m$^{1/2}$	**4.0**					**Average K_{IC}, MPa·m$^{1/2}$**	**-**				
Standard Deviation for Hv	0.15					**Standard Deviation for Hv**	0.27				
Standard Deviation for K_{IC}	0.13					**Standard Deviation for K_{IC}**	-				
Standard Deviation for c	12.7					**Standard Deviation for c**	-				
Standard Deviation for d	0.88					**Standard Deviation for d**	2.3				

Appendix D: X-Ray Diffraction Patterns, Peak List and Reference Codes

Alumina/ Silica in 3:2 Mullite Molar Ratio + 10wt% Diamond Compacts

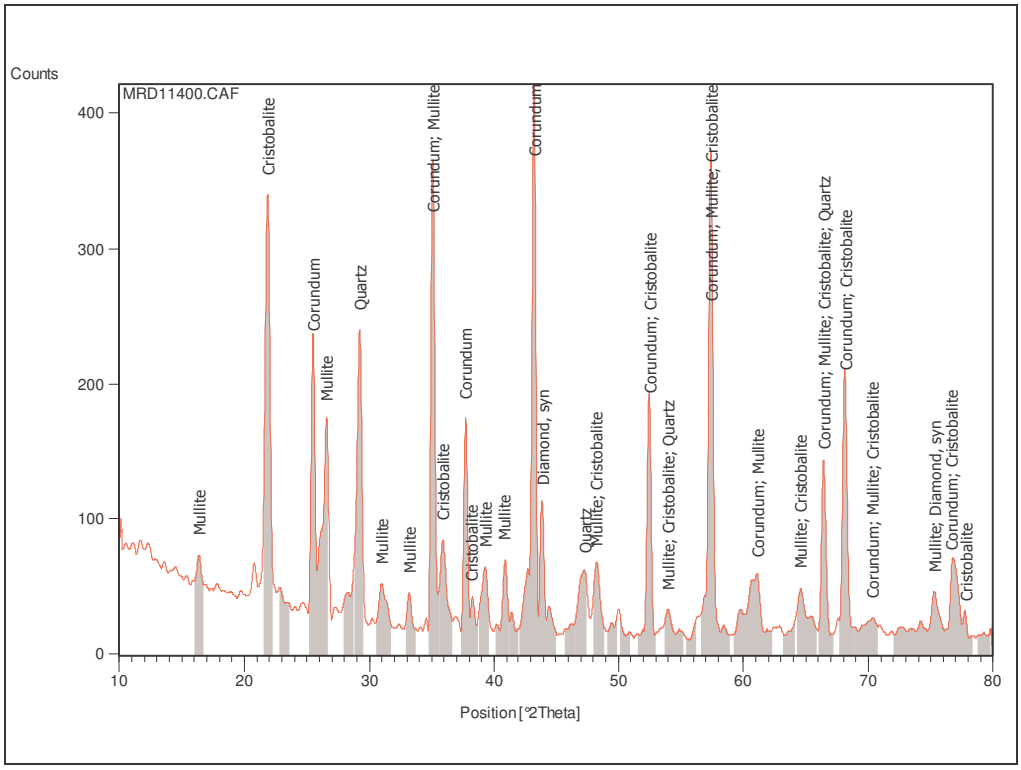


Figure 37: XRD trace for compact *MRD1/1400/Ar*

Table 20: Identified X-ray patterns list for *MRD1/1400/Ar*

Ref. Code	Compound Name	Displacement [°2θ]	Chemical Formula
01-071-1123	Corundum	0,000	Al_2O_3
00-001-0613	Mullite	0,000	$Al_6Si_2O_{13}$
00-065-0537	Diamond, syn	0,000	C
00-004-0379	Cristobalite	0,000	SiO_2
01-081-0068	Quartz	0,000	SiO_2

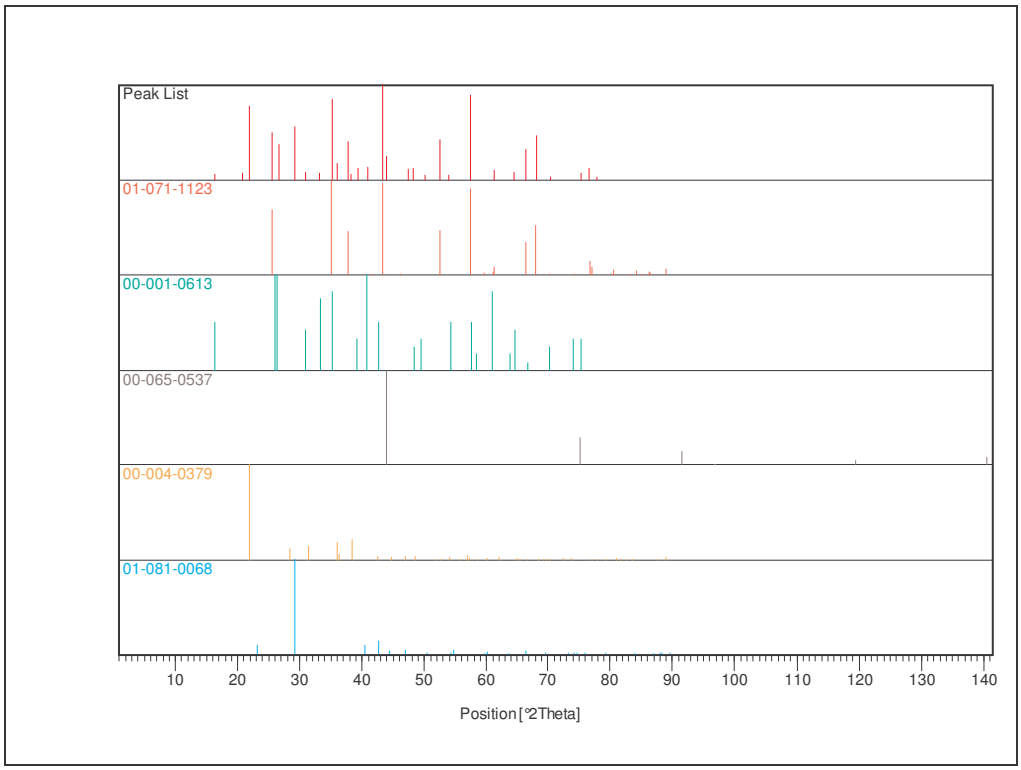


Figure 38: Plot of Identified Phases for *MRD1/1400/Ar*

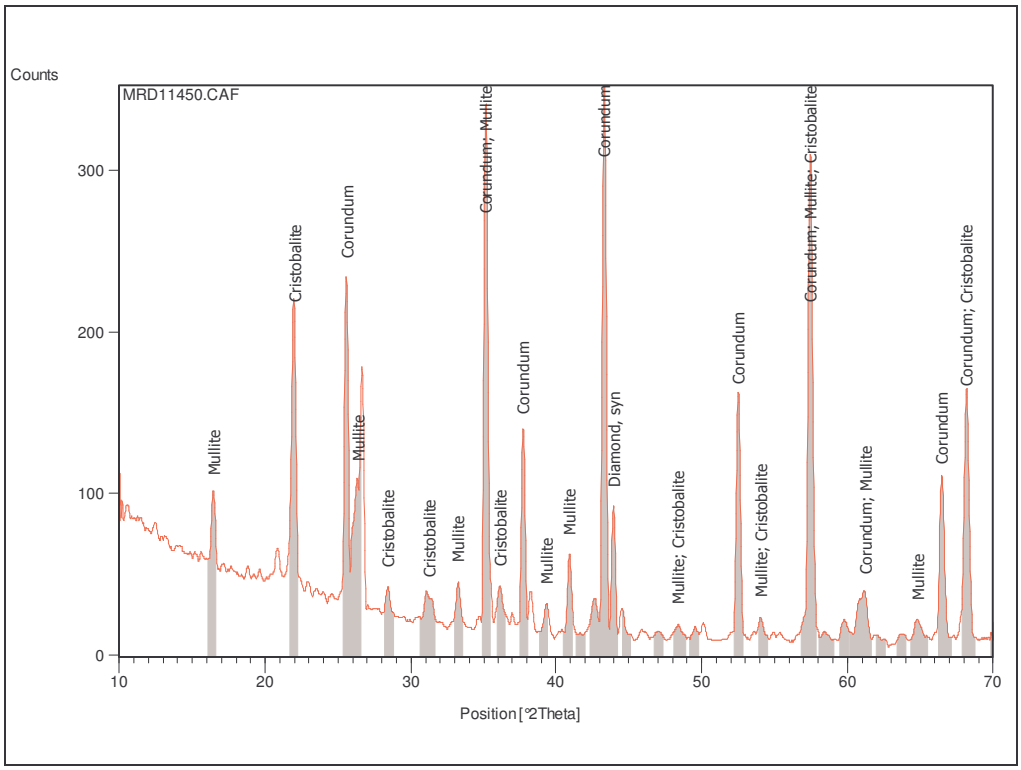


Figure 39: XRD trace for compact *MRD1/1450/Ar*

Table 21: Identified X-ray patterns list for *MRD1/1450/Ar*

Ref. Code	Compound Name	Displacement [°2θ]	Chemical Formula
00-005-0712	Corundum	0,000	Al_2O_3
00-001-0613	Mullite	0,000	$Al_6Si_2O_{13}$
00-001-0438	Cristobalite	0,000	SiO_2
00-065-0537	Diamond, syn	0,000	C

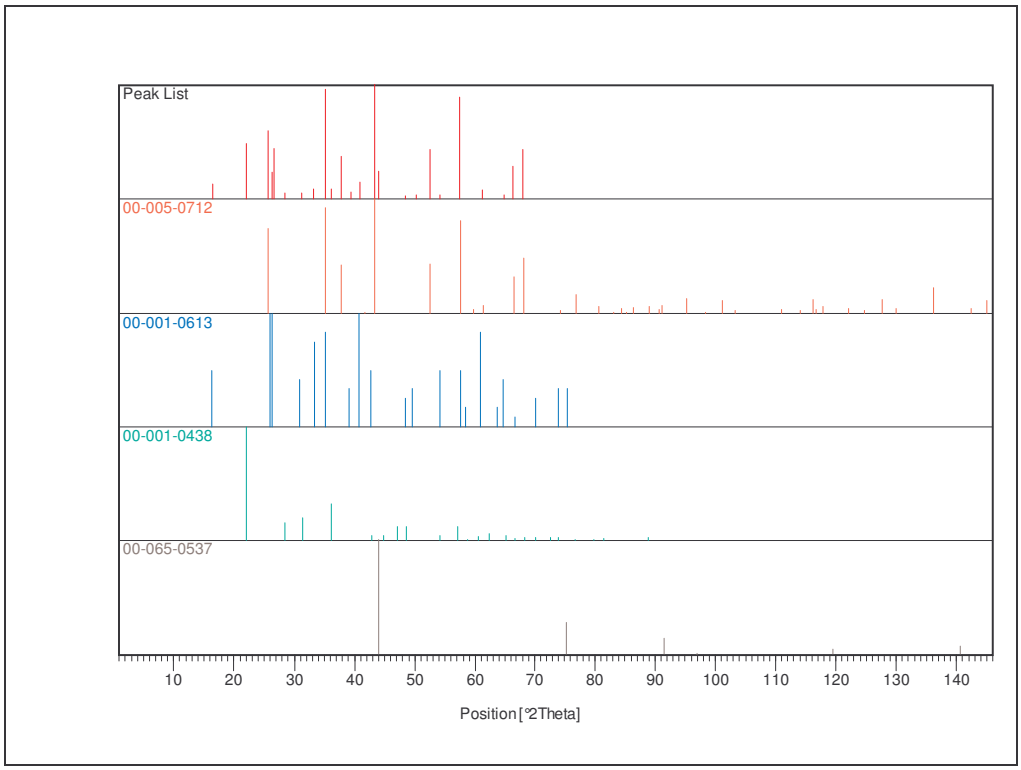


Figure 40: Plot of Identified Phases for MRD1/1450/Ar

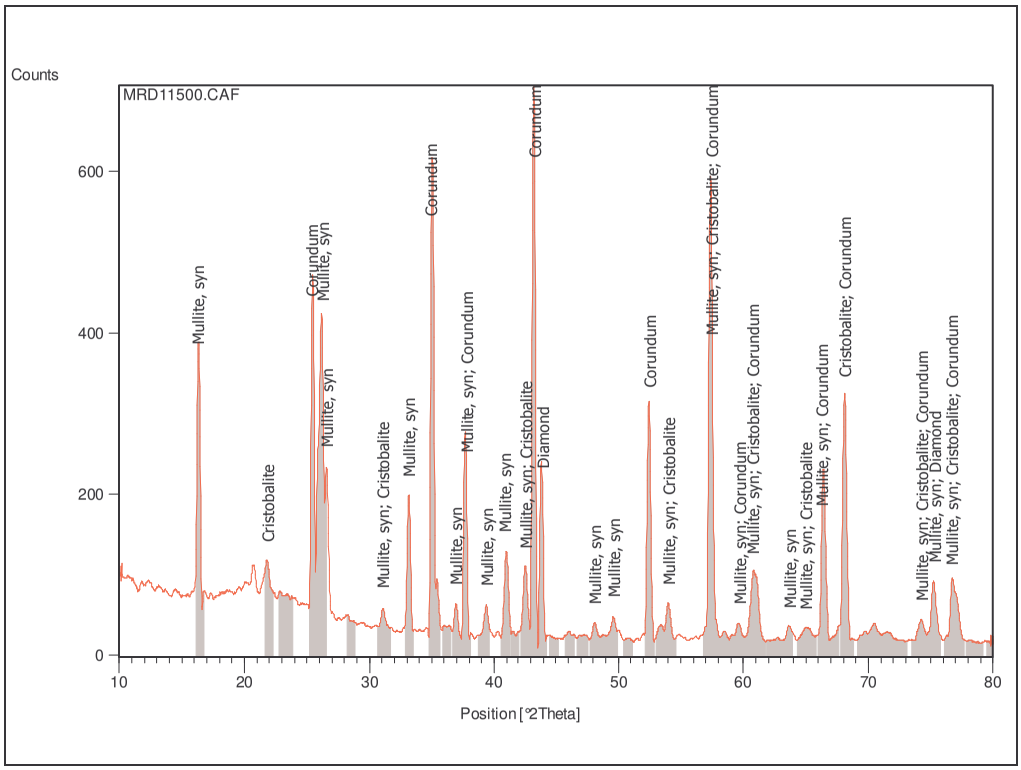


Figure 41: XRD trace for compact *MRD1/1500/Ar*

Table 22: Identified X-ray patterns list for MRD1/1500/Ar

Ref. Code	Compound Name	Displacement [°2θ]	Chemical Formula
01-079-1453	Mullite, syn	0,000	$Al_{4.64}Si_{1.36}O_{9.68}$
01-075-0225	Diamond	0,000	C
00-001-0438	Cristobalite	0,000	SiO_2
01-071-1123	Corundum	0,000	Al_2O_3

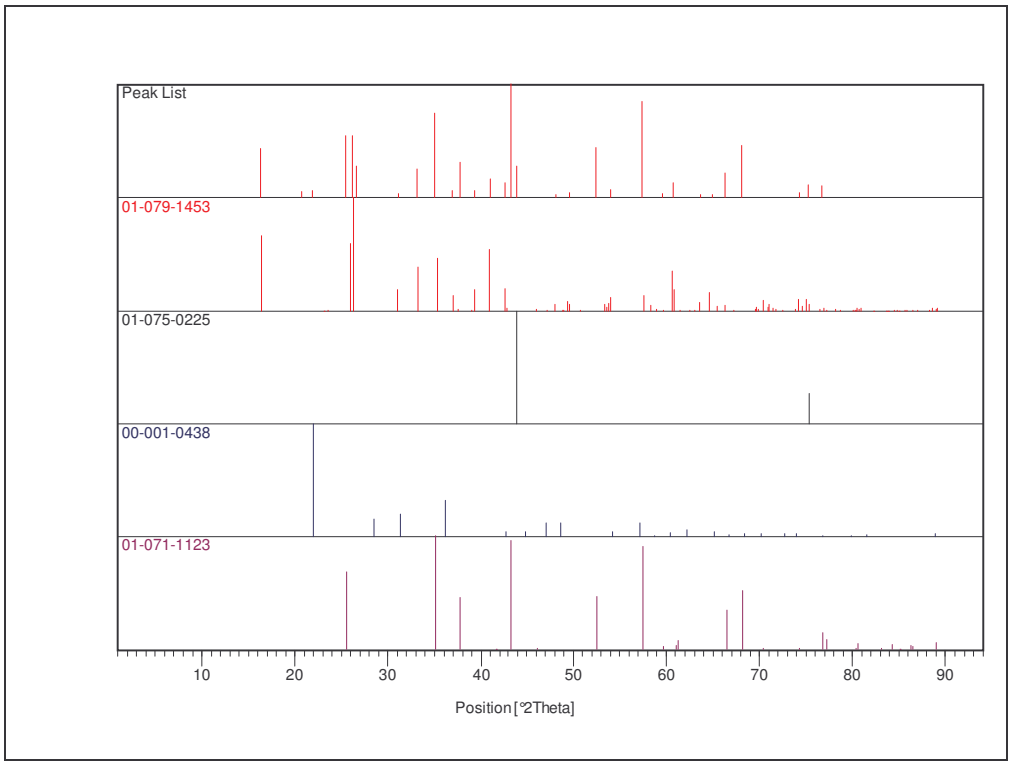


Figure 42: Plot of Identified Phases for *MRD1/1500/Ar*

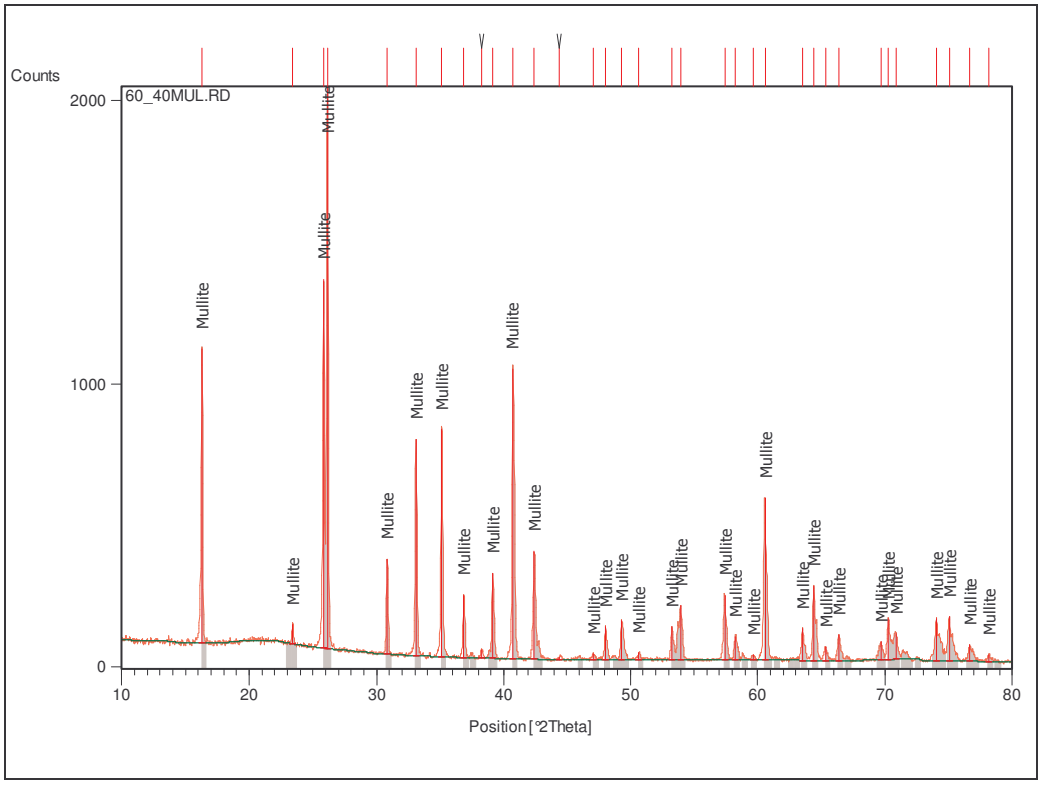


Figure 43: XRD trace for compact *MR1/1600/Ar*

Table 23: Identified X-ray pattern List for *MR1/1600/Ar*

Ref. Code	Score	Compound Name	Displacement [°2Th.]	Scale Factor	Chemical Formula
01-083-1881	27	Mullite	0,000	0,093	$Al(Al_{1.272}Si_{0.728}O_{4.864})$

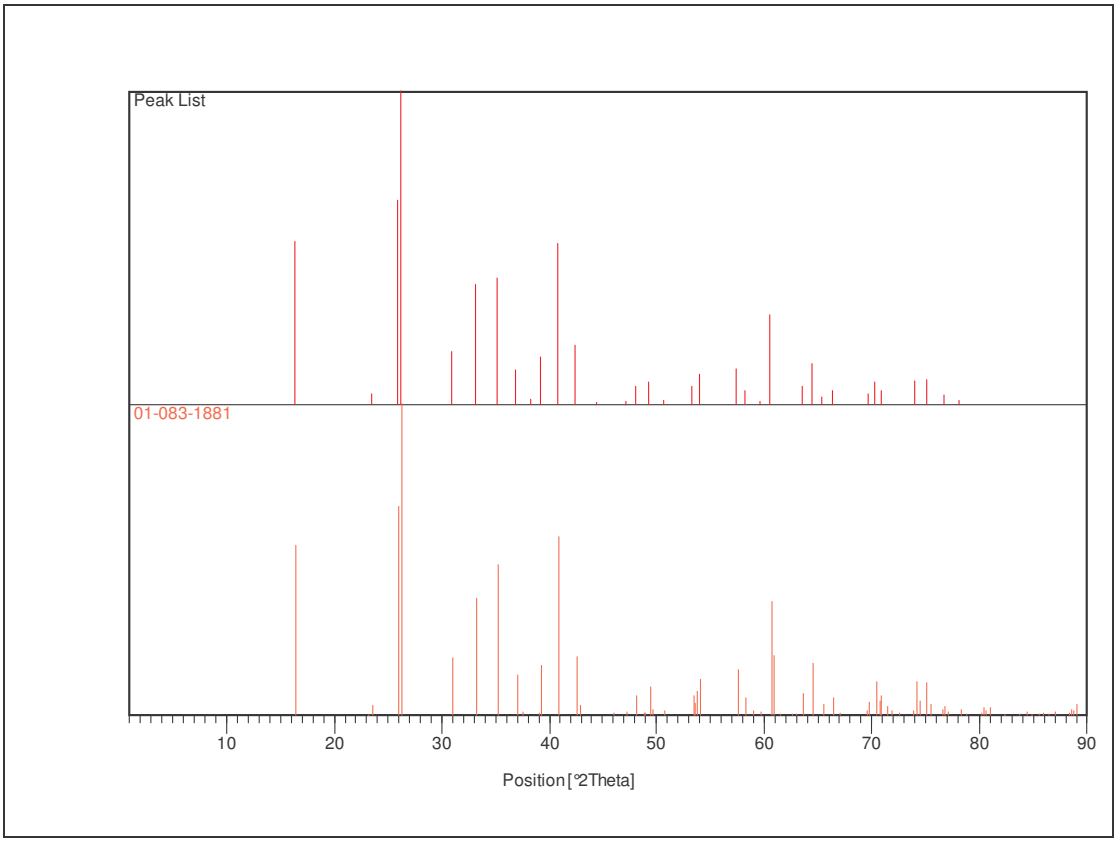


Figure 44: Plot of Identified Phases for *MR1/1600/Ar*

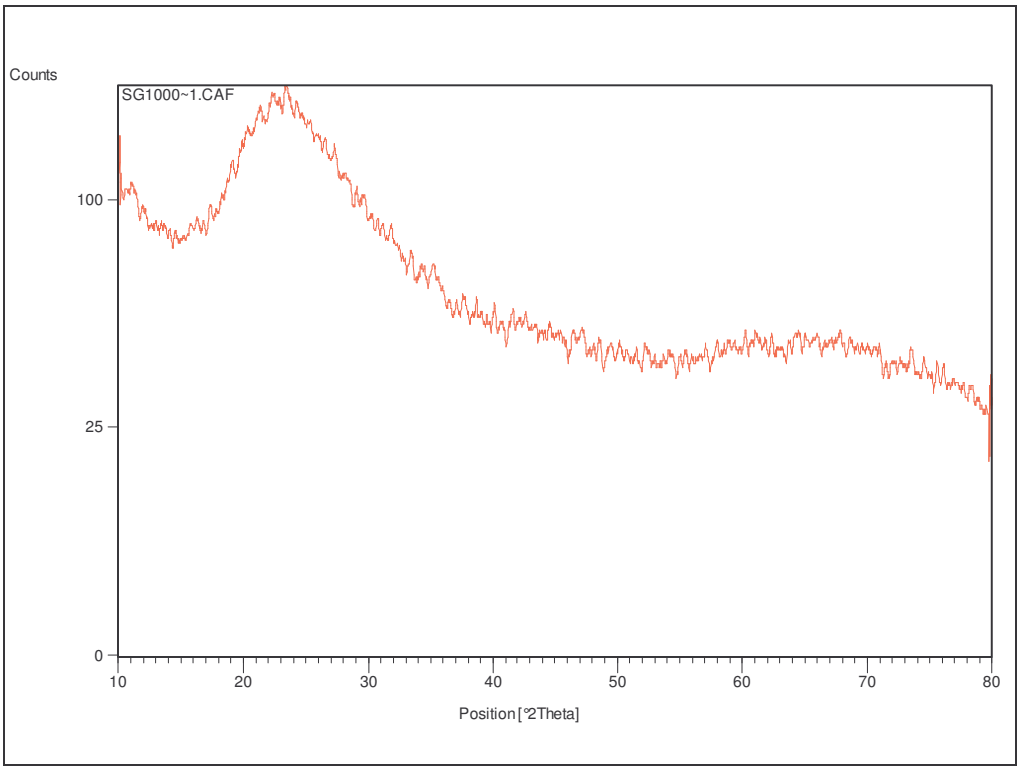


Figure 45: XRD trace for compact *SG/1000/A*

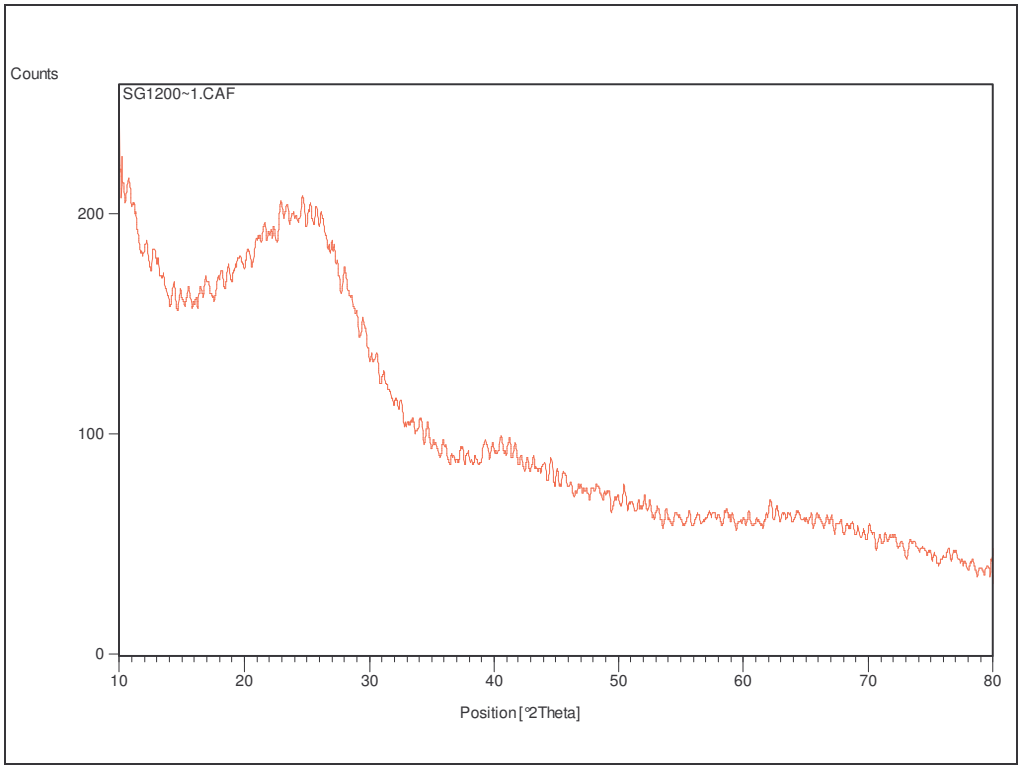


Figure 46: XRD trace for compact *SG/1200/A*

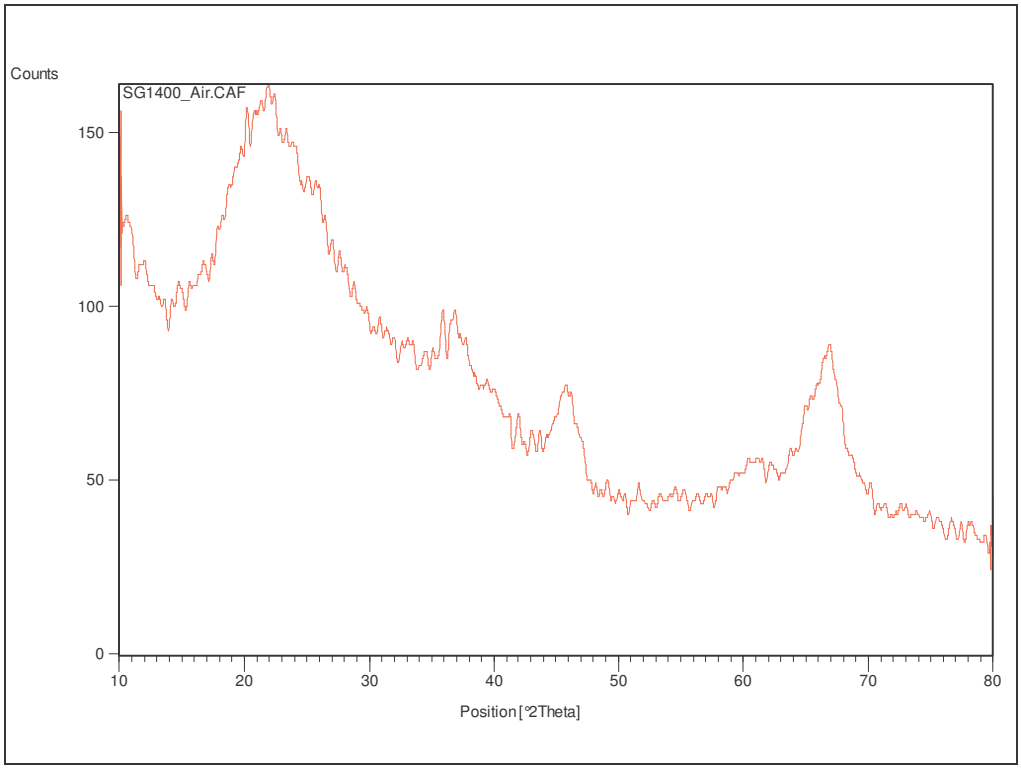


Figure 47: XRD trace for compact *SG/1400/A*

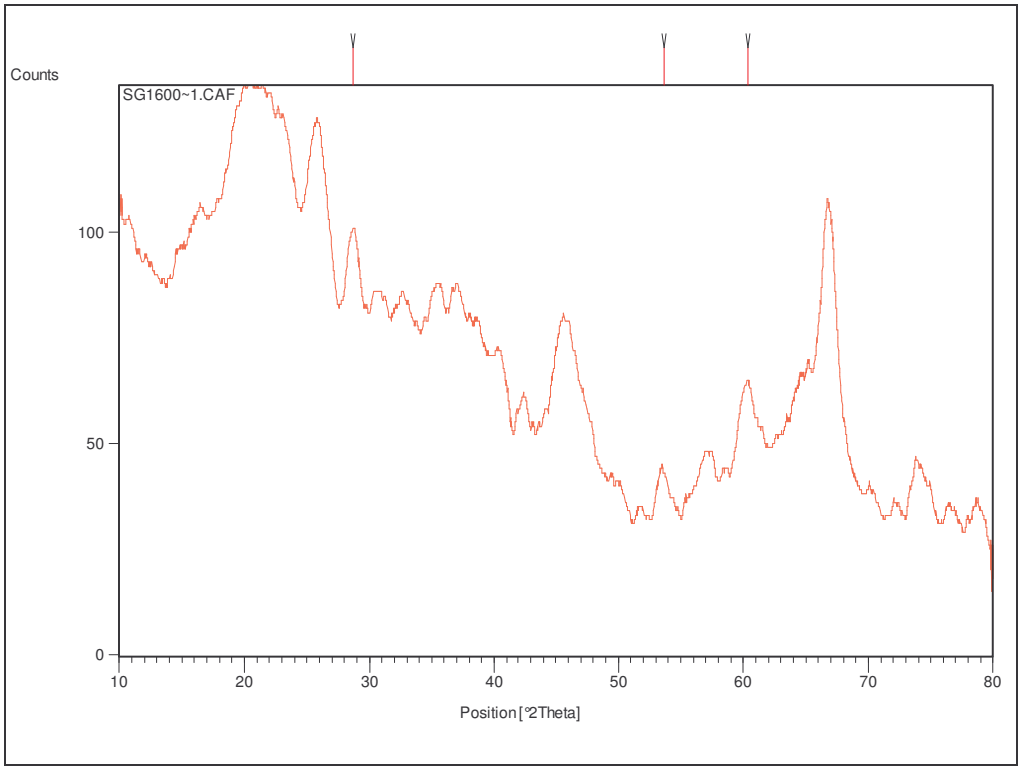


Figure 48: XRD trace for compact *SG/1600/A*

Bibliography

1. McKie A.L. and Ebrahim H.M., *Investigation into Diamond/Alumina Composites.* PRME 4009 Research Project; University of the Witwatersrand, 2005. **November**.
2. Eggerding Carl L., Frank Gonzales Jr., and Niklewski Jerzy B., *Process for Forming Mullite.* United States Patent, Jun. 9, 1981. **Patent No. 4,272,500**.
3. Hillig William B. and Musikant Solomon, *Mullite Matrix Composite.* United States Patent, Feb. 3, 1987. **Patent No. 4,640,899**.
4. Hillig William B. and Musikant Solomon, *Mullite by Reactive Hot Pressing.* United States Patent, Feb. 3, 1987. **Patent No. 4,640,904**.
5. Park H.C, et al., *Preparation of zirconia-mullite composites by an infiltration route.* Material Science and Engineering, 2005. **A405**: p. 233-238.
6. Riedel Ralf, et al., *Polymer-derived Mullite-SiC Based Nanocomposites.* J. E. Ceram Soc., 2009. **29**: p. 3079-3090.
7. Rezaie H.R., Rainforth W. M., and Lee W. E., *Fabrication and Mechanical Properties of SiC Platelets Reinforced Mullite Matrix Composites.* J. European Ceram Soc., 1999. **19**: p. 1777-1787.
8. Zhensong Tong, Zhuoshen Shen, and Yujuan Zhang, *Aluminum/ Diamond Composites and Their Applications in Electronic Packaging.* Sch. of Mat. Sci. & Eng. Beijing University of Sci. & Tech., 2007(86-10-62333649).
9. ACerS - NIST., *Phase Equilibria Diagrams CD-Rom database, version 3.1, NIST standard reference database 31, 2-5 users.* 2004-2005.

10. Mendelovici E., *Comparative Study of the Effects of Thermal and Mechanical Treatments on the Structures of Clay Minerals* J. Thermal Analysis, 1997. **49**: p. 1385-1397.

11. Sanchez-Soto P.J. and Perez-Rodriguez J.L., *Thermal Analysis of Pyrophyllite Transformations.* 1989: p. 267-276.

12. <http://en.wikipedia.org/wiki/Sol-gel>.

13. Inui Tomoyuki and Inoue Masashi, *Process for Production of High-Purity Mullites.* United States Patent, Aug 16, 1994. **Patent No.: 5,338,707**.

14. Hull D. and Clyne T.W., *An Introduction to Composite Materials.* Cambridge Solid State Science Series, 1996.

15. Senthil Kumar A., Raja Durai A., and Sornakumar T., *Development of yttria and ceria toughened alumina composite for cutting tool application.* Int. J. Refractory metals & Hard Materials, 2007. **25**: p. 214 - 219.

16. http://www.substech.com/dokuwiki/doku.php?id=estimations_of_composite_materials_properties.

17. K.M. Subodh, M.L.N. Pappu, and R.K. Goldberg, *Micromechanics of Particulate Reinforced Composites.* NASA Technical Memorandum 107276, August, 1996.

18. Quinn J.B. and Quinn G.D., *On the hardness and brittleness of ceramics.* Key Engineering Materials, 1997. **132-136**(1): p. 460-463.

19. Dutta S., *Fracture Toughness and Reliability in High-Temperature Structural Ceramics and Composites: Prospects and Challenges for the 21st Century.* Bull Mater Sci. , 2001. **24**(2): p. 117 - 20.

20. Ruys A.J., Simpson S.A., and Sorrell C.C., *Thixotropic Casting of Ceramic Matrix Composites.* International Ceramic Monographs, 1994. **1**(1): p. 692-700.

21. Ohji T., et al., *Strengthening and Toughening Mechanisms of Ceramic Nano-Composites*

J. Am Ceram Soc 1998. **81**(6): p. 1453 - 60.

22. Larsson P., et al., *Wear of a new type of Diamond Composite* Int. J. Refractory Metals & Hard Materials, 1999. **17**: p. 453-460.

23. Trusty P.A. and Yeomans J.A., *The Toughening of Alumina with Iron: Effects of Iron Distribution on Fracture Toughness.* J. E. Ceram Soc., 1997. **17**: p. 495-504.

24. Steinbrech R.W., *Toughening Mechanisms for Ceramic Materials.* J. E. Ceram Soc., 1992. **10**: p. 131-142.

25. Ritchie R.O., *Mechanisms of Fatigue Crack Propagation in Metals, Ceramics and Composites; Role of Crack Tip Shielding.* Mat. Sci. Engng., 1988. **A103**: p. 15-28.

26. <http://acbm.northwestern.edu/toughening.html>

27. Rendtorff N.M., Garrido L.B., and Aglietti E.F., *Mechanical and Fracture Properties of Zircon-mullite Composites Obtained by Direct Sintering.* Ceramics International, 2009. **35**: p. 2907-2913.

28. Viswabaskaran V., Gnanam F.D., and Balasubramanian M., *Mullitisation Behaviour of Calcined- alumina Mixtures.* Ceramics International, 2003. **29**: p. 561-571.

29. Lee W.E., et al., *Mullite formation in clays and clay - derived vitreous ceramics.* J. Eur. Ceram. Soc. , 2008. **28**: p. 465 - 471.

30. Viswabaskaran V., Gnanam F.D., and Balasubramanian M., *Mullite from clay - reactive alumina for insulating substrate application.* Applied Clay Science, 2004. **25**: p. 29 - 35.

31. Zawrah M.F. and Aly M.H., *In situ formation of Al_2O_3-SiC-mullite from Al-matrix composites.* Ceramics International 2006. **32**: p. 21 - 28.

32. Carty W. M. and Senapati U., *Porcelain-raw materials, processing, phase evolution and mechanical behaviour.* J. Am. Ceram. Soc., 1998. **81**: p. 3-20.

33. Rezaie H., Rainforth W. M., and Lee W. E., *Mullite Evolution in Ceramics Derived from Kaolinite, Kaolinite with added α-alumina and sol-gel precursors.* Br. Ceram. Trans, 1997. **96**(5): p. 181 - 187.

34. Liu K.C. and Thomas G., *Time-Temperature-Transformation curves for Kaolinite - α-alumina.* J. Am. Ceram. Soc. . **77**: p. 545 - 552.

35. Gardner and Wilcox, United States Patent. **Patent No. 3,857,923**.

36. Yoldas Bulent E. and Partlow Deborah P., *Low Temperature Formation of Mullite Using Silicon Alkoxide and Aluminum Alkoxide.* United States Patent, Aug 18, 1987. **Patent No.: 4,687,652**.

37. Chang-Whan Won and Bernard Siffert, *Preparation by Sol-Gel Method of SiO_2 and Mullite ($3Al_2O_3 \cdot 2SiO_2$) Powders and Study of Their surface Characteristics by Inverse Gas Chromatography and Zetametry.* Colloids and Surfaces A: Physicochemical and Engineering Aspects 1998. **131**: p. 161 - 172.

38. Samanta A.K., Dhargupta K.K., and Ghatak S., *In Situ Development of SiC-Mullite Composite in Ambient Atmosphere from SiC and Al-hydroxyhydrogel Powder Precursor.* J. Material Science Letters, 2001. **20**: p. 2077-2080.

39. Schneider H. and Komarneni S., *Mullite.* Wiley-VCH, Weinheim, 2005: p. 46-70.

40. Schneider H., Schreuer J., and Hildmann B., *Structure and Properties of Mullite - A Review.* J. E. Ceram Soc. , 2008. **28**: p. 329 - 344.

41. Burnham C.W., *Refinement of the crystal structure of sillimanite. Z. Krist.* , 1963. **118**: p. 127-148.

42. Saalfeld H. and Guse W., *Structure refinement of 3:2-mullite ($3Al_2O_3 \cdot 2SiO_2$). N. Jb. Miner. Mh*, 1981. **H4**: p. 145-150.

43. Angel R.J, McMullan R.K., and Prewitt C.T., *Substructure and superstructure of mullite by neutron diffraction* Am. Miner., 1991. **76**: p. 332-342.

44. Sornakumar T., *Advanced ceramic-ceramic composite tool materials for metal cutting applications.* Key Eng Mater 1996. **114**: p. 173 - 88.

45. http://www.materialkemi.lth.se/for_students/courses/course_projects/hardmaterial/Index.htm.

46. <http://www.matweb.com/alumina>

47. Acchar W. and Segadães A.M., *Properties of sintered alumina reinforced with niobium carbide.* Int. J. Refractory Metals & Hard Materials 2009. **27**: p. 427 - 430.

48. <http://www.accuratus.com/mullite.html>.

49. Zhang F.C., Luo H.H., and Roberts S.G., *Mechanical Properties and Microstructure of Alumina-Mullite Composite.* J. Material Science, 2007. **42**: p. 6798-6802.

50. Anya C.C., J. Material Science, 1999. **35:5557**(DOI: 10:1023/A:1004729015686).

51. Medvedovski E., *Alumina-mullite Ceramics for Structural Applications* Ceramics International, 2006. **32**: p. 369-375.

52. Luo H.H., Zhang F.C., and Roberts S.G., *Wear Resistance of Reaction Sintered Alumina/ Mullite Composite.* Material Science and Engineering, 2008. **A478**: p. 270-275.

53. Taktar S. and Baspinar M.S., *Wear and Friction Behaviour of Alumina/ Mullite Composite by Sol-Gel Infiltration Technique.* Material and Design, 2005. **26**: p. 459-464.

54. Zhang H., Maljkovic N., and Mitchell B.S., *Structure and interfacial properties of nanocrystalline aluminium/mullite composites.* Material Science and Engineering, 2002. **A326**: p. 317-323.

55. Tamotsu Akashi and Akira Sawaoka, *Dynamic Compaction of Composite Materials Containing Diamond.* United States Patent, Sept. 22, 1987. **Patent No. 4,695,321**.

56. http://johnchan.phychembio.com/centralblog/07/diamond.png.

57. http://images.google.co.za/imgres?imgurl=http://newton.ex.ac.uk/research.

58. Bundy F.P. and Minomura S.; (Editor), *Ch. 1, pp. 1-10 in Solid State Physics Under Pressure: Recent Advances with Anvil Devices.* KTK Scientific Publishers, Tokyo, Japan, 1985.

59. Weathers M. S. and Bassett W. A., *Phys. Chem. Miner.*, 1987. **15**(2): p. 105-112

60. Mitchell A.C., Shaner J.W., and Keeler R. N., *Physica B+C (Amsterdam)*, 1986. **139-140**: p. 386-389

61. Shaner J. W., et al., *J. Phys., Colloq.*, 1984. **45**(C8, No. 11): p. 235-237

62. Bundy F. P., *Physica A (Amsterdam)*, 1989. **156**(1): p. 169-178

63. Bundy F.P., *J. Geophys. Res., B*, 1980. **85**(B12): p. 6930-6936

64. Young D.A., *Phase Diagrams of the Elements, Ch. 9.* University of California Press, Berkeley, California, 1991: p. 113-117.

65. Richard Bodkin, *A Synthesis and Study of AlMgB14.* Doctor of Philosophy Thesis, 2005. **University of the Witwatersrand**: p. 28.

66. Lee J.S. and Yu S.C, *Characterizasation and Sintered Bodies of Mullite Derived Via Coprecipitation Alumina Silica Powders.* Mat. Res. Bulletin: National Cheng Kung University, China, 1992. **27**: p. 811-821.

67. Shetty D.K., et al., J. Material Science, 1985. **20**: p. 1873.

68. Kromka A., et al., *Identification of Carbon Phases and Analysis of Diamond/Substrate Interfaces by Raman Spectroscopy* Carbon, 2005. **43**: p. 425-429.